SHIBAURA INSTITUTE OF TECHNOLOGY

Graduate School of Science and Engineering

Regional Environmental Systems

DOCTORAL DISSERTATION

Innovative Techniques for Enhancement of Superconducting Characteristics of Bulk MgB_2

Arvapalli Sai Srikanth

Guide: Prof. Muralidhar Miryala

Declaration

I hereby declare that except where specific reference is made to the work of others, the contents of this dissertation are original and have not been submitted in whole or in part for consideration for any other degree or qualification in this, or any other university. This dissertation is my own work and contains nothing that is the outcome of work done in collaboration with others, except as specified in the text and Acknowledgements.

Arvapalli Sai Srikanth

March 2020

Acknowledgements

Firstly, I would like to thank my supervisor, Professor Muralidhar Miryala, for his huge guidance and support. He has given my mind substantial room to wander and accepted my ideas throughout my doctoral course. Thank you for the wonderful opportunities you have opened for me.

Secondly, I would like to thank President Prof. Masato Murakami for his constant suggestions and motivating me towards my PhD pursuit. Also, I am indebted to other professors (Prof. N Sakai, Prof. A Yamamoto and Prof. T Oka), staff and students in the laboratory for their support during my course at SIT. I would also like to thank Techno-plaza staff as well as SIT staff for helping me. In addition, I would like to thank Shibaura Institute of Technology (SIT) for providing financial support during my doctoral course.

Most importantly, I would like to thank my family Sravana Kumar, Pushpa Rani and Sai Susmitha, my colleagues, and friends, who kept me alive and motivated throughout this whole adventure.

Abstract

The objective of this thesis was to study the ways, how to improve critical current density (J_c) in polycrystalline magnesium diboride (MgB_2) bulk. The superconducting devices demand economical operation, cheap manufacturing routes, and lightweight. Considering the above-mentioned qualities, MgB_2 meets most of the criteria making it a promising candidate. Properties such as decent critical transition temperature (T_c), cheap and abundant raw materials, and light weight elements are appealing qualities for practical applications. It is also well known that MgB_2 thin films have high J_c (~ 10^7 to 10^8 A/cm^2) and upper critical field (H_{c2} ~ 60T at 0K). However, these values have been never seen in polycrystalline MgB_2 bulk; in fact, the J_c values are almost two orders of magnitude lower than those observed in thin films. The main reason is poor flux pinning, resulting in low H_{irr}, H_{c2} & J_c. Poor connectivity between grains and low density are the issue. Sintering has been a standard technique (700 to 850 ºC), resulting in good crystallinity and large grain size. Lack of flux pinning at grain boundaries and crystal defects led to considerable reduction of self-field J_c.

To tackle these issues, we tried to manipulate microstructure with various precursors. In this thesis, we fabricated MgB_2 bulk using solid state sintering at 775 ºC for 3 hours. Since, the melting point of boron is very high (~2000 ºC) compared to reaction temperature, boron precursor particle size plays a vital role in optimizing J_c. We used a commercial nano-amorphous boron and the results were astonishing. J_c of 408 kA/cm^2 was observed at 20K, self-field. SEM micrographs revealed the nano-sized grains in the final microstructure, which approved our hypothesis and was successful in improving self-field J_c. In order to improve the high field J_c and upper critical field H_{c2}, we resorted to carbon doping. One serious issue with the carbon doping was lack of homogeneous distribution of carbon in the matrix. To overcome this issue, we prepared carbon-encapsulated boron (CEB) made from pyrolysis of Diborane, hydrogen and gaseous hydrocarbon. It was found that low wt% of carbon coatings ensure the best results. A high-field J_c and H_{c2} were observed in 1.5 wt% carbon encapsulated boron based MgB_2 bulk. Tremendous J_c of 660 and 250 kA/cm^2 were observed at 0 and 2 T; 10 K. H_{c2} (calculated by extrapolation) was also substantially improved, being almost equivalent to the best records reported in MgB_2 bulk system so far, however at a slight expense of T_c. To further improve this result, our group studied the effect of co-dopants such Ag and CEB. Microstructural analysis exposed Ag-Mg phases formed in the

matrix and optimum performance was observed for 4 wt% Ag. To compensate the loss of Mg reacting with Ag, as well as to increase the Ag-Mg phase fraction, we studied the optimization of Mg precursor concentration. 7.5 wt% excess of Mg resulted in the best result, with highest Ag-Mg phase (2 wt%), high irreversibility field (H_{irr}) of 4.76 Tesla and large J_c such as 440 kA/cm^2 at 20 K, self-field. SEM analysis confirmed existence of secondary nano Ag-Mg phases (20-40 nm) which acted as pinning centers.

The special clean boron precursors first used were expensive, which might make the final product costly. In order to make the processing cheap while maintaining high performance, we explored a novel technique of high-energy ultra-sonication using various media such as ethanol, hexane, and distilled water. We successfully produced nano-sized boron via ultra-sonication, and arrived at high J_c in the final bulk. Beside size refinement, the obtained fine boron powder was free of B_2O_3, due to which the MgB_2 bulks were of high quality. SEM analysis clearly revealed that short duration of ultra-sonication results in particle refinement, while prolonged ultra-sonication causes agglomeration of boron particles. MgB_2 bulks fabricated from various systems were studied and the best results were observed in MgB_2 prepared with for 15 min ultra-sonicated boron dispersed in ethanol and for 30 min ultra-sonicated boron dispersed in distilled water. Self-field J_c of approximately 300 kA/cm^2 at 20 K was achieved (almost 35% improvement compared to a regular bulk MgB_2).

List of Publications

[1] **Arvapalli S S**, Muralidhar M, Pinmangkorn S, Jirsa M, Oka T, Sakai N and Murakami M
"Precise optimization of carbon-encapsulated boron doping for high-performance bulk sintered MgB_2"
J. of Adv. Eng. Mater. (2020) (In press) (article, referee reading)

[2] **Arvapalli S S**, Muralidhar M and Murakami M
"Size reduction of boron particles by high-power ultrasonication in ethanol media for optimization of bulk MgB_2"
J. of Superconductor Science and Technology (2020) (Under review) (article, referee reading)

[3] **Arvapalli SS**, Miryala M, Murakami M
"Ultrasonication-A cost effective way to high J_c bulk MgB_2" accepted for the publication at the book entitled "High T_c Superconducting Technology: Towards Sustainable Development Goals"
Jenny Stanford Publishing Pte. Ltd., Singapore (2020). In press

[4] Miryala M, **Arvapalli SS**, Murakami M
Development of MgB_2 superconducting super-magnets: Its utilization towards sustainable development goals (SDGs)" accepted for the publication at the book entitled "*High T_c Superconducting Technology: Towards Sustainable Development Goals"*
Jenny Stanford Publishing Pte. Ltd., Singapore, (2020). In press

[5] Jirsa M, Rameš M, Miryala M, Svora P, Duchoň J, Molnárová O, **Arvapalli S S**, Murakami M
Bulk MgB_2 doped by diverse additives -flux pinning and microstructure
J. of Superconductor Science and Technology (2020) In press (article, referee reading)

[6] J Noudem, Y. Xing, P. Bernstein, R. Retoux, M. Higuchi, **A. Sai Srikanth**, M. Muralidhar, M. Murakami
"Improvement of critical current density of MgB_2 bulk superconductor processed by Spark Plasma Sintering"
Journal of the American Ceramic Society (2020) In press (article, referee reading)

[7] Miryala Muralidhar; Sunsanee Pinmangkorn; Takemura Kento; **Arvapalli Srikanth Sai**; Jirsa Milos; Ramachandra Rao M; Oka Tetsuo; Sakai Naomichi; Murakami Masato

"Recent progress in production of infiltration-growth and melt-growth processed bulk (RE)$Ba_2Cu_3O_y$"
J. of Superconductor Science and Technology (2020**)** In Press (article, referee reading)

[8] Pinmangkorn S, Miryala M, **Arvapalli S S** and Murakami M
"Enhancing the superconducting performance of melt grown bulk $YBa_2Cu_3O_y$ via ultrasonically refined Y_2BaCuO_5 without PtO_2 and CeO_2"
J. of Mater. Chem. Phys. (2020) **Vol.244** pp.122721 (article, referee reading)

[9] Pinmangkorn S, Miryala M, **Arvapalli S S** and Murakami M
Effect of Ultra-sonicated Y_2BaCuO_5on Top-Seeded Melt Growth $YBa_2Cu_3O_y$ Bulk Superconductor
J. Supercond. Nov. Magn. (2020) doi.org/10.1007/s10948-019-05405-0 (article, referee reading)

[10] Pinmangkorn S, Miryala M, **Arvapalli S S** and Murakami M
"Y_2BaCuO_5 Particle Size Control via Ultrasonication and its Effect on Bulk $YBa_2Cu_3O_y$ Superconductor"
J. Phys. Conf. Ser. (2020) **Vo.773** pp.012017 (article, referee reading)

[11] Nurhidayah Mohd Hapipi, Muralidhar Miryala, Soo Kien Chena, **Sai Srikanth Arvapalli**, Masato Murakami, Abdul Halim Shaaria, Mohd Mustafa Awang Kechik, Kean Pah Lim, Kar Ban Tan, Oon Jew Le,
"Enhancement of critical current density for MgB_2 prepared using carbon-encapsulated boron with co-addition of Dy_2O_3 and La_2O_3 "
Journal of the American Ceramic Society (2020) In press (article, referee reading)

[12] **Arvapalli S S**, Miryala M and Murakami M
"Optimization of Mg Precursor Concentration to Obtain High J_c in MgB_2 Synthesized With Ag Addition and Carbon Encapsulated Boron"
J. of IEEE Trans. Appl. Supercond. (2019) **Vol.29** 8000904pp.4. (article, referee reading)

[13] **Arvapalli S S**, Miryala M and Murakami M
"Beneficial Impact of Excess Mg on Flux Pinning in Bulk MgB_2 Synthesized with Ag Addition and Carbon Encapsulated Boron"
J. of Adv. Eng. Mater. (2019) **Vol.21** 1900497 pp1-7. (article, referee reading)

[14] **Arvapalli S S**, Muralidhar M and Murakami M

"High-Performance Bulk MgB_2 Superconductor Using Amorphous Nano-boron"
J. of Supercond. Nov. Magn. **(**2019) **Vol.32** pp.1891-1895. (article, referee reading)

[15] Miryala M, **Arvapalli S S**, Diko P, Jirsa M and Murakami M
"Flux Pinning and Superconducting Properties of Bulk MgB_2 with MgB_4 Addition"
J. of Adv. Eng. Mater. (2019) **Vol.22** 1900750 pp.1–7 (article, referee reading)

[16] Hattori A, Muralidhar M, **Sai Srikanth A** and Murakami M
"Optimization of $YbBa_2Cu_3O_y$ thick Film Formation on MgO Substrates using Yb_2BaO_5 and liquid phase"
J. Phys. Conf. Ser. (2019) vol.1293 1–6 (article, referee reading)

[17] Longji Dadiel J, Muralidhar M, **Arvapalli S S**, Pavan Kumar Naik S and Murakami M
"Processing and Characterization of Charcoal Added Bulk MgB_2 Superconductor"
J. Phys. Conf. Ser. (2019) 1293 (article, referee reading)

[18] **Arvapalli S S**, Masato Murakami, and Miryala Muralidhar.
"SYNTHESIS AND CHARACTERIZATION OF SUPERCONDUCTING BULK MAGNESIUM DIBORIDE"
The 12th SEATUC Symposium Proceedings; (2018**)** OS12-02; pp 142-143.

Presentations:

[1] ***Oral Presentation,*** **Arvapalli S S** et al., Japan International Conference on Carbon Materials and Nanotechnology (JICCMAN-2020), Online.

[2] ***Poster Presentation***, **Arvapalli S S** et al., Green Innovation Symposium (2020), Japan (Tokyo, SIT)

[3] ***Oral Presentation***, **Arvapalli S S** et al., "11th International Workshop on Processing and Applications of Superconducting Bulk Materials" - PASREG (2019), Czech Republic (Prague)

[4] ***Poster Presentation***, Pinmangkorn S, M. Miryala, **Arvapalli S S** et al. "14th European Conference on Applied Superconductivity" – EUCAS (2019), UK (Glasgow).

[5] ***Oral Presentation***, Pinmangkorn S, M. Miryala, **Arvapalli S S** et al. "The 2nd International Conference

on Materials Research and Innovation" – ICMARI (2019), Thailand (Bangkok).

[6] **Plenary,** M. Muralidhar, **Arvapalli S S** et al., "The Phenomenal Role of Bulk High-T_c Superconductors in Day to Life Applications". 7th International Conference on Solid State Science & Technology" ICSSST 2019, November 11-13th, 2019, the Everly Hotel, Putrajaya, K. Lumpur, Malesia.

[7] **Invited,** M. Muralidhar, **Arvapalli S S** et al., Physics Lecture Series No. 10, Department of Physics, UPM, Malaysia, November 14, 2019.

[8] **Invited,** M. Muralidhar, S. Pinmangkorn, T. Kento; **Arvapalli S S** et al., "Recent progress in production of infiltration-growth and melt-growth processed bulk (RE)$Ba_2Cu_3O_y$". 11th International Workshop on Processing and Applications of Superconducting Bulk Materials" - PASREG (2019), Czech Republic (Prague)

[9] ***Oral Presentation,*** **Arvapalli S S** et al., "The 12th South East Asian Technical University Consortium - SEATUC (2018), Indonesia (Yogyakarta, UGM).

[10] ***Poster Presentation,*** **Arvapalli S S** et al., "The 31st International Symposium on Superconductivity" - ISS (2018), Japan (Tsukuba).

[11] ***Poster Presentation***, **Arvapalli S S** et al., "Applied Superconductivity Conference" - ASC (2018), US (Washington, Seattle)

[12] **Oral,** M. Muralidhar, Pavan, S. Pinmangkorn, **Arvapalli S S** et al., **"**High performance IG processed bulk YBCO produced with sharp-edge Y211 precipitates". Applied Superconductivity Conference (ASC 2018), October 28-November 2nd, Seattle, USA.

[13] **Keynote Speech,** M. Muralidhar, Sai et al., "Use of high-T_c superconducting technology in everyday life: Super-Magnets". World Congress on Material Research and Technology, October 22-23, 2018, Tokyo, Japan.

Table of contents

Chapter 1

Introduction

1.1 Superconductivity

1.1.1 Background

Superconductivity was first discovered in 1911 by H Kamerlingh Onnes (refer to Fig. 1.1(a)), which turned to be one the greatest discoveries in the history of science [1]. In fact Onnes was studying the resistance of solid mercury at cryogenic temperatures using his prior discovery, liquid helium (4.2 K) as a refrigerant where he had observed that the resistance abruptly disappeared as can be seen in Fig. 1.1(b).

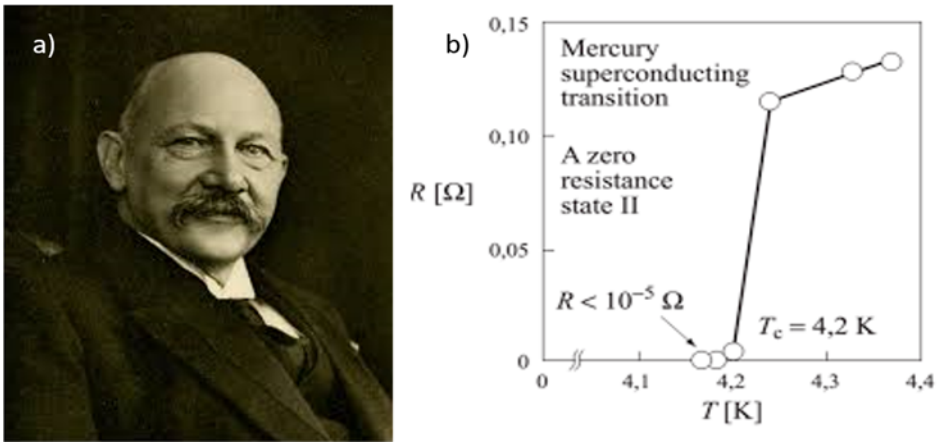

Fig. 1.1: a) H K Onnes portrait, b) Discovery of superconductivity in Hg at 4.2 K.

The main features of superconductors are

i) Sudden disappearance of electrical resistivity below characteristic temperature (also known as superconducting critical temperature- T_c) and

ii) Complete spontaneous expulsion of magnetic flux, which was later discovered by Walter Meissner and Robert Ochsenfeld in 1933 [2].

Their experiments found out that the flux was expelled because of the superconducting surface currents that are formed. These currents create magnetic fields that perfectly counter couple the applied magnetic field, popularly known as the 'Meissner effect'. Both fundamental properties of superconductors arise when they are cooled to cryogenic temperatures (below T_c). As a matter of fact, the applied magnetic field will penetrate slightly into the surface of the superconductor by a particular distance known as penetration depth (λ). For superconducting material to be in active state, it should be maintained at a temperature lower than T_c, restricted current density and subjected to limited magnetic field. For instance, in similar to T_c, there is a maximum current density and maximum magnetic field known as the superconducting critical current density (J_c) and the critical field (B_c) respectively. Fig. 1.2 depicts the three limiting parameters such as J_c, T_c, and H_c as axes and the restricted volume that defines the viability of superconductive nature.

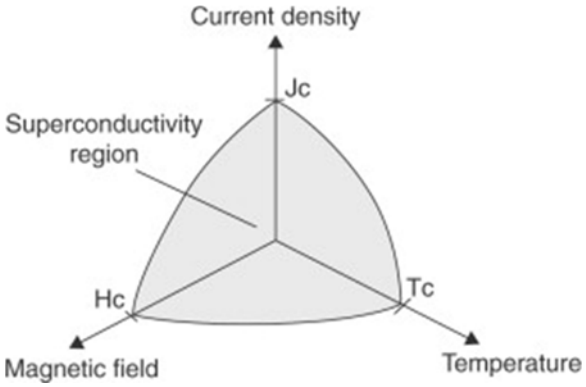

Fig. 1.2: Critical volume made from J_c, T_c and H_c as axes for maintaining superconducting state.

The superconducting state turns to normal state, should the state of material be outside the restricted volume made up of superconductor parameters as mentioned prior. Henceforth, working of a superconductor are bound by limited temperatures and magnetic fields, and can only carry a huge finite amounts of current, despite the zero resistance.

1.1.2 BCS theory

Bardeen-Cooper-Schrieffer (BCS) theory was used as basis for explaining this nature in most of the superconducting materials [3, 4]. According to this theory, electrons in the superconducting

state form Cooper pairs via an electron-phonon interaction. The energy for Cooper pairing is marginally lower than regular two-free-electron system, which allows a tiny energy gap above them. Although this energy gap a very small value (2Δ (0K) ~ 1 meV), it is enough for electrons to avoid collisions or interactions while moving which are responsible to resistivity. Therefore a superconductor exhibits zero resistivity when the thermal perturbation is less than the band gap. Many conventional LTS such as NbSn and NbTi can be explained using the BCS theory [5]. Using BCS theory the T_c can be assessed by the following equation 1.1:

$$T_c = \Delta(0K)/1.8\, k_B \tag{1.1}$$

k_B is the Boltzmann constant equivalent to 1.38×10^{-23} J/K). As the energy gap is a very small value, T_c's of the BCS-type superconductors in most of the cases tend to be lower or equal to 30 K.

A core characteristic parameter of Cooper pair is the coherence length (ξ), which is defined as the length of electron-electron spacing in Cooper pair. This length can be influenced by the mean free path of the electrons (l). ξ of a practical superconductor can be evaluated by the following equation 1.2:

$$1/\xi = 1/\xi_o + 1/l \tag{1.2}$$

Where ξ_o is the coherence length in theoretical perfect materials (assuming no defects and abnormalities). Finally, both the parameters i) penetration depth and ii) coherence length are the most vital parameters in superconductivity. Ginzburg-Landau (G-L) theory states the strong dependence of two factors in determining the maximum amount of the critical current density (J_c) and the critical field H_c [7, 8]. The dependence is as follows

$$J_c \propto 1/\lambda^2\xi \tag{1.3}$$

$$H_c \propto 1/\lambda\xi \tag{1.4}$$

In addition, there is another parameter known as Ginzburg-Landau parameter κ, which is ratio of penetration depth and coherence length. This ratio can aid in determining the type of superconductors.

$$\kappa = \lambda/\xi \tag{1.5}$$

1.1.3 Types of Superconductors

Coming to the types of superconductor, there are two types of superconductors in general, which are i) Type I superconductors and ii) Type II superconductors [5, 6]. Materials that ideally follow the Meissner Effect come under Type I superconductors. While, Type II superconductors are materials with greater Ginzburg-Landau parameter κ ($\kappa > 0.71$ for type II superconductors, and $\kappa < 0.71$ for type I superconductors) and also behave differently when magnetic field is applied. In brief, type I superconductors act as perfect diamagnetic materials i.e. they don't allow any magnetic flux through their bodies, however in type II superconductors the magnetic flux is partially allowed to enter through their body, creating quantized units of flux called fluxons (ϕ_o). All of the fluxons are aligned in the same direction to the applied field. Each fluxon is comprised of a cylindrical core with radius equivalent to coherence length (ξ), and a supercurrent along the periphery. The magnetic field emitted from the fluxon decays into the nearby area over a distance of λ. Since the superconductor in this state allows magnetic flux while still showing zero resistance, it is known as mixed state. This mixed state in type II superconductors exists until very high magnetic field. After certain high field known as the upper critical field (H_{c2}), the superconductor changes from the mixed state to the non-superconducting state as can be seen from Fig. 1.3.

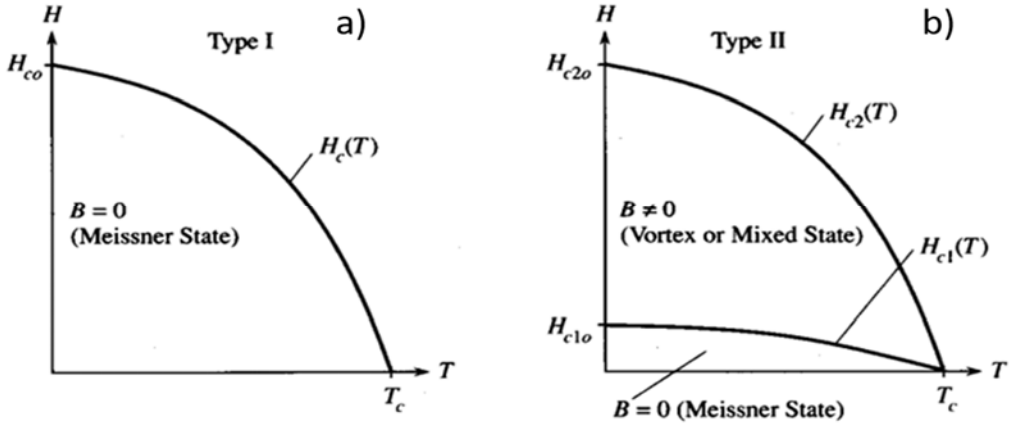

Fig. 1.3: Magnetic behavior of a) Type I superconductors and b) Type II superconductors

In a theoretical perfect type II superconductor the repulsive interactions between individual fluxons forces them to migrate and eventually lose the superconductive nature much faster. Yet, in a real superconducting material there are many defects such dislocations, vacancies, precipitates, and interfaces etc. that act as flux pinning centers that prevent fluxons from migrating [9]. Hence,

presence of more pinning centers improve the maximum H_{c2} value at which the superconductor becomes non-superconducting. In fact, this can be explicated by estimating energy change in the superconductor system. To create and grow a fluxon within the superconductor, an additional energy must be provided to the system. This additional energy is termed as 'condensation energy'. However, if the fluxon is overlaid on the pinning centers, the condensation energy essential to produce the fully grown fluxon core is minimized. Hence, the system comes to a lower energy state and becomes more stable than the normal system (without pinning centers) and therefore the flux becomes energetically pinned. Due to this stability, large J_c can be achieved at high fields and hence is vital for a superconducting material to have strong flux pinning capability. The properties of the flux pinning can be assessed by the bulk pinning force density (F_p) using equation 1.6

$$F_p = J_c \times B \tag{1.6}$$

As mentioned prior, various defects can act as pinning centers. However, pinning ability of a pinning center depends on the interaction between the pinning centers and the fluxons, especially on parameters such as the size of pinning centers. For optimum pinning performance the size of the pinning center should be close to the size of the fluxons (i.e. coherence length). Dew-Hughes [10, 11] has summarized the bulk flux pinning force densities in contrast to various types of pinning centers (classified by size and shape) in equations 1.7, 1.8 and 1.9:

$$\text{Volume pinning } (d < a, b, c) \quad f(h) \propto h^0(1-h)^2 \tag{1.7}$$

$$(d > a, b, c) \quad f(h) \propto h^1(1-h)^2 \tag{1.8}$$

$$\text{Surface pinning } (c < d < a, b) \quad f(h) \propto h^{0.5}(1-h)^2 \tag{1.9}$$

where, h is reduced magnetic field calculated by ($h = H/H_{c2}$; $0 \leq h \leq 1$) and f is normalized pinning force density ($f = F_p/F_{p,max}$; $F_{p,max}$ is the maximum pinning force) while *a, b, c* are the dimensions of the pinning centers and d is the inter-flux-line spacing. The reduced magnetic field dependence of the normalized pinning force density is solely judged by the flux pinning types and thus plotted as a single lined *f (h)* curve, independent of materials and temperatures. For instance, if the primary pinning in a superconductor is from grain boundaries, the *f (h)* curve plotted will be similar to $h^{0.5}(1-h)^2$ at all temperatures ($T < T_c$). These pinning curves *f (h)* as per the above mentioned equations have characteristic maximum that can be used to detect the primary flux pinning mechanism. In most of the cases, h is often estimated using H/H_{irr} (H_{irr} is the irreversibility field,

i.e. the critical field at which J_c decreases to a finite small value) instead of H/H_{c2} because H_{c2} can be very large in some superconductors that cannot be measured. Therefore improvement in H_{c2} and increasing the pinning centers are the two most universal ways to increase the effectiveness of flux pinning capability in a superconductor.

1.2 MgB_2 Superconductor

1.2.1 Discovery

Superconducting materials are not as enigmatic as they might seem. Over many years, thousands of materials [12, 13] are reported to exhibit superconducting properties. Based on their working temperatures and critical superconducting temperatures (T_c) superconductors can be classified into two types: i) high temperature superconductors (HTS) and ii) low temperature superconductors (LTS). Examples of some HTS are $YBa_2Cu_3O_y$ (YBCO) [14] and $Bi_2Ca_2Sr_2Cu_3O_{10}$ (Bi2223) [15], which can be functioned at temperatures above that of liquid nitrogen (77.3 K). Ripening of the cooling technology made it cheap to produce liquid N_2 environment. Despite the cost efficacy, various obstacles such as high magnetic anisotropy, brittle nature of materials and high cost of precursors, hinder their potential to realize practical applications. Simultaneously, in case of most typical LTS such as NbTi and Nb_3Sn with T_c's lesser than 20 K, require expensive liquid helium (4.2 K) as the coolant, which is economically unattractive. Research carried at the beginning of the 21st century delivered the superconductivity community with two new classes of superconductors: i) MgB_2 [16] and ii) iron-based superconductors [17-19], which have T_c's around 25-50 K. Hence, they are popularly known as medium temperature superconductors (MTS) [20].

Magnesium boride as a chemical was discovered in 1864 [21], well before superconductivity phenomena. However, superconductivity in magnesium diboride (MgB_2 – T_c ~ 39 K) was first reported in 2001 by Prof. J. Akimitsu et.al. [16]. This discovery was a slight shock considering that the chemical itself was discovered way long ago. After MgB_2 was first discovered, thorough studies on the crystal structure of MgB_2 as well as reaction mechanisms and chemistry was published. Although MgB_2 was a common compound accessible in many chemical laboratories and chemical supplying companies, cryogenic studies were not carried out on this compound until 2001, which led to a gap of almost 10 decades. Once discovered, scientists and technologists tried

to explore and understand the compound, the mechanisms responsible for superconductivity and advantages of this new intermetallic over other superconductors.

1.2.2 Highlights of MgB_2

MgB_2 has a simple structure and a comparatively high T_c compared to the traditional metallic superconductors (Nb_3Ge (T_c -23.2K) etc.) which ruled over superconductor research for quite some time. Highlights of this material are larger coherence length ($\xi \sim$ 5-12 nm) compared to these superconductors [22]. The upper critical magnetic field (H_{c2}) of doped MgB_2 is quite high which enables this material for magnetic applications [23-25]. MgB_2 in bulk form has high critical current density (J_c), as well as uniform trapped field properties which makes it an interesting candidate for technologists as it can be operated in the range 25 to 30 K [26]. To the present modern cryo-technology, this temperature range is easily attainable without the use of costly liquid He. MgB_2 has lower anisotropy and weak link free grain boundaries, unlike trending cuprates-based HTS. Since it is an intermetallic, it also exhibits low normal state resistivity [27]. Being made up of lighter elements, MgB_2 has quite low density, which in turn reduces the product's weight considerably [28]. This quality makes the material a robust contender for superconducting applications, especially in space applications where weight is of utmost importance [29]. Reduced production cost is the most attractive feature for the industrial sector [30]. Furthermore, Mg and B are precursors that are readily accessible unlike heavy metals and rare-earths which are primary constituents in other superconducting systems. The fabrication is also cost efficient because it needs comparatively less temperature and time for heat treatment. For example, in the case of high T_c cuprates, the heat treatment temperature is higher (1000 ^oC) and the duration is very long (more than 2 weeks). When considering tapes and wires, the sheath materials used for MgB_2 based superconductors can be cheap Fe, stainless steel etc. while in the case of cuprate superconductors it is costly Ag. This because in high T_c cuprates any other sheath material except Ag, will react with precursors and destroy superconducting properties as well T_c. Despite the low T_c, (well below the cuprate superconductors) much theoretical studies on MgB_2 were carried by researchers because of its modest crystal structure with sp orbital electrons involved in the superconducting mechanism, which is relatively simple and easy to handle theoretically.

1.2.3 Structural Properties of MgB_2

1.2.3.1 Crystal Structure

In 1954, Jones et al. [31] explored a Mg-B compound by high resolution neutron powder diffraction and X-ray diffraction (XRD) and identified the stoichiometry as MgB_2 thereby determining the crystal structure to be a hexagonal unit cell similar to that of AlB_2 [32, 33] (with lattice constants a = 3.0834 Å and c = 3.5213 Å). Later, these results were verified by contemporary techniques [34], which categorized MgB_2 into a P6/mmm space group, with Mg atoms occupying (0, 0, 0) sites and B taking (1/3, 2/3, 1/2) and (2/3, 1/3, 1/2) sites or Wyckoff positions. The hexagonal Boron atomic planes are intercalated within hexagonal Mg atomic planes, forming an alternative layered structure as shown in Fig. 1.4. The six-fold symmetry and the anisotropy of the crystal structure are exhibited in MgB_2 grains and single crystals.

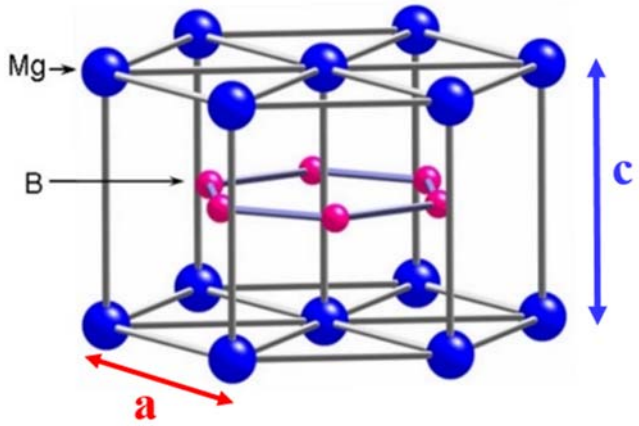

Fig. 1.4: Crystal structure of MgB_2 [35].

The intralayer B–B bond lengths are much shorter than the interlayer distance. In detail, the values are B-B intralayer = 0.1780 nm, Mg-Mg intralayer = 0.3084 nm, Mg-Mg interlayer = 0.3524 nm and Mg-B interlayer = 0.25 nm [36, 37]. Because of this in plane boron bonding, the MgB_2 system shows an anisotropic electronic structure. In one Mg-B bond, Magnesium are positive ions and boron atoms are negative ions. Hence, electrons move from Mg to the network of boron atoms (sheets or 2D layers). This shows that MgB_2 exhibits both ionic and covalent bonding characteristics, which enables the material to display novel superconducting properties.

1.2.3.2 Electronic Band structure

Despite having the similar structure to graphite, MgB_2 has quite different band structure such as conducting states with two superconducting band gaps. As mentioned, Mg atoms donate their valence electrons to the boron planes, which constitute the ionic bond characteristics. These in plane B atoms are bonded together via sturdy covalent bonds (2- Dimensional). While on the other side, the metallic bonds (3- Dimensional) are situated in the middle of these layers. In the bond formation, the sp^2 hybridized boron (comprised of 2s and $p_{x,y}$ orbitals) contributes to creation of partially filled 2D covalent sigma (σ) bands. The hole-bands formed by this are localized in the boron plane. While the p_z orbital contributes to creation of 3D metallic type pie (π) band which is delocalized. In this type of π band, not only the electrons but also the holes act as charge carriers [38]. Overall, these 2D-covalent sigma and 3D-metallic pie bands add to the total density of states (DOS) in the Fermi level [39-43]. The detailed band structure of MgB_2 can be observed from Fig. 1.5 [44], which was studied long before the uncovering of its superconducting nature [45].

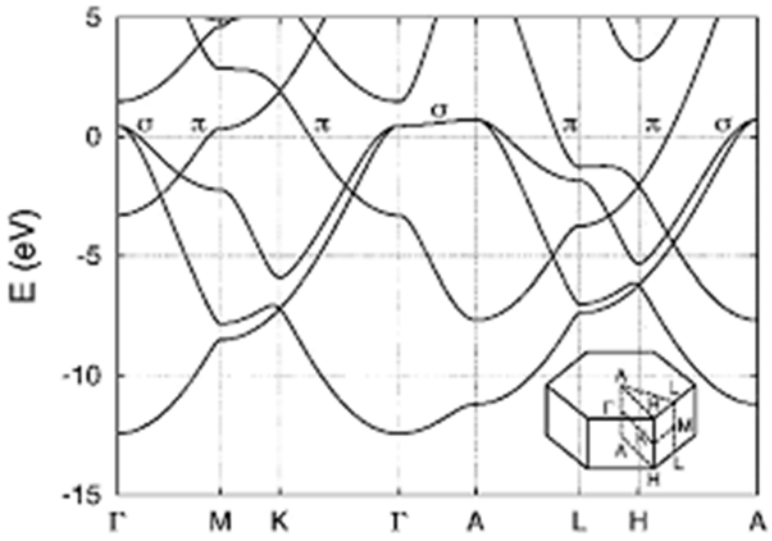

Fig. 1.5: Electronic band structure of MgB_2 superconductor

As mentioned earlier, the 3 σ bands formed from 2s, p_x, and p_y in the boron layer, and 2 π bands formed by boron p_z orbitals, very similar to that of graphite. In MgB_2, the valence bands are mainly made up of B bands unlike Mg, which does not have much contribution. The fermi surface is made from the hybrid boron electronic states. These bands join together at the Fermi surface at various positions of the Brillouin zone that is responsible for forming an interconnected tube kind of network. In this network, σ and π bands are greatly dispersive because of the huge overlap between

all p orbitals of nearby boron atoms [46]. Also, the interlayer overlaps such as $p_{x,y}$ orbitals are much less significant, which makes the k_z dispersion of σ bands less than 1 eV. For the above discussion, it is clear that the dispersion of the $\sigma p_{x,y}$ band is considerably different from the πp_z band. For instance, the most major dispersion in $\sigma p_{x,y}$ bands is observed along Γ-K, while the dispersion in major along Γ-A in πp_z bands. The σ bands are parallel to Γ-A and are placed slightly above the Fermi level. These bands also form two cylindrical hole type Fermi surfaces around the Γ-A line [47]. On the other hand, π bands form a pair of planar honeycomb like tubular networks similar to a bonding orbital (holes) placed at $k_z = \pi/c$ and an antibonding orbital (electrons) present at $k_z = 0$. Fig. 1.6 depicts the Fermi surface of MgB_2, where the straight up facing cylinders are related to σ bands, while the 3D tunnels are related to π bands. In the Fig. 1.6, the green and blue cylinders are related to $p_{x,y}$ bands (holes). While the blue tubular network comes from the bonding p_z bands, the red tubular network is related to antibonding p_z bands.

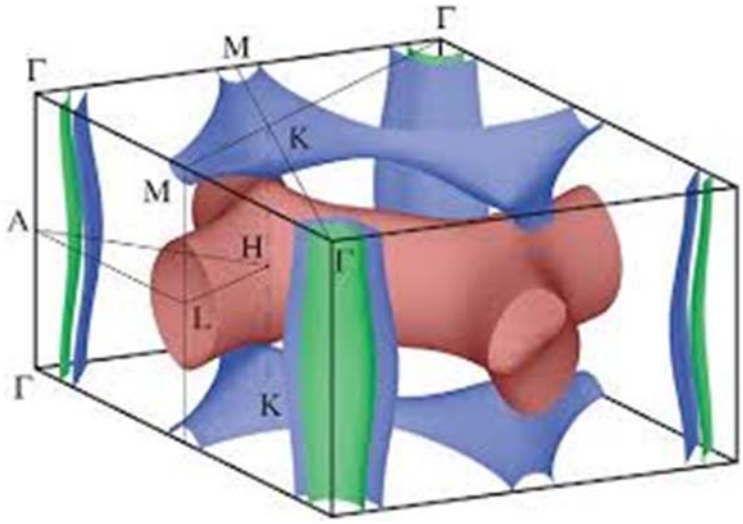

Fig 1.6: Fermi surface of MgB_2 superconductor

Theoretical estimations for predicting electronic structure of MgB_2 are well reinforced with experimental proofs. Angle Resolved Photoemission Spectroscopy (ARPES) is one of the most standard techniques to determine electronic band structure of any material. Although ARPES determine properties of very thin surface layers and so cannot always be considered reliable to represent the whole bulk's electronic structure. However, experimental results, mainly Fermi surface properties such as de Haas-van Alphen effect are in good agreement with the theoretical

calculations [48-51]. On the other hand, Nuclear Magnetic Resonance (NMR) is another way to study the electronic structure at Fermi level. NMR spectroscopy reveals primarily two properties related to electronic structure such as i) Knight shift and ii) Spin–lattice relaxation rate. Estimation of in-plane and out-of-plane Hall coefficients reveal that dominant carriers along the *a*-*b* plane are hole-type, while along c direction the dominant carries are electron type, showing the multiband nature of MgB_2 [52, 53]. These results are in agreement with theoretical predictions.

1.2.4 Superconducting Mechanism

The mechanisms explaining superconducting properties of MgB_2 was an intriguing research topic throughout the world, soon after the exposure of superconductivity in MgB_2. Since the T_c was close to the BCS theory estimations, influence of high-frequency phonons are assumed to be a vital part. Techniques such as isotope effect, Raman scattering, de Haas-van Alphen effect, inelastic neutron and inelastic X-ray scattering are popular for detecting the types and role of various phonon modes responsible for superconducting nature. After a lot of research, it is concluded that MgB_2 is a phonon-assisted BCS based superconductor involving selective coupling between specific phonons and specific electronic states. As per the BCS theory the superconducting transition temperature (T_c) is related with mass (M) via the following relation

$$M^{\alpha} \times T_c = k \tag{1.10}$$

Where k is a constant, while α is isotopic coefficient (α =1/2 in case of a simplified BCS model) [54]. Specimens prepared using the isotopes such as ^{10}B and ^{11}B are utilized for studying the change in transition temperature. These studies revealed that a shift of 1K was observed [58, 59]. Similar scenarios were observed in other electron–phonon interaction based conventional superconductors such as Mercury, lead etc. Complete information on isotopic shift has been elucidated based on phonon-mediated BCS superconductivity theory elsewhere [55]. After all the calculations, the projected isotope effect coefficients for both Mg and B are 0.02 and 0.3, respectively [56] which dictates that the B phonons are contributing more than Mg to the superconductivity. MgB_2 is the first superconductor to exhibit two distinct superconducting gaps such as one at ~ 2 meV and the other one at ~ 7 meV, which then disappear simultaneously at same T_c [57]. The reasons for two different superconducting band gaps are due to the weak coupling in

the 3D bands and strong electron coupling in the 2D bands. In addition, this nature in MgB_2 was experimentally supported by evidences from point contact spectroscopy, specific heat measurements and tunneling data [58, 59]. Overall, based on the results from various studies it is clear that MgB_2 is a BCS based superconductor unlike high T_c cuprates.

1.2.5 Superconducting and Structural Properties

MgB_2 has a brittle nature, similar to other HTS. In a regular polycrystalline bulk MgB_2, the grain size ranges from 10 nm to 10 μm [60]. As a result of its peculiar band structure, MgB_2 is anisotropic, especially between *a* and *c* axis. This is because of different bond strengths i.e. Mg-B bonds are weaker than the B-B bonds. The penetration depth (λ) of MgB_2 ranges from 100-140 nm at 0K, while the coherence length (ξ) is around 5-12 nm. One of the superior feature of MgB_2 is its large coherence length (greater than interatomic spacing), which makes the material unaffected by weak-link issue as seen in HTS superconductors.

In the family of borides, MgB_2 has the highest superconducting critical transition temperature (T_c). T_c of MgB_2, as a matter of fact any material, can be influenced by various factors likes type of synthesis, manipulating synthesis conditions, using dopants or additives, applying external pressure, applying magnetic field, disturbing crystal structure, creating crystal defects, introducing strain, irradiation with various sources, varying mass of the constituent atoms such as using isotopes etc. So far, many elements and compounds as substituents have already been studied in the MgB_2 system such as C, Al, Mn, Cu, Fe, Li, Na, Si, Zr, Ag, SiC etc. [61-71]. In most of the scenarios the value of T_c is always decreasing. T_c drop varies differently with different dopants, be it Mg site or B site. Based on dopant research done so far, C substitution at the B site and Al substitution at the Mg site are the most fruitful ones as they belong to neighboring elements/groups in periodic table although at cost of decrease in T_c. On the other hand, other elements form secondary phases instead of substitution, which acted as only obstacles for the super current flow therefore deteriorate superconducting performance. Even a scarce amount of impurities can reduce T_c drastically [72]. Pressure manipulation can influence the critical temperature of MgB_2. In BSC based superconductor, increase in pressure can generate alteration in phonon modes resulting a drop in T_c. In fact according to prior research T_c change of 1.6K can be observed with a change of 1 GPa pressure [73]. Elsewhere, bulk MgB_2 was irradiated using protons and neutrons in order to

generate disorders and defects which can aid as pinning centers to improve the superconducting performance, however the reduction in T_c was huge [74].

MgB_2 exhibits higher critical current densities (J_c) than conventional LTS as well as HTS superconductors. The lack of weak link issue makes it even exhibit high inter-grain J_c. Lots of parameters like microstructure, density, phase purity, heat treatment, flux pinning etc can hugely effect the critical current density value of MgB_2 bulk superconductor. As the J_c varies with applied external magnetic field, its value must be assessed at self-field (zero field) as well as high field before considering it for an application. In general, pristine MgB_2 exhibits low J_c and upper critical field because of poor flux pinning. Improving this aspect has been a popular research topic. In order to do so, lot of trials have been made so far to improve the flux pinning such as hot isostatic pressing (HIP) [75], Spark plasma sintering (SPS) [76], solid state sintering [77], quenching [78], magnetic field processing [79], irradiation [74], high energy ball milling [80], chemical doping [81] etc. of all the above mentioned techniques, chemical doping is the most efficient way because of its ease of execution.

Another way to increase flux pinning centers is to end up with secondary phases (via additives) in the final superconductor matrix, which alter the microstructural properties that aid in improving the H_{c2}, irreversibility field (H_{irr}) and enhance the J_c as well. So far humongous number of dopants were tested such as carbon allotropes [82], silicides [83], oxides [84], nano and submicron particles of metallic elements [85], etc. Of all materials, carbon allotropes and nano SiC [86] dopants were most successful in improving flux pinning centers along with H_{c2} and J_c, without substantial drop in T_c. Grain boundaries play a vital role on J_c and H_{c2} of the bulk MgB_2 as they considerably contribute to the flux pinning and act as weak links like in HTS. In brief, decrease in grain size causes increase in grain boundary interface will aid in improving prior mentioned properties of MgB_2 superconductor [87, 88]. One main disadvantage of this material is its porosity (almost 50% in a regular sintered specimen) as can be seen in Fig. 1.7.

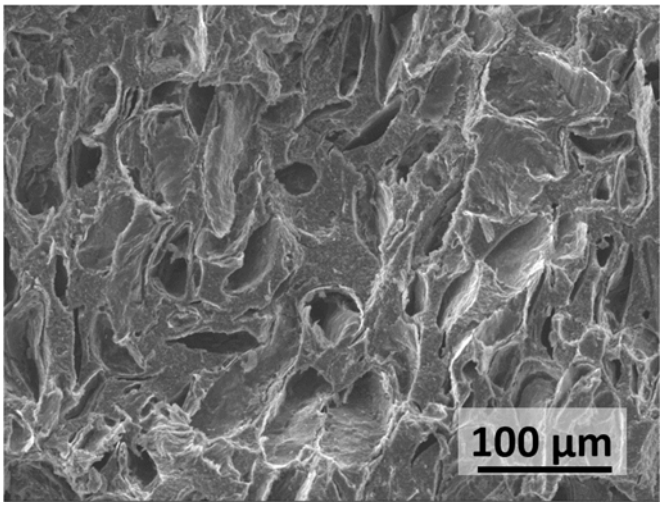

Fig. 1.7: low magnification SEM image of bulk MgB_2 (almost 50% porous).

Several techniques are being probed to counter this problem which include SPS, HIP, Mg diffusion etc. Another issue is formation of MgO (insulating in nature) that forms during sintering and usually responsible for decreasing J_c, however if tuned can come in hand as flux pinning centers. Present day superconductor applications demand different properties based on requirement such as high self-field J_c or good high-field J_c or high H_{c2} etc. unfortunately MgB_2 being superior over other superconductors have less high-field and self-field J_c (not high enough to comprise the cooling costs) and low H_{c2}.

1.2.6 Fabrication Techniques

Sintering:

The most commonly practiced fabrication technique is sintering. This technique is easy and can aid in mass producing required shapes and sizes. Also considered as the most economical way and hence used in most of the laboratories and companies. In this technique both the precursors are mixed together and subjected to a specific temperature to obtain final product. This technique has been optimized over several years. The phase diagram clearly illustrates the phases formed with the variation of Mg:B ratio (see Fig. 1.8). After severe research, it is concluded that 750 – 850 ^oC for about 3 hours was perfect temperature for producing good performance bulk [77].

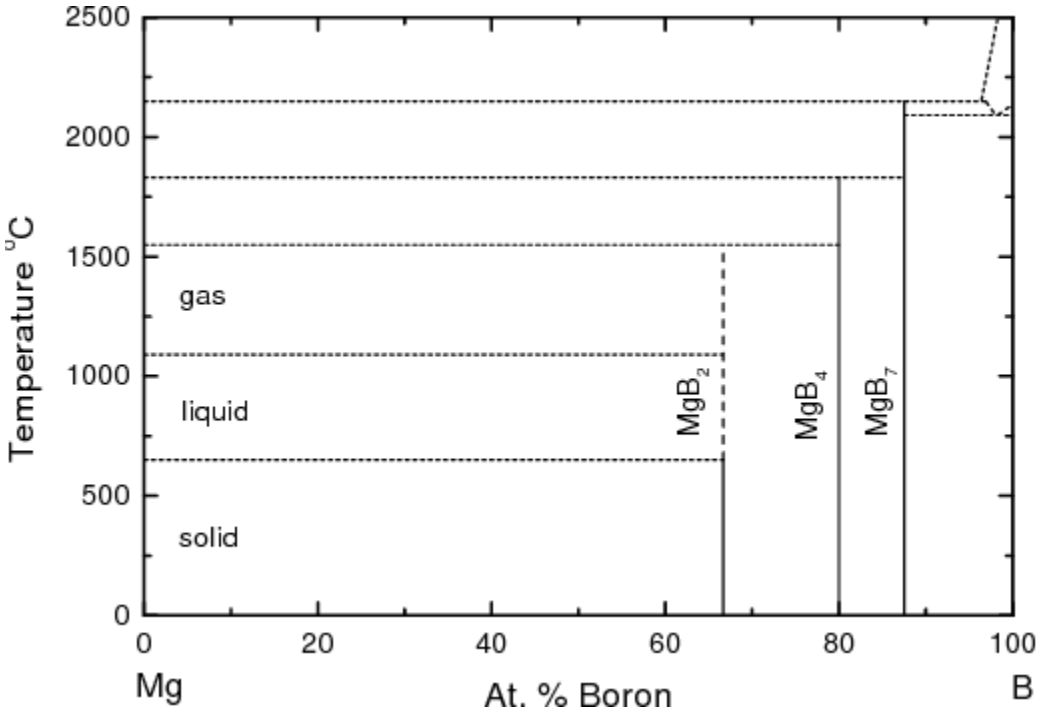

Fig. 1.8: Mg-B phase diagram [89].

Spark Plasma Sintering:

This is a pressure-assisted pulsed-current process in which the powder samples are loaded in an electrically conducting die and sintered under a high uniaxial pressure. Because of high pressure and local temperature, the density of end products is very high, which is necessary in case of bulk MgB_2 because of the porous nature. However, this technique is not optimized completely [76].

Diffusion technique:

In this technique Mg gas is allowed to flow through dense Boron matrix at reaction temperature which results in highly dense bulk. However there are issues such as non-uniformity due to incomplete diffusion till the center of the matrix, cracks probably due to volume issues or embrittlement [79].

Hot-Isostatic Pressing:

High dense MgB_2 bulks were prepared by the HIP method. However, over several years there were different types of HIP techniques

i) The powder mixture was kept in glass encapsulation (pressure, 200MPa; temperature, 1000 ºC over 200min; cooling under pressure) which is then used to synthesize bulk MgB_2 with diameters up to 20mm and thicknesses up to 10mm. This method can be scaled to larger sample sizes and complex shapes [75].

ii) Frist, the mixture was pressed into pellets by CIP (Cold Isostatic Pressing) method. Next, the pressed precursor pellets are sealed in the stainless steel container by Electron Beam Welding in vacuum. The sealed SS containers were set into the HIP machine and subsequently sintered at 900ºC for 3 hours under a pressure of around 980 MPa [90].

So far various techniques have been explored such as infiltration growth [91], chemical routes, ex-situ [92] etc. On the other hand, dopants, precursor refinement using Ball milling [81] etc. are one category of fabrication techniques. All of these techniques are utilized to improve the superconducting performance to commercializable level.

1.2.7 Applications

Although there are many superconducting materials discovered up till now, only a few of them are worthy enough to use in real applications. Till today, conventional low temperature superconductors such as Nb_3Sn and NbTi make up the majority of superconducting market because of good qualities such as decent critical current density, ductility, strength, easiness to fabricate into long wires etc. Efforts are being made to replace them with HTS superconductors and MgB_2 superconductors. Few main reasons for the industrial sector to show interest in MgB_2 are production, light weight and density (2.55 g/cm^3), cost effectiveness (both Mg and B are abundant and cheap), robustness of material etc. From prior discussion we know that MgB_2 is anisotropic, however is very less when compared to trending HTS. Hence MgB_2 unlike HTS doesn't require an extra texturing step in processing. Certain sectors such as space application have huge interests because of how light MgB_2 can be. All above mentioned features and advantages make MgB_2 a strong candidate for making superconductors that can be readily used in real-world applications. It is always advised that for optimum performance the superconductors must be used quite below T_c. In case of MgB_2 the most suitable operating temperature is around 20-30 K which can be achieved easily using present cryocooler technology or liquid hydrogen which can avoid the use

of very expensive liquid helium. MgB_2 is the most promising material for high field magnets application in place of Nb_3Sn and NbTi as the technology for them is materialized and MgB_2 can just fit in. Apart from the magnet applications such as NMR, MRI, water cleaning etc. [93, 94], MgB_2 superconductor has potential uses in superconducting transformers, rotors and transmission cables, etc. [95, 96].

1.2.8 Motivations and Objectives

From the above introduction a brief understanding of basic superconductivity and MgB_2 bulk system elucidates that this material has a great potential to become a commercial product for tackling real-world crisis and problems. However, we can also understand that there are some issues that need to be solved in order to successfully proceed further with this bulk system. Issues include limited upper critical field B_{c2}, requirement for strong flux pinning and high porosity. The porosity and connectivity issue can be solved by exploring various techniques mentioned in 1.2.6. From the J_c values of MgB_2 films [97, 98], it is clear that bulk has not reached its best performance yet. From prior research it is known that grain refinement is key to increase the flux pinning force [99-101]. Hence exploring various novel techniques to achieve this refinement will be a part of this work. Simultaneously, maintaining cost efficiency to product realization is important and therefore exploring cheap and scalable techniques will inherently be a part of this work. Improvement of H_{c2} was studied with various dopants, and carbon was supposed to be the best for doing so. However there has been an inhomogeneity issues in the bulk MgB_2 and solving this issue which will be another part of this work.

The main objectives of the thesis are as follows:

- To improve the self-field and high field critical current density (J_c) of superconducting bulk MgB_2 for magnet application via grain refinement and suitable dopants.
- To tackle the inhomogeneity problems such as C-substitution and Mg deficiency in the silver added bulk MgB_2.
- To employ novel, cheap and scalable technique such as high energy ultrasonication and optimize the parameters for producing high performance bulk MgB_2.

1.3 References

[1] Kammerlingh Onnes, *Leiden Comm* **1911**, 120b, 124c.

[2] W. Meissner, R. Ochsenfeld, *Naturwiss* **1933**, 21, 787.

[3] J. Bardeen, L.N. Cooper, J.R. Schrieffer, *Phys. Rev.,* **1957**, 106, 162.

[4] J. Bardeen, L.N. Cooper, J.R. Schrieffer, *Phys. Rev.,* **1957**, 108, 1175.

[5] D.K. Finnemore, "Superconductivity: type I and II", in Engineering Superconductivity, edited by P.J. Lee, **2001**, *John Wiley & Sons, Inc*., New York.

[6] A.C. Rose-Innes, E.H. Rhoderick, "Introduction to superconductivity," **1969**, *Pergamon Press*, New York.

[7] M. Eisterer, *Supercond. Sci. Technol*., **2007**, 20, R47.

[8] P.L. Ginzburg, L.D. Landau, Zhur. Eksperin. *Theoret. Fiz.,* **1950**, 20, 1064.

[9] S.R. Foltyn, L. Civale, J.L. MacManus-Driscoll, Q.X. Jia, B. Maiorov, H. Wang, M. Maley, *Nature Mater*., **2007**, 6, 631.

[10] D. Dew-Hughes*, Philos. Mag.,* **1974**, 30, 293.

[11] . Dew-Hughes, *Philos. Mag.,* **1987**, 55, 459.

[12] Y. Iwasa, "Case Studies in Superconducting Magnets: Design and Operational," **1994**, *Plenum Press*, New York.

[13] B.W. Roberts, *J Phys Chem Ref Data*, **1976**, 5, 581.

[14] M.K. Wu, J.R. Ashburn, C.J. Torng, P.H. Hor, R.L. Meng, L. Gao, Z.J. Huang, Y.Q. Wang, C.W. Chu, *Phys. Rev. Lett.* **1987**, 58, 908-910.

[15] J.M. Tarascon, W.R. McKinnon, P. Barboux, D.M. Hwang, B.G. Bagley, L.H. Greene, G.W. Hull, Y. Lepage, N. Stoffel, M. Giroud, *Phys. Rev. B*, **1988**, 38, 8885-8892.

[16] J. Nagamatsu, N. Nakagawa, T. Muranaka, Y. Zenitani, J. Akimitsu, *Nature*, **2001**,410, 63.

[17] Y. Kamihara, H. Hiramatsu, M. Hirano, R. Kawamura, H. Yanagi, T. Kamiya, H. Hosono, *J. Am. Chem. Soc.,* **2006**, 128, 10012.

[18] Y. Kamihara, K. Watanabe, M. Hirano, H. Hosono, *J. Am. Chem. Soc.,* **2008**, 130, 3296.

[19] K. Takahashi, K. Igawa, K. Arii, Y. Kamihara, M. Hirano, H. Hosono, *Nature*, **2008**, 453, 376.

[20] B.A. Glowacki, "Development of Nb-based conductors", in Frontiers in Superconducting Materials, edited by A.V. Narlikar **2005** *Springer*, Berlin.

[21] T L Phipson, *R. Soc. London*, **1864**,13, 217.

[22] W Martienssen, H Warlimont Springer Handbook of Condensed Matter and Materials Data, **2005**, *Springer*, Berlin.

[23] X S Huang, W Mickelson, B C Regan, A Zettl, *Solid StateCommun*, **2005**, 136, 278.

[24] R H T Wilke, S L Budko, P C Canfield, D K. Finnemore, S T Hannahs, *Physica C*, **2005**, 432, 193.

[25] M Bhatia, M D Sumption and E W Collings, *IEEE Trans. Appl.Supercond*, **2005**, 15, 3204.

[26] Y Wang, Fundamental Elements of Applied Superconductivity, **2013**, *John Wiley & Sons*, Singapore.

[27] W K Yeoh, J Horvat, J H Kim, X Xu, S X Dou, *Appl. Phys. Lett.,* **2007**, 90, 122502.

[28] D L Perry, Handbook of Inorganic Compounds, Second Edition, **2011**, *Taylor & Francis Group*, United States of America.

[29] W Goldacker, S I Schlachter, B Obst, M Eisterer, *Supercond. Sci. Technol.,* **2004**, 17, 490.

[30] P Grant, Potential electric power applications for magnesium diboride, *Mat. Res. Soc. Symp. Proc*., **2001**, 689, 3.

[31] R.C. Ray, *J. Chem. Soc*., **1914**, 105, 2162

[32] M.E. Jones and R.E. Marsh, *J. Am. Chem. Soc*., **1953**, 76, 1434.

[33] E.J. Felten, *J. Am. Chem. Soc.,* **1956**, 78, 5977.

[34] J.-Q. Li, L. Li, Y.-Q. Li, Z.-A. Ren, G.-C. Che, Z.-X. Zhao, *Chin. Phys. Lett*., **2001**, 18, 680

[35] Cristina Buzea et al, *Supercond. Sci. Technol*, **2001**, 14, 115

[36] M E Jones and R Marsh, *J. Am. Chem. Soc*., **1953**, 76, 1434.

[37] C Buzea and T Yamashita, *Supercond. Sci. Technol*, **2001**, 14, R115.

[38] K D Belashchenko, M Van Schilfgaarde, V P Antropov, *Phys. Rev. B*, **2001**, 64, 092503.

[39] M Pissas, Low-Dimensional Solids, (Ed. D W Bruce, D O'Hare, R I Walton), **2010***, John Wiley & Sons*, United Kigdom.

[40] J Kortus, I I Mazin, K D Belashchenko, V P Antropov, L L Boyer, *Phys. Rev. Lett*., **2001**, 86, 4656.

[41] M E Zhitomirsky and V H Dao, *Phys. Rev. B*, **2004**, 69054508.

[42] S C Erwin and I I Mazin, *Phys. Rev. B*, **2003**, 68, 132505.

[43] M Mansor and J P Carbotte, *Phys. Rev. B*, **2005**, 72, 024538.

[44] H J Choi, S G Louie and M L Cohen, *Phys. Rev. B*, **2009**, 79, 094518.

[45] I I Tupitsyn, Sov. *Phys. Solid State*, **1976**, 18, 1688

[46] I I Mazin and Antropov*, Physica C*, **2003**, 385, 49.

[47] N I Medvedeva, A L Ivanovskii, J E Medvedeva, A J Freeman*, Phys. Rev. B*, **2001**, 64, 020502.

[48] V D P Servedio, S L Drechsler, T Mishonov, *Int. J.Mod. Phys. B*, **2002**, 16, 1613

[49] H Uchiyama, K M Shen, S Lee, A Damascelli, D H Lu, D L Feng, Z X Shen and S Tajima, *Phys. Rev. Lett*. **2002**, 88, 157002.

[50] I Askerzade, Unconventional Superconductors: *Anisotropy and Multiband Effects*, **2012**, *SpringerVerlag*, Berlin.

[51] N W Ashcroft, D N Mermin, *Solid State Physics*, **2003**, *Thomson Learnin*g, India.

[52] Y Eltsev, K Nakao, S Lee, T Masui, N Chikumoto, S Tajima, N Koshizuka, M Murakami, *Phys. Rev. B*, **2002**, 66, 180504.

[53] T Masui, S Lee and S Tajima, *Phys. Rev. B*, **2004**, 70, 024504.

[54] C P Poole, H A Farach, R J Creswick, R Prozorov, *Superconductivity,* **2007***, Elsevier*, London.

[55] P C Canfield, S L Budko, D K Finnemore, Physica C, **2003**, 385, 1.

[56] D G Hinks, J D Jorgensen, *Physica C*, **2003**, 385, 98.

[57] M Iavarone, G Karapetrov, A E Koshelev,W K Kwok, G W Crabtree,W N Kang, E M Choi, H J Kim, S I Lee, *Supercond. Sci. Technol.,* **2004**, 17, S106.

[58] H D Yang, J Y Lin, H H Li, F H Hsu, C J Liu, S C Li, R C Yu, C Q Jin*, Phys. Rev. Lett*., **2001**, 87, 167003.

[59] S Tsuda, T Yokoya, Y Takano, H Kito, A Matsushita, F Yin, J Itoh, H Harima and S Shin, *Phys. Rev. Lett.,* **2003**, 91, 127001.

[60] S Jin, H Mavoori, C Bower, R B V Dover, *Nature*, **2001**, 411, 563.

[61] Paranthaman, M., Thompson, J. R., Christen, D. K., *Physica C: Superconductivity,* **2001***,* 355(1-2), 1–5.

[62] Luo, H., Li, C. M., Luo, H. M., Ding, S. Y. *Journal of Applied Physics,* **2002**, 91(10), 7122.

[63] Gonnelli, R. S., Daghero, D., Ummarino, G. A., Tortello, M., Delaude, D., Stepanov, V. A., Karpinski, *J Physica C: Superconductivity,* **2007**, 456(1-2), 134–143.

[64] Tampieri, A., Celotti, G., Sprio, S., Rinaldi, D., Barucca, G., Caciuffo, R. *Solid State Communications,* **2002**, 121(9-10), 497–500.

[65] I Pallecchi *et al*, *Supercond. Sci. Technol.,* **2009**, 22**,** 095014.

[66] P Toulemonde *et al*, *Supercond. Sci. Technol.,* **2003**, 16**,** 231.

[67] Sudesh *et al*, *Supercond. Sci. Technol.,* **2013**, 26**,** 095008.

[68] Bumin, D., Yanmaz, E., Basoglu, M. *et al. J Supercond Nov Magn,* **2011**, 24**,** 211–215.

[69] M. Muralidhar, K. Inoue, M.R. Koblischka, A. Murakami, M. Murakami, *J. Adv. Eng. Mater.* **2015**, *17*, 831

[70] Wang, X. L., Soltanian, S., James, M., Qin, M. J., Horvat, J., Yao, Q. W., … Dou, S. X, *Physica C: Superconductivity*, **2004**, 408-410, 63–67.

[71] Feng, Y., Zhao, Y., Pradhan, A. K., Cheng, C. H., Yau, J. K. F., Zhou, L., … Murakami, M, *Journal of Applied Physics,* **2002**, 92(5), 2614–2619.

[72] D W Gu, Y M Cai, J K F Yau, Y G Cui, T Wu, G Q Yuan, L J Shen, X Jin, *Physica C*, **2003**, 386, 643.

[73] B Lorenz, R L Meng and C W Chu, *Phys. Rev. B*, **2001**, 6401, 2507.

[74] R Gandikota, R K Singh, J Kim, B Wilkens, N Newman, J M Rowell, A V Pogrebnyakov, X X Xi, J M Redwing, S Y Xu, Q Li, B H Moeckly, *Appl. Phys. Lett.,* **2005**, 87, 072507.

[75] S.S. Indrakanti, V. F. Nesterenko, M. B. Maple, N. A. Frederick, W. H. Yuhasz, Shi Li, *Philosophical Magazine Letters*, **2001**, 81:12, 849-857474.

[76] Kang D K, Kim D W, Choi S H, Kim C A, Ahn I S, *Metal. Mater. Intern*, **2009**, 15, 15

[77] M Mustapić, J Horvat, M S Hossain, Ž Skoko, S X Dou, *Superconducting science and Technology,* **2013**, vol. 26 (7).

[78] Lin Ye *et al*, *Supercond. Sci. Technol.*, **2007**, 20**,** 621.

[79] S X Dou *et al*, *Appl. Phys. Lett*., **2006**, 89, 202504.

[80] Lee, J. H., Shin, S. Y., Kim, C.-J., Park, H. W, *Journal of Alloys and Compounds,* **2009**, 476(1-2), 919–924.

[81] C.H. Cheng, Y. Zhao, X.T. Zhu, J. Nowotny, C.C. Sorrell, T. Finlayson, H. Zhang, *Physica C: Superconductivity,* **2003**, 386, 588-592.

[82] C H Cheng *et al*, *Supercond. Sci. Technol.,* **2003**, 16**,** 1182.

[83] E W Collings *et al*, *Supercond. Sci. Technol.*, **2008**, 21, 103001.

[84] Perner, O., Häßler, W., Eckert, J., Fischer, C., Mickel, C., Fuchs, G., Schultz, L, *Physica C: Superconductivity and Its Applications,* **2005**, 432(1-2), 15–24.

[85] Kimishima, Y., Okuda, T., Uehara, M., Kuramoto, T, *Physica C: Superconductivity and Its Applications,* **2007**, 463-465, 286–289.

[86] Bumin, D., Yanmaz, E., Basoglu, M. *et al, J Supercond Nov Magn*, **2011**, 24**,** 211–215.

[87] S G Jung, W K Seong and W N Kang*, J. Appl. Phys.,* **2012**, 111, 053906.

[88] G Giunchi, G Ripamonti, S Raineri, D Botta, R Gerbaldo, R Quarantiello, *Supercond. Sci. Technol.,* **2004**, 17, S583.

[89] T. Massalski "Binary Alloy Phase Diagrams", *A.S.M International*, Materials Park, OH, **1990**, 2nd ed.

[90] J Zou *et al*, *Supercond. Sci. Technol.,* **2015**, 28**,** 075009.

[91] A G Bhagurkar *et al*, *Supercond. Sci. Technol.,* **2015**, 28**,** 015012.

[92] Hiroya Tanaka *et al*, *Supercond. Sci. Technol.,* **2012**, 25**,** 115022.

[93] Nakamura, T., Tamada, D., Yanagi, Y., Itoh, Y., Nemoto, T., Utumi, H., Kose, K., *Journal of Magnetic Resonance*, **2015**, 259, 68–75.

[94] Shigehiro Nishijima *et al*, *Supercond. Sci. Technol.,* **2013**, 26**,** 113001.

[95] Tixador, P., *Advances in Science and Technology,* **2006**, 47, 195–203.

[96] Ballarino, A., Bordini, B., Giannelli, S., *MgB_2 Transmission Lines for the Large Hadron Collider. MgB_2 Superconducting Wires,* **2016**, 581–591.

[97] X X Xi, *Supercond. Sci. Technol.,* **2009**, 22, 043001.

[98] Moon, S. H., Yun, J. H., Lee, H. N., Kye, J. I., Kim, H. G., Chung, W., Oh, B., *Applied Physics Letters,* **2001**, 79(15), 2429–2431.

[99] Masaya Takahashi *et al*, *Supercond. Sci. Technol.,* **2009**, 22**,** 125017.

[100] W Häßler *et al*, *Supercond. Sci. Technol.,* **2006**, 19, 512.

[101] Wang, J., Shi, Z. X., Lv, H., & Tamegai, T., *Physica C: Superconductivity and Its Applications,* **2006**, 445-448, 462–465.

Chapter 2

Experimental

2.1 Synthesis

2.1.1 Production of Bulk MgB_2

Polycrystalline bulk MgB_2 pellets were fabricated via in-situ sintering Mg and B powders (along with dopants or additives, if any). These powders were thoroughly mixed and ground in a glove box (Ar atmosphere) in the ratio of 1:2 of Mg:B. This mixture was then pressed into pellets of 20mm in diameter, 7mm in thickness using a uniaxial press with a force of approximately 20 kN. These pellets were immediately wrapped by Titanium (Ti) foils and heat treated in a tube furnace in Ar atmosphere. The samples were sintered at an optimized temperature of 775 ^oC in a tubular furnace. The sintering soaking time was 3 hours (see Fig. 2.1). The temperature is initially increased to 775 ^oC and finally decreased to room temperature (RT) at a rate of 100 ^oC /h. The pellets after taking out of the furnace were polished to remove outer layer of any possible MgO, which are then used for further characterizations.

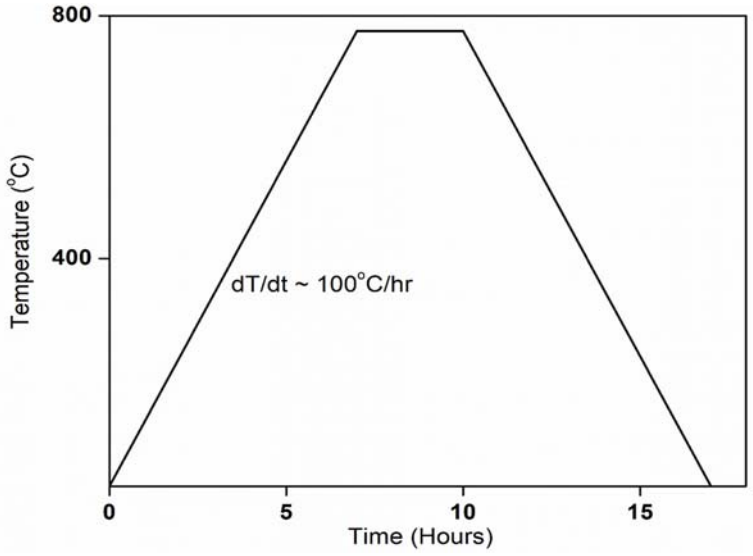

Fig. 2.1: Heat pattern for sintering bulk MgB_2 superconductor.

2.1.2 High Energy Ultrasonication

The working principle of this technique is that it generates powerful waves using vibration from a metal probe. These high energy waves cause turbulence in the medium and pass the high energy to the particles, which then bombard each other and the container walls, resulting in a sharp breakage. Tiny air bubbles are formed, releasing destructive forces inside the solution, which aid in splintering the particles. An important advantage of this method is that the waves' generation can be controlled and optimized by tuning frequency and power. Fig. 2.2 shows the clear schematic of the ultrasonication process. In this, we employed Mitsui UX-300 Ultrasonic Homogenizer.

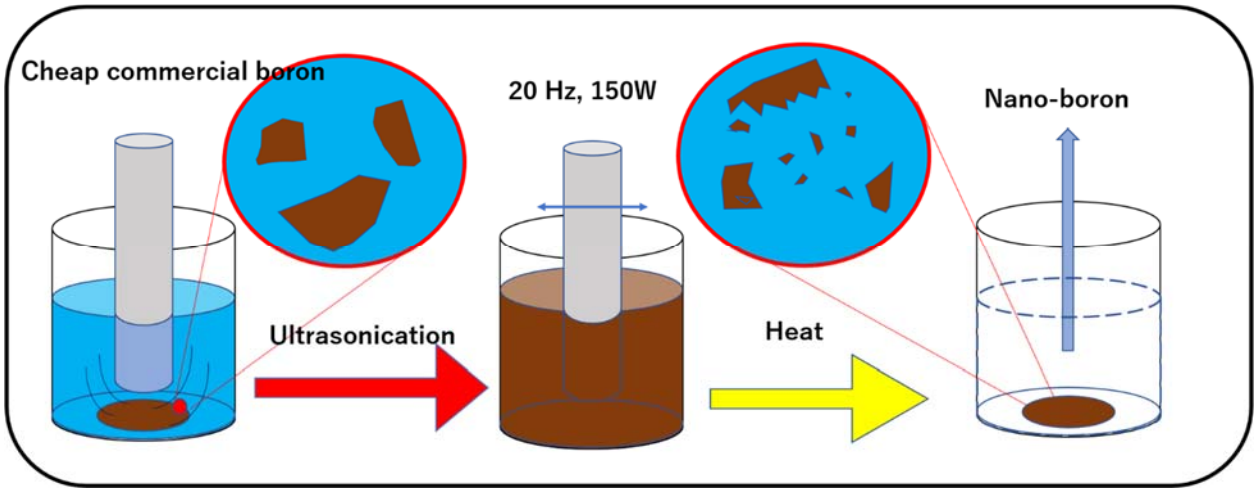

Fig. 2.2: Schematic of the particle refinement using high-energy ultrasonication.

2.2 Characterization Techniques

2.2.1 X-ray Diffraction (XRD)

In 1913, English physicists Sir William Henry Bragg and his son Sir William Lawrence Bragg explained why the cleavage faces of crystals reflect the incident X-ray beams at particular angles where they undergo constructive interference (see in Fig. 2.3). The relationship was named after them known as Bragg's law, as shown in equation 2.1 [1].

$$n\lambda = 2d\ sinn(\theta) \tag{2.1}$$

The variable d is the distance between atomic layers in a crystal, and the variable λ is the wavelength of the incident X-ray beam; n is an integer. This observation was an illustration of X-

ray wave interference, now known as X-ray diffraction (XRD), and was direct confirmation of the periodic atomic structure of crystals postulated over several centuries. Although Bragg's law was used to explain the interference pattern of X-rays scattered by crystals, diffraction has been developed to study the structure of all states of matter with any beam, e.g., ions, electrons, neutrons, and protons, with a wavelength similar to the distance between the atomic planes.

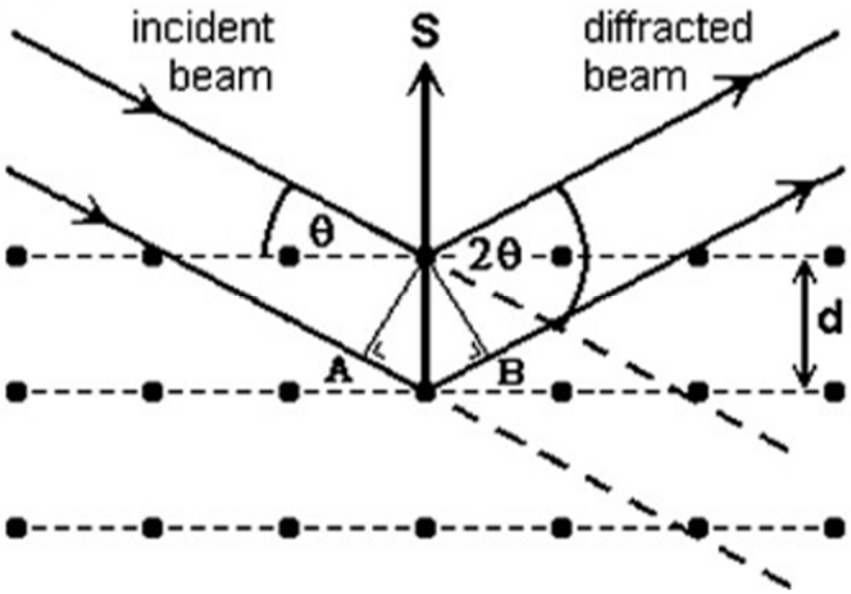

Fig. 2.3: Schematic view of x-ray diffraction illustrating the constructive interference for Bragg diffraction.

Further, there is a simple and well-known equation for measuring the crystallite size from X-ray diffraction peaks, known as the Scherrer equation (equation 2.2).

$$D = K\lambda/\beta cos\theta \tag{2.2}$$

Where D is the average crystallite size, K is shape factor (~0.9), λ is X-ray wavelength, β is full width at half maximum (FWHM) of the peak, and θ is Bragg angle. This equation was named after Paul Scherrer. However, there is a limitation regarding the application of this expression; the crystallite size must be in sub-micron range. In addition, external software must be used for performing Rietveld refinement followed by phase fraction calculations from XRD pattern. In this work, we employed MAUD (Materials Analysis Using Diffraction) for refinement and phase fraction calculations.

2.2.2 Scanning electron microscopy (SEM) and Energy dispersive analysis of X-rays (EDAX)

Electron microscopy is a scientific characterization technique that uses a beam of electrons to create an image of a sample under study. This setup is placed in vacuum, to avoid interference of electron beam with molecules present in air. Several electromagnetic lenses are used to focus the electron beam and magnify the images. In general, SEM is capable of investigating surface morphology and can magnify the image by several folds [2, 3]. The science behind is that, when the electron beam is projected on the sample at desired position and usually scans the surface. There are several ways how electrons interact with the sample. After beam collision with sample surface, electrons are either absorbed or scattered by the specimen, while emitting characteristic X-rays, secondary electrons, Auger electrons and backscattered electrons as illustrated in Fig. 2.4 [4]. Each type of electrons holds a specific information regarding the sample. For example, secondary electrons detected by SEM generate the image. Both the secondary and Auger electrons have relatively low energy as they arise from atoms close to the specimen surfaces. When X-rays are released, their spectral data carry a specific information regarding individual elements; it is employed for identification of chemical structure by EDAX [5]. The application of scanning electron microscope in conjunction with Energy Dispersive analysis of X-ray (SEM-EDAX) is a powerful tool for characterization of complex materials. The combined use of SEM-EDAX is a way to study and understand the structural and compositional complexity of the samples. The SEM used in this work is Field Emission Scanning Electron Microscope FESEM; JEOL; JSM-7100F.

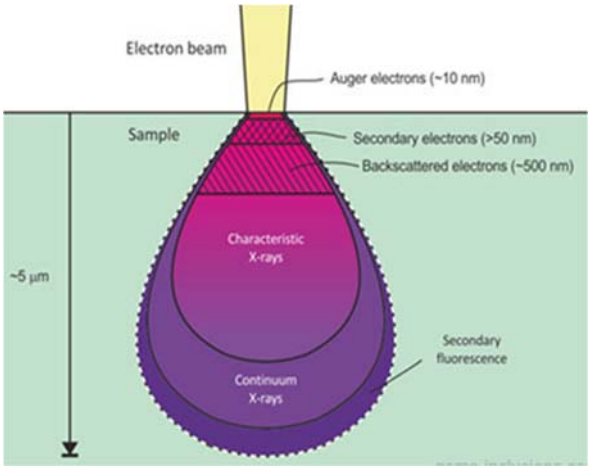

Fig. 2.4: Cross-section of electron beam-specimen interaction; Scanning Electron Microscope.

2.2.3 Transmission electron Microscopy

Transmission electron microscopy (TEM) is one of the most sophisticated instruments for analyzing the internal morphology or structure, spatial distribution of the various phases, dark field/bright field images, selected area diffraction and views of the defect structure through direct visualization. In TEM, the beam of electrons is transmitted through a specimen to form an image. Electrons interact strongly with atoms via elastic and inelastic scattering as shown in Fig. 2.5 [6]. Hence, to enable electrons to transmit the specimen, it must be very thin, around 5–100 nm for 100 keV electron beam. The thickness of the sample varies depending on the density and elemental composition of the specimen. Elastic scattering of electrons in a highly localized region makes it possible to obtain a large resolution. Inelastic scattered electrons are not localized. During elastic scattering, the electron beam trajectory slightly shifts because of interaction with electrostatic potential of nuclei. Since there is no huge momentum loss, the whole electron beam returns to the detector to form the image. In the case of inelastic collision, the energy of electrons in the beam is transferred to specimen, causing various effects such as excitation or ionization or lattice vibrations etc. [7]. In this work, transmission electron microscope TEM JEOL/ JEM-2100 was used.

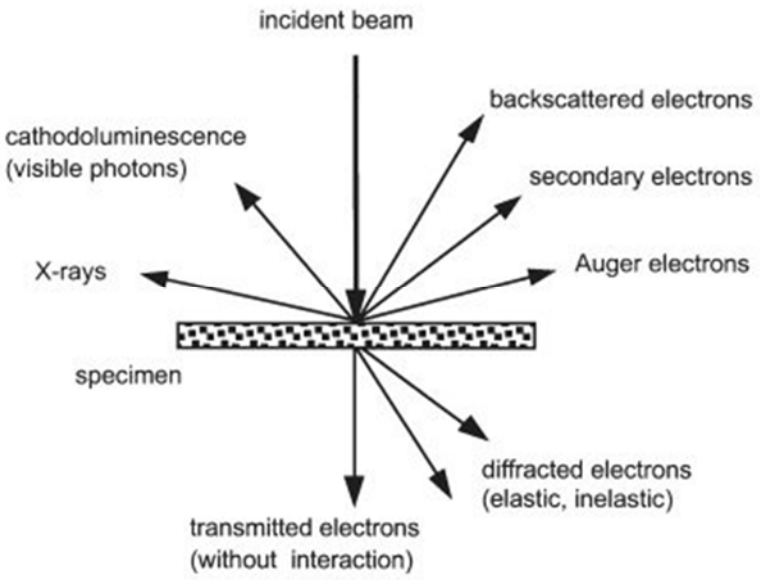

Fig. 2.5: TEM, beam interaction with thin specimen.

2.2.4 Superconducting properties measurements

To measure the magnetic moment of superconducting samples, a superconducting quantum interference device (SQUID) is used. It is a very sensitive magnetometer used to measure extremely delicate magnetic fields. The working principle of this instrument is based on superconducting loops containing Josephson junctions.

Critical Transition Temperature (T_c):

In this work, T_c of bulk MgB_2 was measured using SQUID magnetometer. Magnetic signal or susceptibility of cuboidal specimen of known dimensions was plotted against temperature (M-T curve) at magnetic fields of 10 Oe. Additionally, $T_{c,onset}$ (superconducting onset temperature), T_c^o (superconducting offset temperature)and ΔT_c (superconducting transition width) were also calculated to determine the quality of superconductor synthesized. Usually $\Delta T_c < 1$K is considered an indication of good quality superconducting bulk. Usually onset and offset temperatures are estimated as 5 % and 95 % of the final susceptibility value respectively. However, the first differential of the M-T curve can give these values much easily.

***M-H* curves, Irreversibility Field (H_{irr}) and Upper critical field (H_{c2}):**

Magnetic moment of the specimen measured by SQUID magnetometer during magnetic field sweep between -5 T and +5 T was plotted against ramping field (*M-H* curve) at a constant temperature below T_c, usually 20 K. H_{c2} (the thermodynamic upper critical field) is defined as the field at which magnetic moment reaches zero. In the models describing pinning in conventional superconductors in terms of pinning force density, F_n-h curve ($F=J_cH$, $F_n=F/F_{max}$), magnetic field was normalized to it, $h=H/H_{c2}$. In most of these models, F_n-h curve approached linearly H_{c2} position and it was quite easy to determine H_{c2} value. It, moreover, was not much high. However, in modern superconductors, including MgB_2, H_{c2} value is high, moreover thermally excited magnetic relaxation appears, which reduces the position, where $J_c=0$, from H_{c2} to irreversibility field, H_{irr}. Though lower than H_{c2}, also this quantity is rather high. Thus, with the field limitation of SQUID to 5 T, it is not always possible to find, especially at lower temperatures, the right H_{irr} value. Moreover, the curve approaches H_{irr} exponentially and we need to use a certain precision

criterion. In our case, H_{irr} was estimated as the field value at which J_c reaches 100 A/cm^2 [9]. At temperatures, where H_{irr} was out of the field limit, an extrapolation from reliable data points gave a good approximation. From the *M-H* curve, J_c was calculated using Bean extended critical state model,

$$J_c = 20\ \Delta m/[a^2 d\ (b - a/3)] \tag{2.3}$$

where *a, b* are cross sectional dimensions, $b > a$, and *d* is thickness of the specimen (*a, b, d* in mm) and Δm (in emu units, 1 emu = 10^{-3} Am^2) is the difference in magnetic moments during increasing and decreasing field in the *M-H* loop (see Fig 2.6). In this expression, dimensions of a rectangular superconducting specimen are crucial parameters for determination of critical current density. SQUID specimens with dimensions of approximately 1 x 1 x 0.5 mm^3 were cut from MgB_2 bulk samples [8]. Later, the data will be used to evaluate flux pinning force etc.

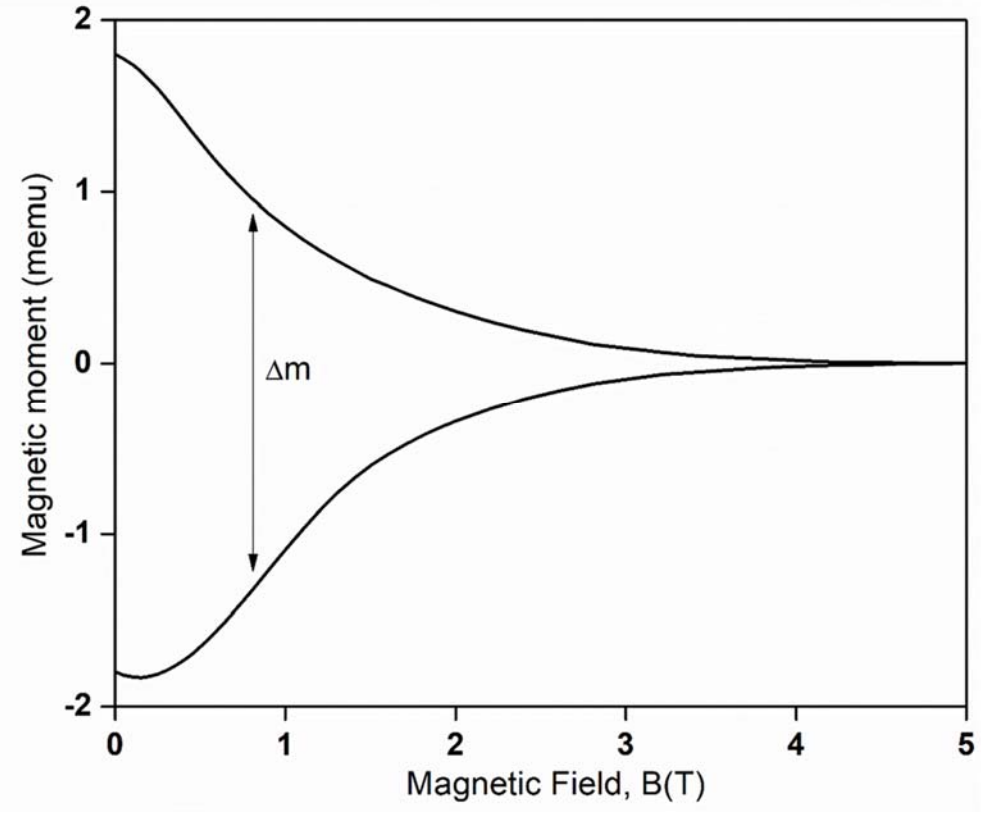

Fig. 2.6: Illustration of a typical M-H curve used for determination of J_c.

2.3 References

[1] Moram, M. A., & Vickers, M. E., *Reports on Progress in Physics,* **2009**, 72(3), 036502.

[2] J. Goldstein, D.E. Newbury, D.C. Joy, C.E. Lyman, P. Echlin, E. Lifshin, L. Sawyer, J.R. Michael, "Scanning Electron Microscopy and X-ray Microanalysis," **2007**, *Springer Science and Business Media, LLC*: New York.

[3] Stadtländer, Christian T. K.-H., "Scanning Electron Microscopy and Transmission Electron Microscopy of Mollicutes: Challenges and Opportunities." **2007**.

[4] Reimer, L., Scanning electron microscopy: physics of image formation and microanalysis. *Springer*, **1998**, 527 p

[5] Reimer, L., Electron Energy-Loss Spectroscopy in the Electron Microscope. *Springer*, **1996**, 490 p.

[6] M. Karlik., *Materials Structure*, **2001**, 8(1):3–16.

[7] Helmut Kohl, Ludwig Reimer, Transmission Electron Microscopy. *Springer Series in Optical Sciences.* doi:10.1007/978-0-387-40093-8, **2008**.

[8] Bean C P, Magnetization of high-field superconductors *Rev. Mod. Phys.,* **1964**, 36 31–9.

[9] Fuchs G, Müller, K.-H, Handstein A, Nenkov K, Narozhnyi V, Eckert D, Schultz L *Solid State Communications,* **1964**, 118(10), 497–501.

Chapter 3

High-Performance Bulk MgB_2 Superconductor Using Amorphous Nano-boron

3.1 Introduction

Since the introduction of MgB_2 into the family of high temperature superconductors i.e. 39 K [1], it has become a potential replacement for many superconducting applications. Extensive research has been carried on its characterization [2] and applications [3]. The superconducting transition temperature of MgB_2 is significantly lower than that of $YBa_2Cu_3O_y$ "Y-123", however, MgB_2 benefits from some BCS -like superconducting features, e.g. a large coherence length and weak magnetic relaxation. The discovery of 39 K superconductivity in MgB_2, which has stimulated considerable interest in it as a family of high temperature superconductors. The transition temperature T_c is higher than previously reported superconducting materials such as Nb_3Ge (T_c-23.2 K) [4] and YPd_2B_2C (T_c-23 K) [5]. This T_c value is highest among A15 intermetallic compounds and intermetallic boro-carbides. This discovery seems to confirm the speculation that the low mass of boron should be responsible for high temperature superconductivity [6]. Unlike YBCO which has to be single crystalline to be well superconducting which in turn reduces the ability of material to scale into devices, MgB_2 overcomes this issue. It is evident that the grain boundaries which act as pinning centers are responsible for the superconductivity of the MgB_2. However, these superconducting properties can be further improved by inserting new pinning centers. Later proton irradiation studies by A.D. Caplin's group proved that creating flux pinning centers via defects or doping in the material

can help in improving the J_c values [7]. This is where many researchers have started doping MgB_2 with different materials to create pinning centers.

Other ways to improve pinning is to increase defects such as grain boundaries etc. by optimizing the sintering conditions and composition [7]. As a result, the transport J_c values at liquid helium temperature and 10 T reached the level of 10^5 A/cm^2 for Si-doped MgB_2 samples [8]. Similar improvements were also observed with additions of carbon [9], boron carbide [10], carbon nanotubes [11], carbohydrates or hydrocarbons [12], graphene oxide [13], Ni-Co-B nanoparticles [14]. However, the critical current density values of MgB_2 materials still need a further improvement for high critical current densities.

From our previous work, it is observed that sintering temperature plays a prominent role in controlling J_c and one can achieve high J_c at an optimum temperature range. In the case of MgB_2, several temperature ranges have been experimented such as <750 ºC, <825 ºC and >850 ºC. From XRD analysis it is observed that single phase MgB_2 is obtained around 775 ºC. Also, high J_c is observed in the samples prepared at 775 ºC sintering temperature, while at other temperatures the J_c is lower. To understand this results SEM analysis has been done, which elucidates that at higher temperatures (> 850 ºC) multiple phases are detected [15]. From the Energy dispersive spectroscopy (EDS) analysis, it is evident that few particles are B-rich in nature by forming new MgB_4 phases. These phases are responsible for the poor J_c values. Apart from the above reasons mentioned, another reason was found to be loss of Mg in vapor form when heated to temperatures above its melting point. Research studies to avoid this loss has been done in ambient temperature and pressure less conditions (by sealing the mixture of magnesium as well as boron in a stainless steel tube and sinter the setup like usual). It is observed that the superconducting properties especially J_c was improved [16]. In other studies, these MgB_4 non-superconducting phases as well as MgO are reported to be helpful in improving the superconducting critical current densities by acting as pinning centers if uniformly distributed in the matrix [17-18]. MgB_2 has been fabricated as crystal, powder, thin films, macroscopic wires, nanowires and tapes using various approaches such as solid state synthesis, mechanical alloying, sol-gel and vapor-transport process [19-22]. MgB_2 offers the possibility of wide engineering applications in the temperature range 20-30 K, where conventional superconductors such as Nb_3Sn and Ni-Ti alloy, cannot play any role due to their low T_c. MgB_2 is superior because of its ability to show superconductivity in sintered form, as it doesn't have any weak link issues.

Considering the group of intermetallic superconductors, the critical temperature of MgB_2 is rather high, which helps to lower the cooling costs. The cheaper technology and the high critical current density (J_c) in the polycrystalline state makes this material promising for several applications such as in power industry, magnetic resonance imaging (MRI), fault current limiters (FCL), and SQUIDS, high energy storage, levitation based devices and powerful super-magnets operating at around 20 K [23]. For superconducting super-magnet applications, it is necessary to produce a good quality and high performance bulk MgB_2 material with high J_c and low production cost. In order to improve the critical current density of the MgB_2 material, various processing techniques have been developed such as chemical doping [8], refining of the initial particle size by ball milling [24], and irradiation [7]. Significant progress has been made concerning the development of processing techniques, flux pinning, critical current density (J_c), large size MgB_2 bulk growth. Many dopants have been studied to obtain high J_c such as Titanium [25], Carbon and its allotropes [26] etc. Recently high J_c is observed in MgB_2 doped with 1.5 wt% carbon-encapsulated boron powder, sintered at 805 °C for 3 hours [27]. The critical current density, J_c of MgB_2 in high magnetic field is correlated with its microstructure. Hence, in this work we tried to manipulate the boron particles size, which in turn controls the final microstructure, thereby resulting in desired superconducting properties such as high critical current density (408 kA/cm^2). We also discuss the pinning mechanism responsible for the high critical current density.

3.2 Experimental

Bulk MgB_2 is synthesized by an *in situ* solid state reaction. The precursors used were commercial powders (Furu-uchi Chemical Corporation) of Mg metal powder (99.9% purity, 200 meshes), nano particle sized amorphous B powder (98.5% purity, ~100 - 300nm). These powders were thoroughly mixed and ground in a glove box in the ratio of 1:2 of Mg:B. This mixture is then pressed into 20mm diameter, 7mm thick pellets using a uniaxial press with a force of approximately 20 kN. These pellets were immediately wrapped by Titanium (Ti) foils and heat treated in a tube furnace in Ar atmosphere. All samples were sintered at an optimized temperature of 775 ºC in a tubular furnace. The sintering soaking time is 3 hours (refer Chapter 2). The temperature is initially increased to 775 ºC and finally decreased to room temperature (RT) at a rate of 100 ºC /h. The constituent phases of the samples were identified with a high-resolution automated X-ray powder diffractometer (RINT2200), using Cu-Kα

radiation generated at 40 kV and 30 mA. The microstructure of these samples was studied with a scanning electron microscope (SEM) and chemical composition was estimated by SEM using EDX analysis.

SQUID specimens with dimensions of approximately 1 x 1 x 0.5 mm^3 were made from MgB_2 bulk samples. Critical temperature (T_c) and Critical current density (J_c) are done using SQUID Magnetometer (Quantum Design, model MPMS5). J_c is calculated from magnetization hysteresis loops (M-H) using extended Bean critical state model formula, as mentioned in chapter 2.

3.3 Results and Discussion

3.3.1 XRD

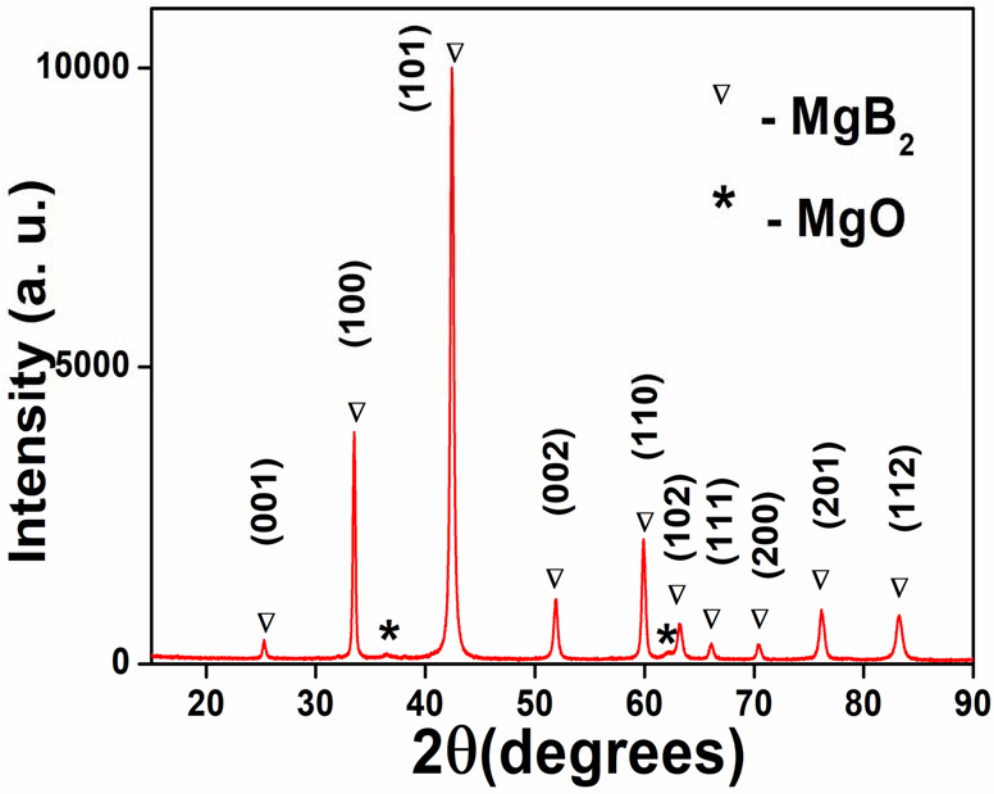

Fig. 3.1: X-ray diffraction pattern for MgB_2. Very small MgO peaks were visible confirming the synthesis of high purity MgB_2 single phase material.

To analyze the microstructure dependence on J_c, we have performed several characterization techniques. The X-ray diffraction pattern (see Fig. 3.1) explain the crystallographic information of the phases in the angular range $15^o \leq 2\theta \leq 90^o$. The crystal structures and constituent phases were investigated using X-ray powder diffractometer. The peak structure indicates almost a single phase with a minimal amount of MgO as an impurity phase in the samples. In addition, previous research studies such as rietveld phase fractions analysis show that the impurity phase MgO is around 7 % in MgB_2 prepared inside glove box, while it is 37 % when prepared in normal atmosphere [28]. As we fabricated the sample in glove box with controlled Ar atmosphere, it can be safely assumed that the MgO percentage is very low. After performing the rietveld phase fraction analysis using MAUD (Material Analysis Using Diffraction), we found that in this sample, the percentage of MgB_2 is 97.97% and MgO is very low such as 2.02 % (see Fig. 3.2) with an error of 0.05%. The MgB_2 and MgO crystallographic information used to analyze the phase fraction are P6/mmm [29], Fm-3m [30] respectively.

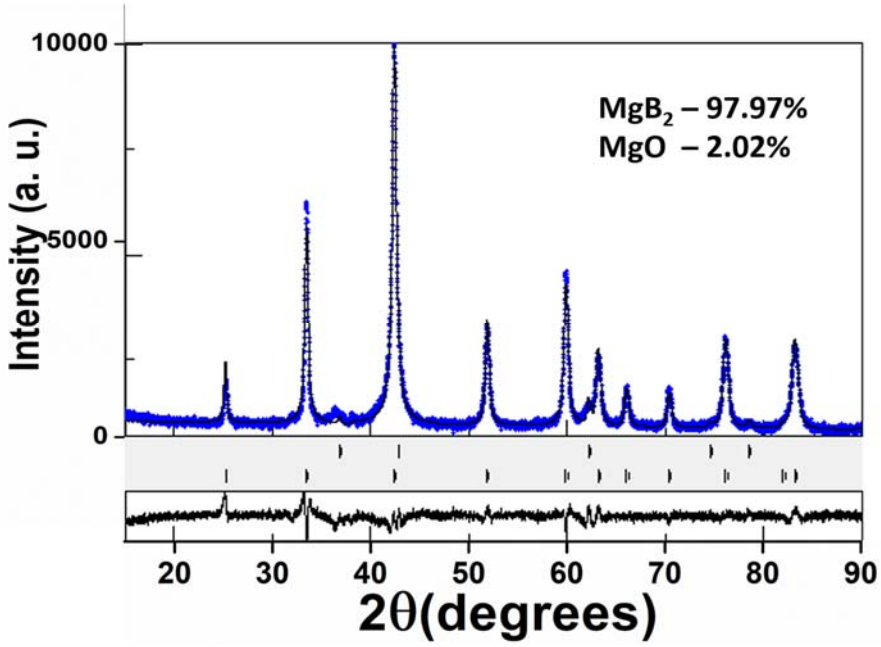

Fig. 3.2: Phase fraction calculation using Rietveld analysis (using MAUD software). Depicts the low concentration of MgO in the matrix.

3.3.2 Morphology

SEM micrograph of the bulk MgB_2 sample shows the grain morphology, porosity and fine size of the powder. SEM analysis at low magnification gives insight on porosity and microstructure of the material. The porosity is very high (see Fig. 3.3).

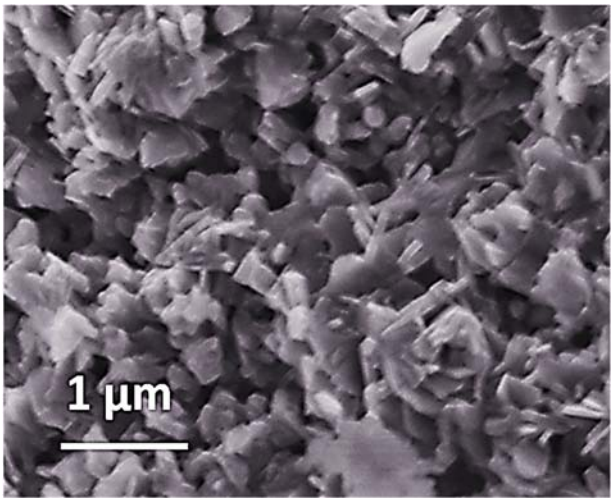

Fig. 3.3: SEM micrographs of MgB_2 at Low magnification depicting the high porosity.

Also, the grains are mostly in round or plate like structure and randomly oriented, which is expected in a solid state sintered MgB_2. Since there is no weak link issue in MgB_2 this grain structure is very less likely to negatively effect the J_c values. However, because of the high porosity, the reduction in amount of MgB_2 for a given dimensions is responsible for lowering J_c. We calculated the density of bulks using, *density = Mass/ Volume* and arrived at a density of approximately 1.27 g/cm^3. Which accounts to half of theoretical density of MgB_2 (2.6 g/cm^3), or also explained as 50% porosity. All of our samples and in general, bulk MgB_2 synthesized by conventional sintering show this behavior. This issue can be addressed with high pressure sintering, which has been of utmost interest since recent years.

Table. 3.1: Atom percentages of elements using EDX analysis. Indicates very minute amount of Oxygen contamination.

Element	Atom % (spot A)	Atom % (spot B)
Mg	40.03	47.9
B	58.31	50.36
O	1.66	1.74

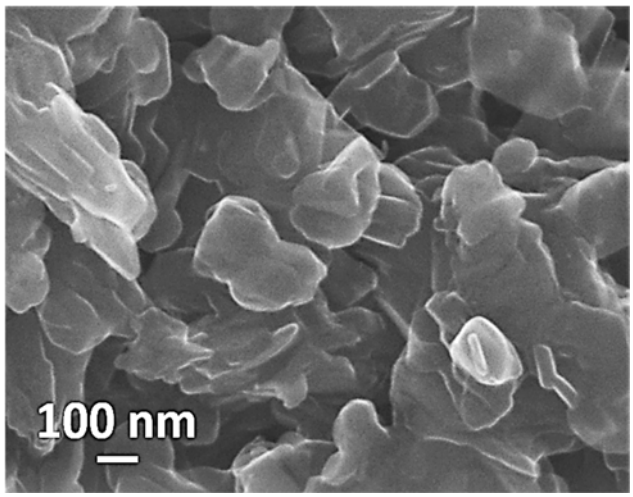

Fig. 3.4: SEM micrograph at higher magnification illustrating the fine grained MgB_2. Grain sizes ranging from 100-500 nm are observed.

On the other hand, lower grain sizes ranging from 100-300 nm can be observed (see Fig. 3.4) which is an important factor for high J_c. Since the grain boundaries are the pinning centers in MgB_2, lower grain size which implies more number of grain boundaries, will aid in enhancing the J_c value. In addition, it can be concluded that there is a sharp superconducting transition (see Fig. 3.5).

3.3.3 Superconducting properties

High onset T_c such as 37.8 K can be observed, with a ΔT of 0.45 K. As expected from the fine microstructure, high J_c is reflected when measured (see Fig. 3.6). J_c as high as 408 $kAcm^{-2}$ is observed at 20 K in self field and 124 $kAcm^{-2}$ at 20 K when the field is 1Tesla. While MgB_2, we produced with

commercial boron powder (~300 Mesh; bigger particles around few micrometers range) has shown a J_c of 270 kAcm^{-2}, which was close to previous reported value, that is around 250 kAcm^{-2} [31]. This critical current density value increment can be attributed to the fine-grained microstructure. Since the sintering temperature is higher than the melting point of Mg, the Boron precursor particle size plays a big role in tuning the final microstructure of MgB_2.

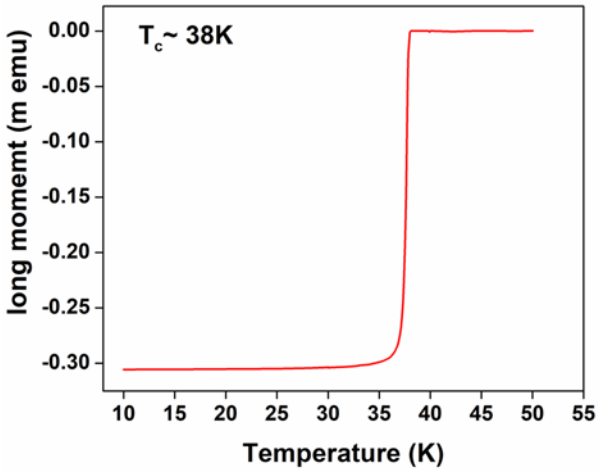

Fig. 3.5: Superconducting transition in the bulk MgB_2 material. Note that a sharp superconducting transition (onset T_c) is observed close to 37.8K.

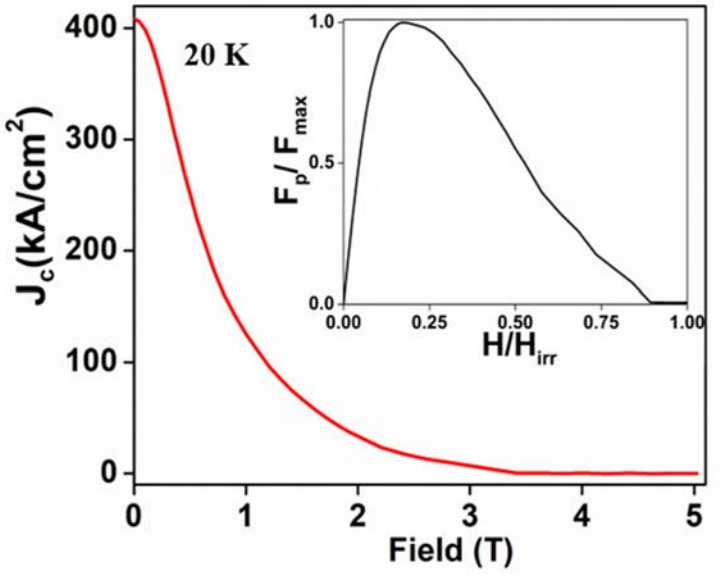

Fig. 3.6: J_c vs B plot – High J_c such as 408 kAcm^{-2} is observed in self field at 20 K and Normalized flux pinning curve vs reduced magnetic field (f_p vs h), where $f_p=F_p/F_{p,max}$ and $h=H_o/H_{irr}$. f_p = 1 at h=0.17 which indicates the grain boundary aided pinning.

In previous studies, it has been reported that the presence of oxide impurities in the matrix are helpful in aiding the pinning effect in the MgB_2 matrix [17]. However, in this case the pinning contribution is primarily due to the grain boundaries and subtly because of the oxide impurities. To justify this mechanism we have studied the material using EDX analysis in FE-SEM. Looking at the atomic percentages (see Table. 3.1), the probability of the oxide impurities seem to be very low. Two different spots are chosen to get a wider view of elemental distribution of Magnesium (Mg), Boron (B), and Oxygen (O). The spots chosen for EDX are labeled as A and B, which can be referred from the figure (see Fig. 3.7). While it can also be seen that the Mg: B ratio is not exactly 1:2, which might be because of the low atomic number of B that makes it difficult to collect the x-rays as the formation of Auger electrons are much favored over the x-rays [32].

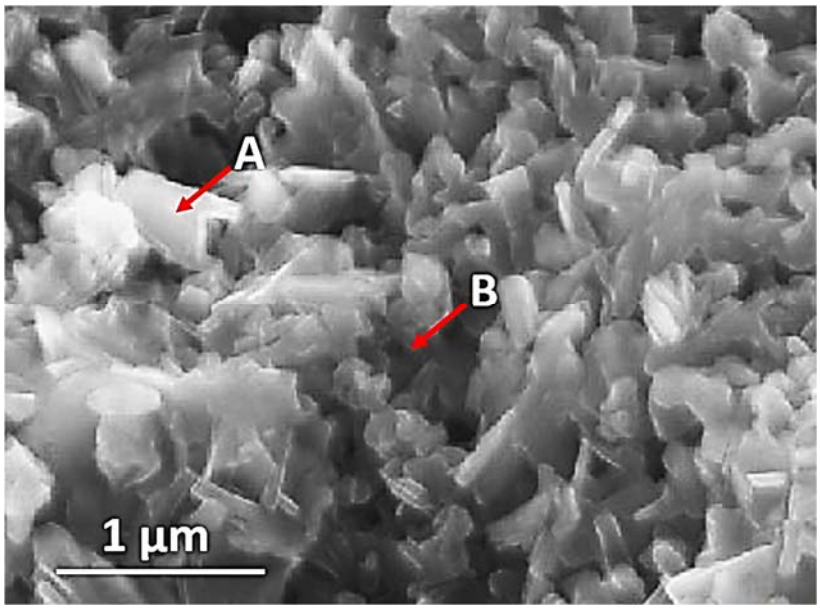

Fig. 3.7: Atomic percentages of elements in the MgB_2 matrix using EDX analysis. Details of two different spots are chosen to get a broad spectrum of elemental distribution of the matrix.

3.3.4 Flux pinning

Using the direct summation of elementary pinning forces, long ago Dew-Hughes proposed the following general expression to evaluate the normalized pinning force density for a material using the following expression: $F_p/F_{pmax} \propto h^p(1-h)^q$, where p and q are dimensionless parameters that

depend on the specific characteristics of flux pinning. From this evaluation, different types of pinning centers as well as mechanisms are described by different values of p and q. In order to understand the flux pinning characteristics in our sample, we have plotted and studied the normalized flux pinning force curve against reduced magnetic field. In this curve $f_p=F_p/F_{p,max}$ is plotted against $h=H_o/H_{irr}$ at 20 K, where H_{irr} is the irreversibility field obtained from M-H loops. The peak position is located at h_{max} = 0.17 (see Fig. 3.6), close to 0.2 which indicates that the dominant mechanism for the pinning is grain boundary pinning. This result is in accordance with previous studies for which normal and surface pinning dominate with in grains [33].

3.4 Conclusion

We have discussed the effect of microstructure on the critical current density of MgB_2. Single phase MgB_2 with fine grain size has been synthesized by a solid state sintering process sintered at 775 ^oC in Ar atmosphere. The XRD indicates that all samples have only a small quantity of MgO phase. SEM analysis showed that the samples have a fine grained structure and are highly porous. Grain size of 100-500 nm are observed which will act as pinning centers and improve J_c. Moderate superconducting transition temperature (T_c), and high critical current density (J_c) such as 408 $kAcm^{-2}$ is observed at 20K and self-field. Analysis of normalized pinning force vs reduced magnetic field curves indicate that the dominant pinning mechanism in this case is grain boundary pinning. This work shows that manipulating the grain size and microstructure is definitely a promising method to enhance the performance of sintered bulk MgB_2 material.

3.5 References

[1] J. Nagamatsu, N. Nakagawa, T. Muranaka, Y. Zenitani, J. Akimitsu, *Nature (London)*, **2001**, vol. 410, no. 63.

[2] Finnemore D. K., and Ostenson J. E., and Bud'ko S. L., Lapertot G., Canfield, P. C, *Phys. Rev. Lett.*, **2001**, vol. 86, no. 11, pp. 2420-2422.

[3] K. Kajikawa, T. Nakamura, *IEEE Transactions on Applied Superconductivity,* **2009**, vol. 19, no. 3, pp.1669 – 1673.

[4] J. R. Gavaler, M. A. Janocko, C. Jones, *J. Appl. Phys*., **1974**, vol. 45.

[5] R. J. Cava, H. Takagi, B. Batlogg, H. W. Zandbergen, J. J. Krajewski, W. P. Peck, Jr., R. B. van Dover, R. J. Felder, T. Siegrist, K. Mizuhashi, J. O. Lee, H. Eisaki, S. A. Carter, S. Uchida, *Nature (London*), **1994**, vol. 367.

[6] S. L. Bud'ko, G. Lapertot, C. Petrovic, C. E. Cunningham, N. Anderson, P. C. Canfield, *Phys. Rev. Lett*., **2001**, Vol. 86 (pp. 1877).

[7] Y. Bugoslavsky, L. F. Cohen, G. K. Perkins, M. Polichetti, T. J. Tate, R. Gwilliam, A. D. Caplin, *Nature*, **2001**, vol. 411, pp. 561–563.

[8] Dou S X, Soltanian S, Horvat, Wang X L, Zhou S H, Ionescu M, Liu H K, Munroe P, Tomsic M, *Appl. Phys. Lett.,* **2002**, vol. 81, pp. 3419-3421.

[9] Mickelson W, Cumings J, Han W Q, Zettl A, *Phys. Rev. B*, **2002**, vol. 65.

[10] P Lezza, C Senatore, R Flükiger, *Superconducting science and Technology*, **2006**, vol 19 (10).

[11] S. X. Dou, W. K. Yeoh, J. Horvat, M. Ionescu, *Applied physics letters*, **2003**, vol. 83 (24).

[12] H Yamada, M Hirakawa, H Kumakura, H Kitaguchi, *Superconducting science and Technology*, **2006**, vol. 19 (2).

[13] Sudesh, Kumar N, Das S, Bernhard, Varma G D, *Supercond. Sci. Technol*., **2013**, vol. 26.

[14] M Mustapić1, J Horvat1, M S Hossain1, Ž Skoko2 and S X Dou, *Superconducting science and Technology*, **2013**, vol. 26 (7).

[15] M. Muralidhar, A. Ishihara, K. Suzuki, Y. Fukumoto, Y. Yamamoto, M. Tomita, *Physica C: Superconductivity*, **2013**, vol. 494, pp. 85-88.

[16] Akiyasu Yamamoto, Jun-ichi Shimoyama, Shinya Ueda, Yukari Katsura, Shigeru Horii and Kohji Kishio, *Superconducting science and Technology*, **2004**, vol. 17 (7).

[17] T. Prikhna, M Eisterer, H W Weber, W Gawalek, V V Kovylaev, M V Karpets, T V Basyuk, V E Moshchil, *Supercond. Sci. Technol*., **2014**, v. 27, No. 4.

[18] T. Prikhna, Michael Eisterer, Wilfried Goldacker, Wolfgang Gawalek et al., *IEEE Transactions on Applied Superconductivity*, **2015**, vol. 25, No. 3.

[19] Narottam P. Bansal, Jon C. Goldsby, Richard B. Rogers, Michael A. Susner, Michael D. Sumption, *Journal of alloys and compounds*, **2015**, vol. 622, pages 986-988

[20] M. Nath B. A. Parkinson, *Advanced Materials*, **2006**, vol. 18 (14), pp.1865-1868.

[21] W Häßler, B Birajdar, W Gruner1, M Herrmann, O Perner, C Rodig, M Schubert, B Holzapfel, O Eibl and L Schultz, *Superconducting science and technology*, **2006**, vol.19 (6).

[22] X.X. Xi, A.V. Pogrebnyakov, S.Y. Xu, K. Chen, Y. Cui, E.C. Maertz, C.G. Zhuang, Qi Li, D.R. Lamborn, J.M. Redwing, Z.K. Liu, A. Soukiassian, D.G. Schlom, X.J. Weng, E.C. Dickey, Y.B. Chen, W. Tian, X.Q. Pan, S.A. Cybart, R.C. Dynes, *Physica C*, **2007**, vol. 456, pp. 22-37.

[23] K Vinod, R G Abhilash Kumar and U Syamaprasad, *Superconductor Science and Technology*, **2007**, vol. 20, no. 1.

[24] Gumbel A G, Eckert J, Fuchs G, Nenkov K, Müller K H, Schultz L, *Appl. Phys. Lett*., **2002**, vol. 80, pp. 2725.

[25] F. Yang, S.Q. Li, G. Yan, J.Q. Feng, X.M. Xiong, S.N. Zhang, Q.Y. Wang, G.Q. liu, Y.C. Pang, H.F. Zou, C.S. Li, Y. Feng, *Journal of Alloys and Compounds*, **2015**, vol. 622, pp. 714-718.

[26] Satrio Herbirowo, Nofrijon Sofyan, Risuliniko Saragih, Agung Imaduddin, Hendrik, Pius Sebleku, Akhmad Herman Yuwono, *AIP Conference Proceedings*, **2017**, 1826, 020007; doi: 10.1063/1.4979223

[27] M. Muralidhar, M. Higuchi, P. Diko, M. Jirsa, M. Murakami, *Journal of Physics: Conf. Series*, **2017**, vol. 871.

[28] Dharmendra Kumar Singh, Brajesh Tiwari, Rajveer Jha, H.Kishan, V.P.S.Awana, *Physica C: Superconductivity and its Applications*, **2014**, vol 505, pp. 104-108.

[29] Jorgensen J.D., Hinks D.G., Short S, Physical Review, *Serie 3. B - Condensed Matter*, **2001**, vol. 63, pp. 2245221-2245225.

[30] Sasaki Satoshi, Fujino Kiyoshi, Takéuchi Yoshio, Proceedings of the Japan Academy, *Series B: Physical and Biological Sciences*, **1979**, vol. 55, pp. 43-48

[31] H Kumakura, Y Takano, H Fujii, K Togano, H Kito, H Ihara, *Physica C: Superconductivity*, **2001**, vol 363, pp 179-183.

[32] J. Berlin, Analysis of boron with energy dispersive x-ray spectrometry, *Imaging Microsc*., **2011**, 13, pp. 19-21.

[33] D.A Cardwell, N Hari Babu, M Kambara, A.M Campbell*, Physica C: Superconductivity*, **2002**, vol 372-376. Part 2, pp. 1262-1265.

Chapter 4

Optimization of carbon-encapsulated boron doping for high-performance bulk sintered MgB_2

4.1 Introduction

Discovery of superconductivity in MgB_2 [1] attracted research focus from trendy superconductors (intermetallic [2], cuprates etc.). The reason was the specific position of this material among other superconductors, being much closer to conventional ones, both by its T_c and other superconducting characteristics. As regards physics, it appeared soon that it is a special type of superconductor, a two/gap system, never seen before. Concerning technology of preparation, the production easiness, light weight, low cost, simple crystal structure, no weak links [3], scalability etc. were extremely attractive issues, too. Hence, MgB_2 offers various magnetic applications [4]. We are now at a point where MgB_2 is being studied thoroughly from 3D to 1D structures looking for innovative and effective ways to improve the superconducting and mechanical properties. In the endeavor to improve critical current density (J_c), the fact is in focus that it mainly depends on the microstructure, which can be manipulated on demand. On the other hand, T_c is an intrinsic material property, not easy to manipulate. T_c in most cases degrades with increasing concentration of secondary additions [5,6]. So far, minute additions of secondary phases in MgB_2 have been rigorously studied for sake of improving J_c by adding various materials such as carbon [7–14], silver, etc. [6,15–21]. These substituents were added to the solid mixture of Mg and B powders, rigorously mixed before sintering. In most cases, the amount of substituents was very little from 0 to 10 wt%, due to the inverse relation of T_c with the amount of additive/dopant content in the matrix. Another problem is uniform distribution in the matrix [22]. Carbon is one such effective substituent, it can replace boron in the MgB_2 matrix, due to a close atomic radius. It results in creation of strain and distortion in the matrix, which in turn can act as a pinning center. Apart from that, these irregularities in the matrix reduce coherence length which

leads to inter-band scattering, causing increment in H_{c2} (upper critical field) [23,24]. So far, carbon was doped into MgB_2 via several carbon sources such as carbohydrates [25], carbon allotropes [26], graphene oxides [27], SiC [28], Coronene [29], toluene [7] etc. A uniform distribution of carbon in the matrix was always a challenge, as the products require stability and reliability over long run. To enable a commercial production, we opted carbon encapsulated boron, where carbon uniformly coats boron. In our previous works, we reported that low concentration of carbon (less than 3 wt%) results in a high critical current density [12]. In opposite, higher concentrations of carbon result in a degradation of critical temperature and formation of undesired Mg-C-B phases [30]. So, we need to perfectly optimize the carbon content to obtain best performance for commercialization. In this work, we tried to vary the carbon wt% from 1 to 1.9 wt% and to tune the product properties.

4.2 Experimental

The carbon-encapsulated boron powder was fabricated in collaboration with PAVEZYUM, Turkey. We produced amorphous boron powder through pyrolysis of Diborane gas (B_2H_6) under inert conditions i.e. the hydrogen gas was flown in the B_2H_6 gas stream throughout the whole synthesis. To elaborate this hydrogen stream (a reducing agent) acts as protection against oxidation. Simultaneously during this pyrolysis technique the thermal conductivity is enhanced. In addition to B_2H_6, a gaseous hydrocarbon (C_xH_y) is mixed in the stream. This way, the hydrocarbon decomposes to form a coating of thin carbon layers around freshly formed circular shaped boron particles. Because of the morphology of powder such as carbon surrounding boron, the final product is named Carbon Encapsulated Boron (CEB). The wt% of carbon is estimated after the fabrication of final product.

To optimize the CEB amount for obtaining the possible highest J_c, a series of bulk MgB_2 was synthesized by *in situ* solid state reaction, with concentrations of CEB such as 1 wt%, 1.1 wt%, 1.35 wt%, 1.5 wt%, and 1.9 wt%. The precursors were commercial powders (Furu-uchi Chemical Corporation) of amorphous Mg powder (99.9% purity, 200 meshes) and carbon encapsulated boron powder. One gram of MgB_2 was synthesized with Mg and CEB components weighing 0.529 g and 0.471 g, respectively, which was molar ratio of 1:2, as required. These powders were rigorously mixed and ground in a glove box to avoid oxide formation. This mixture was then pressed into 20 mm diameter, 7 mm thick pellets using a uniaxial hydraulic press with a force of 20 kN. These pellets were immediately wrapped in Titanium (Ti) foils and heat treated at 775 ^oC for 3 hours in a tube

furnace in Ar atmosphere. The constituent phases in the final samples were identified with a high-resolution automated X-ray powder diffractometer (RINT2200) with a step size of 0.01° from 10° to 90°, using Cu-K_α radiation generated at 40 kV and 30 mA. Rietveld analysis was done to find out the phase fraction of all constituent phases detected from XRD. The microstructure of these samples was later studied with a field-emission scanning electron microscope (FE-SEM). To study the carbon distribution in the matrix, we used energy dispersive X-ray analysis (EDX).

For SQUID measurements, specimens with dimensions of approximately 1.5 x 1.5 x 0.75 mm^3 were cut from MgB_2 bulk samples. Critical temperature (T_c) and critical current density (J_c) were measured using SQUID Magnetometer (Quantum Design, model MPMS5). J_c was calculated from magnetization hysteresis loops (M-H) using the extended Bean critical state model [31].

4.3 Results and Discussion

4.3.1 X-ray Diffraction and Superconducting Performance

XRD results in Fig. 4.1 shows a slight shift of the (110) peak towards higher diffraction angles in proportion with carbon wt%. This tells us that there is carbon substitution in the lattice and the amount of shift is proportional to the amount of carbon substituted [12]. The lattice parameters were calculated by using Bragg's law. The lattice parameter *a* (equivalent to *b*) was calculated by using (110) peak, parallel to *ab*-plane, while *c* was calculated using (002) peak, perpendicular to *ab*-plane. The standard lattice parameters of pure MgB_2 are $a \sim b \sim 3.086$ Å and $c \sim 3.524$ Å. *a* drops with increasing carbon content, up to 1.5 wt%, but above 1.5 wt% it starts to increase. This is because when carbon atoms substitute boron in the lattice, the lattice parameter shrinks as the carbon atoms have a lower atomic radius compared to boron. The amount of decrease in the lattice parameter is thus proportional to amount of carbon substitution. *c* stays unchanged, as there is no shift in (002) peak. All the changes happen in *ab*-plane, there is no shift in (00l) diffraction peaks. This is due to hexagonal arrangement of Mg and B layers in the MgB_2 lattice. More detailed information can be found in Table. 4.1. Fig. 4.2 depicts sharp transition, which indicates high quality of the MgB_2 bulks.

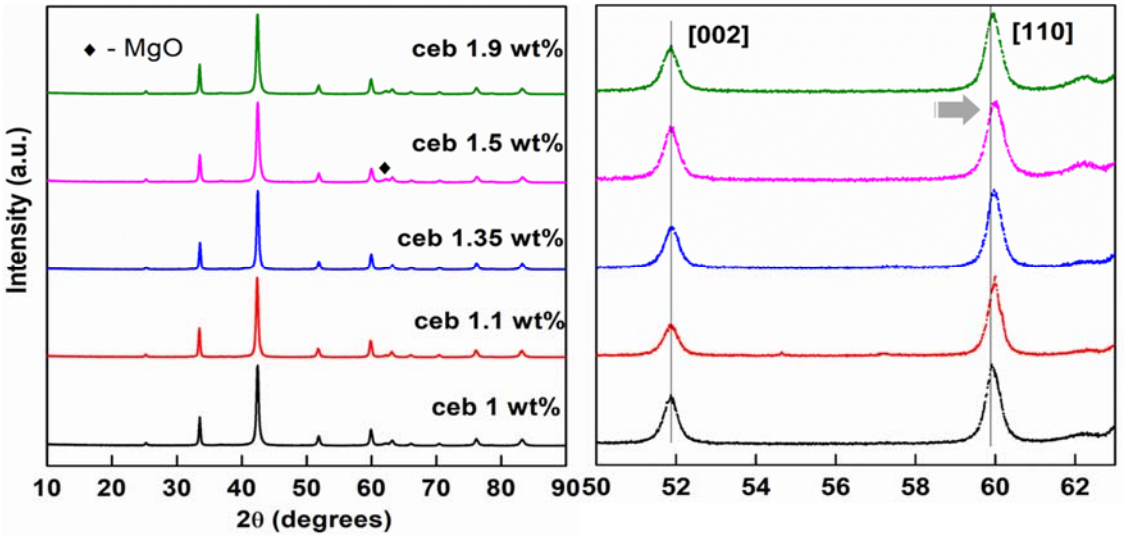

Fig. 4.1: XRD of MgB_2 with several wt% CEB based bulks. Shift in [110] peaks can be observed, while [002] peaks remain un-changed.

Table. 4.1: Lattice parameters and crystallite size calculations from XRD data. Large reduction and smallest crystallite size are observed in cc 1.5 wt% based MgB_2 bulk.

CEB wt %	Lattice parameter *a* (Å)	Lattice parameter *c* (Å)	Crystallite size (nm)
0	3.086	3.524	~ 27
1	3.0854	3.524	21
1.1	3.0849	3.524	21.3
1.35	3.0826	3.524	21.3
1.5	3.0798	3.524	17.1
1.9	3.0830	3.524	19.8

There are also other ways to estimate the carbon doping into the bulk. One way to estimate the actual amount of carbon substitution x in $Mg(B_{1-x}C_x)_2$, was calculating x using the formula, $x = 7.5 \times \Delta(c/a)$, where $\Delta(c/a)$ is the change in c/a compared to an undoped reference sample [32]. The actual carbon contents for the bulks made of CEB 1, 1.1, 1.35, 1.5 and 1.9 wt%, in terms of $2x$ are estimated to be 0.004, 0.0066, 0.02, 0.036 and 0.018 respectively. These results are comparable with those calculated when large wt% CEB was used [33]. Although these values are minute, the amount of carbon substitution was maintaining the trend with T_c and J_c results reported in later discussions.

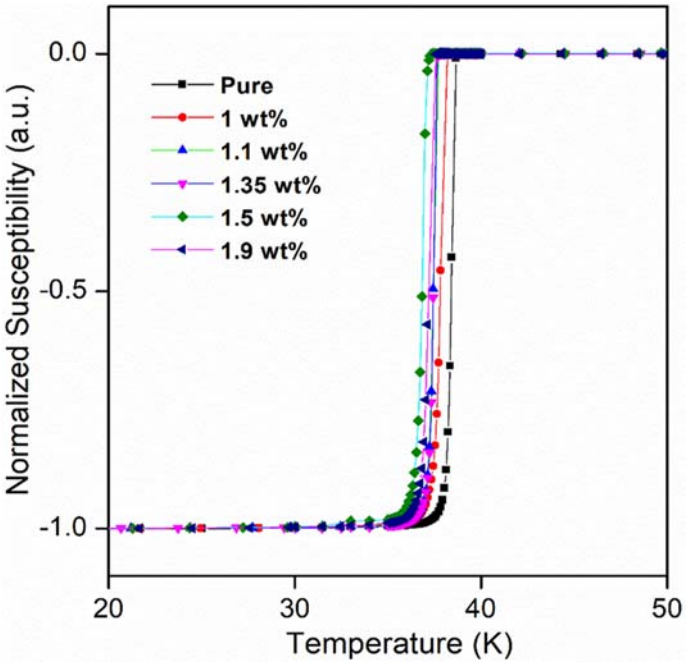

Fig. 4.2: Normalized susceptibility plotted against temperature. All samples show $\Delta T_c < 1$ K, which shows that the synthesized bulks are of high quality.

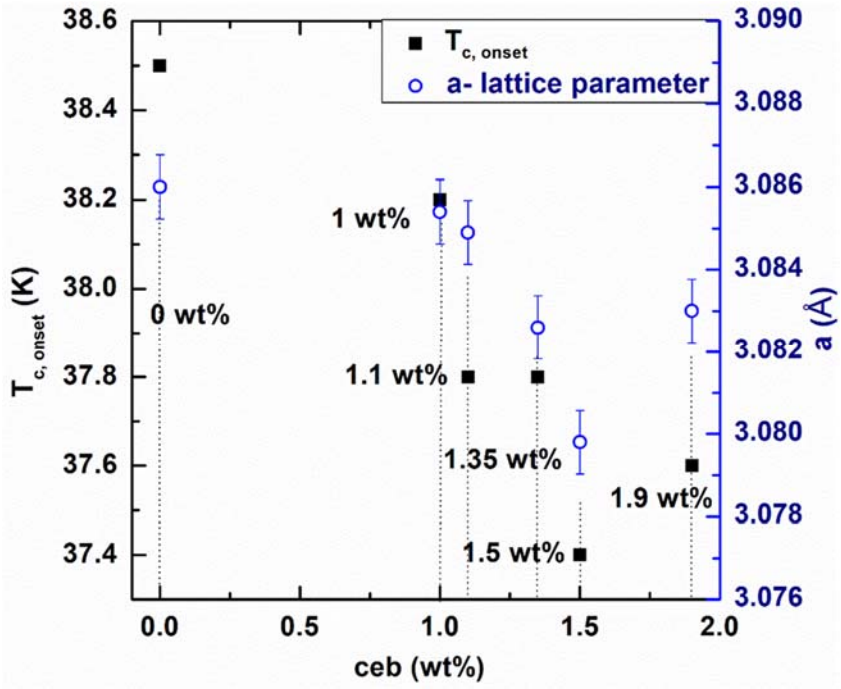

Fig. 4.3: $T_{c,onset}$ (on the left Y-axis in black) and lattice parameter a (on the right Y-axis in blue) plotted against CEB wt%. Both the parameters follow the same trend.

The onset superconducting temperature results (Fig. 4.3) support the conclusions made from the XRD analysis. T_c starts to decrease with increasing CEB wt% till 1.5wt% and starts to raise thereafter. T_c reduction with increasing C doping is well known from previous studies. The main reasons are carbon substitution into the lattice and the associated lattice strain. This phenomenon is observed in almost every case of dopants [5,24,27,34]. From these results we can conclude that maximum carbon doping is for 1.5 wt% CEB.

The critical current density displayed as a function of the applied magnetic field in the semi-logarithmic plot exhibited superior H_{irr} values (Fig. 4.4). All the bulks exhibited superior properties when compared to the regular bulk. Especially, the bulk with 1.5 wt% CEB exhibited the highest value among all other bulks, 435 kA/cm^2 at self-field, 20 K (inset Fig. 4). At low fields close to self-field as well as high fields (2-4 T), J_c of the 1.5 wt% CEB based bulk was high. These values are higher than in MgB_2 doped by carbohydrates [35]. Moreover, the tradeoff between T_c reduction and J_c improvement was not as good as in the present case. This behavior can be explained from the diffraction data obtained from XRD. We calculated the crystallite sizes for all the bulks using Scherrer's equation

$$\tau = K\lambda/\beta \cos\theta \tag{4.1}$$

Here, τ is crystallite size, K is dimensionless shape factor (~0.9), λ is X-ray wavelength (Cu-K$_\alpha$ ~ 1.54 Å), β is FWHM (highest intensity peak – (101) peak), and θ is the Bragg angle. Usually, Scherrer's formula can be used only on grains smaller than micron. In our case, we knew from our previous work that crystallite size of sintered MgB_2 lies around 27 nm and hence the formula can be used without any restrictions.

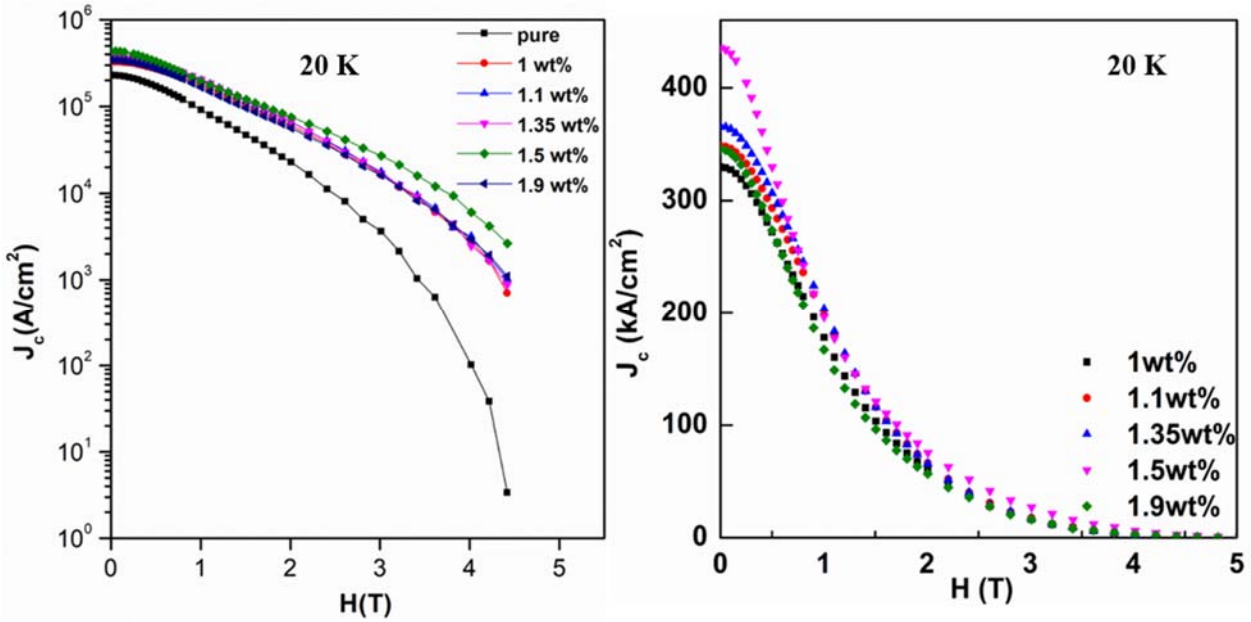

Fig. 4.4: Superconducting critical current density of various CEB wt% based MgB_2 bulks. 1.5 wt% CEB MgB_2 bulk shows the best performance.

In Table. 4.1, we can find the lowest crystallite size ~ 17 nm in MgB_2 with1.5 wt% CEB, which resulted in a high self-field J_c, as grain boundary pinning is prominent at low fields. Fig. 4.5 plots the relation between crystallite size and J_c of bulks. An inverse linear proportionality can be observed, which justifies the grain boundary pinning. A lower crystallite size implies finer grains and therefore a higher number of grain boundaries that are primary pinning centers in MgB_2 bulk superconducting system. In high fields, high J_c is observed because of high defect density created by high carbon substitution into the lattice, as seen on lattice parameters. In addition, the lattice distortion created by maximum doping results in a high impurity scattering, which aids an additional pinning. This indicates that 1.5 wt% CEB is the optimal amount for maximum substitution of carbon into lattice and most effective in improving the critical current density. Any further excess of carbon content is for the performance detrimental [12]. This bulk subjected to much lower temperatures, exhibited extremely large critical current densities such as 660 kA/cm^2 at self-field and 10 K, 550 kA/cm^2 at self-field and 15 K, and 100 kA/cm^2 at 3 T and 10 K (see Fig. 4.6).

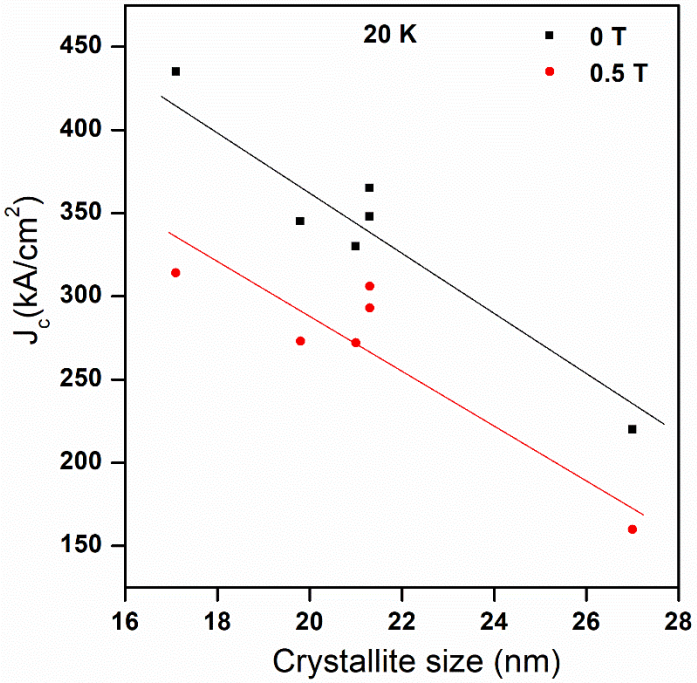

Fig. 4.5: Superconducting critical current density-J_c vs Crystallite size of various CEB based MgB_2 bulks. Plot shows an inverse proportionality.

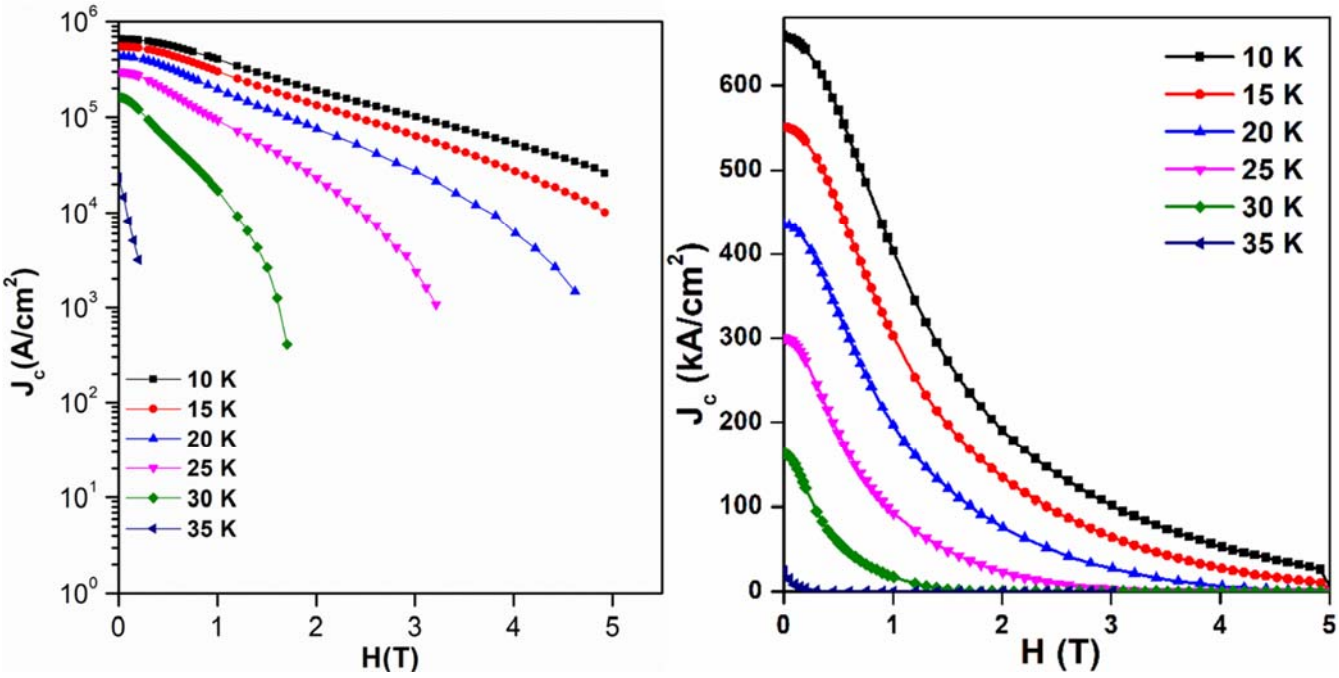

Fig. 4.6: Superconducting critical current density of CEB 1.5 wt% based MgB_2 bulk at various temperatures. At 10 K, the J_c reached 660 kA/cm^2.

In addition, the irreversibility field measured at 10 K was extremely high, up to 20 T (extrapolation), which is very interesting for upcoming high-field applications such as particle accelerators [36], Axion dark matter experiments [37], and magnetic confinement fusion reactors [38] etc. The present irreversibility field values are far above those of conventional Nb_3Sn superconducting magnets. Some studies of MgB_2 report H_{c2} at 4.2 K close to 42 T in thin films, and 44 T (theoretically) at 0 K [39]. Here we note that relaxation in MgB_2 is very weak and therefore H_{irr} can be expected very close to H_{c2}. H_{c2} perpendicular to ab-plane for various thin films ranged at 10 K from 7 to 17 T. This shows that the present extrapolated H_{c2} value for 1.5 wt% CEB exceeds or is almost equivalent to that of thin films, which is an extraordinary result. Similar speculations were made, when 10 wt% double walled carbon nano-tubes were used to dope MgB_2 bulk [26], where the authors predicted up to 42 T at 4.2 K. Elsewhere [35], carbon doping via addition of 10 - 20 wt% of malic acid, resulted in enhancement of superconducting properties. However, J_c was not as good as our present results. Moreover, the H_{c2} at 20 K of MgB_2 bulk with 1.5 wt% CEB around 8 T (obtained via extrapolation) is also higher than that of malic acid doped MgB_2 [33]. Hence, we can conclude that the present results represent a significant milestone in improving superconducting performance of bulk MgB_2, even among several other techniques of carbon doping.

Further, we constructed flux a pinning diagram based on Dew-Hughes general expression, which is a plot of the normalized flux pinning force $(f_p=F_p/F_{p,max})$ against reduced magnetic field $(h=H_o/H_{irr})$. Here, H_{irr} is the irreversibility field and F_p is flux pinning force calculated as a product of magnetic field induction and critical current density. When compared to the reference un-doped MgB_2 bulk, the $f_p(h)$ peak of the MgB_2 bulk with 1.5 wt% CEB is slightly shifted towards higher fields, which indicates a slight pinning contribution from carbon substitution (Fig. 4.7). In addition, we can also observe an increase in FWHM of the peak, which implies an improvement in both low field and high field pinning force. Thus, the decrease in crystallite size contributed to pinning improvement at low fields, while carbon substitution aided in improving high field pinning. Similar scenarios were seen when carbohydrates were doped in bulk MgB_2 system. There also the basis hypothesis is carbon substitution [35]. We tried to calculate parameters (p and q) pertaining to Dew-Hughes expression (3), via curve fitting to get deeper understanding on flux pinning mechanisms. A is a numerical

parameter, while p and q are power-law describing parameters which explain the actual pinning mechanism.

$$f_p = A(h)^p(1-h)^q \qquad 4.2$$

We obtained $p = 0.5 \pm 0.05$, $q = 2 \pm 0.15$, and $A \sim 3.5 \pm 0.4$. The fit curve is plotted as blue line in Fig.4. 6, labelled as Curve fit. According to the Dew-Hughes, the maximum position (h_{max}) can be estimated by the value $p/(p+q)$, which is equivalent to 0.2 from the curve fit parameters. These parameters strongly indicate that the primary pinning mechanism is grain boundary pinning, which is expected in bulk MgB_2 system. In addition, the FWHM of pure as well as ccb based MgB_2 is slender/smaller than theoretical one, because of the anisotropy in the system. The theoretical model was prepared assuming an isotropic material, while MgB_2 is anisotropic [40].

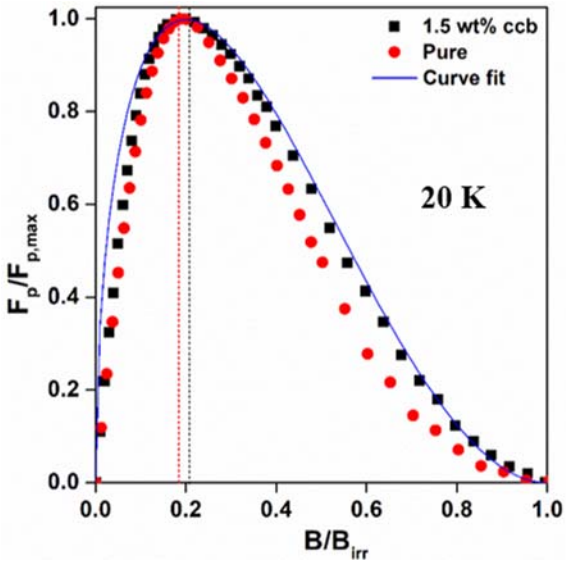

Fig. 4.7: Flux pinning diagrams of the 1.5 wt% CEB based MgB_2 bulk and a reference normal MgB_2 bulk. The 1.5 wt% CEB MgB_2 bulk shows slight increase in peak position as well as the curve width.

To get deeper insight we also calculated flux pinning diagrams of the best sample at various temperatures (ref: Fig. 4.8), the peak positions lie around 0.2. However, if closely observed, the curve shifts towards right/ higher values with increase in temperature. This is because of decrease in the

magnetic anisotropy with increase in temperature, similar results were observed in spark plasma sintered (SPS) MgB_2 [41,42].

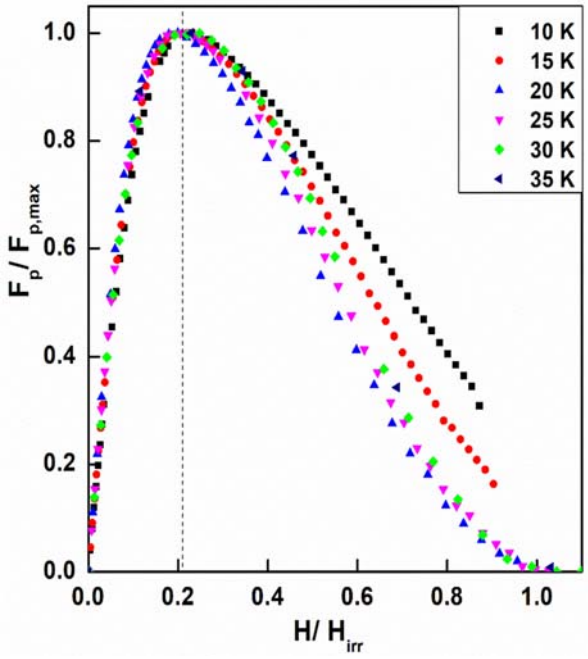

Fig. 4.8: Flux pinning diagrams of the 1.5 wt% CEB based MgB_2 bulk at various temperatures. The normalized flux pinning force at high field increases with reduction in operating temperature but the peak position doesn't shift.

4.3.2 Microstructural and Density Studies

We calculated the density of bulks using, *density = Mass/ Volume of cylindrical pellet* and arrived at a density of approximately 1.12 - 1.22 g/cm^3 for all the bulks. Which accounts to almost half of theoretical density of MgB_2 (2.6 g/cm^3), or also explained as 50% porosity. This porosity is mainly due to the voids left by reacted Mg. All of our samples and in general, bulk MgB_2 synthesized by conventional sintering show this behavior. To purport the superconducting performance results, we performed SEM and EDX (ref: Fig. 4.9). EDX spectrum reveals that the carbon distribution is uniform throughout the matrix, which is what we envisioned.

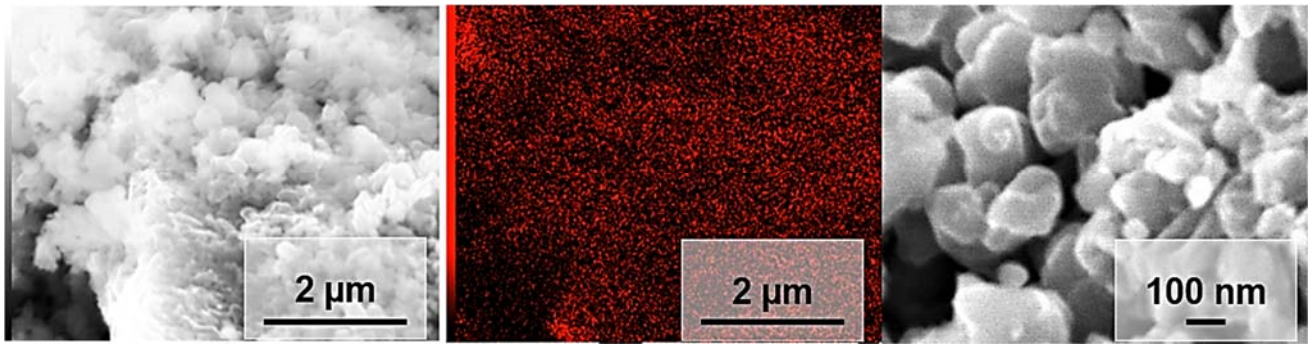

Fig. 4.9: Microstructural analysis (left most) and carbon distribution (center) of 1.5 wt% ccb based MgB_2 bulk. High magnification image (right most) illustrates the nanometer-sized particles.

While the high magnification images depict fine particles of size range around 50-200 nm. These results purport the crystallite size refinement as well as impurity scattering through the matrix. Hence this technique aids in synthesizing stable high performance bulk MgB_2 and therefore more reliable for use in commercial applications.

4.4 Conclusion

By optimizing carbon content in CEB, we succeeded to prepare a high performance sintered bulk MgB_2. 1.5 wt% of carbon in CEB was found to result in the best performance with a tremendous J_c of 660 kA/cm^2 at 10 K, self-field. H_{c2} (calculated by extrapolation) was also substantially improved, being almost equivalent to the best records reported so far. XRD results explain the maximum carbon substitution in 1.5 wt% CEB based bulk, via (110) peak shift, reflecting a change in the crystallite size calculated using Scherrer's equation. *M-T* loops showed that the reduction in $T_{c,onset}$ was proportional to the carbon substituted into the lattice. In addition, ΔT_c <1 K for all bulks proved high quality. Flux pinning diagrams revealed that, while the dominant pinning came from grain boundaries, there was a considerable effect from increased electron impurity scattering caused by carbon substitution. This resulted in an increase of H_{c2}, high field J_c, as well as the curve width of flux pinning diagrams. Microstructural analysis revealed small MgB_2 particles and uniform carbon distribution that supported all our assumptions. In summary, the 1.5 wt% carbon concentration in CEB was found to be beneficial for fabricating high performance MgB_2 bulks, suitable for a wide range of applications.

4.5 References

[1] J N, N N, T M, Y Z and J A *Nature* **2001** 410 63

[2] Matthias B T, Geballe T H, Geller S and Corenzwit E *Phys. Rev.* **1954** 95 1435

[3] Larbalestier D C et.al., *Nature* **2001** 410 186–9

[4] Glowacki B A, Majoros M, Eisterer M, Toenies S, Weber H W, Fukutomi M, Komori K and Togano K MgB_2 *Phys. C Supercond. its Appl.* **2003** 387 153–61

[5] Ansari I A, Shahabuddin M, Ziq K A, Salem A F, Awana V P S, Husain M and Kishan H *Supercond. Sci. Technol.* **2007** 20 827–31

[6] Kirat G, Kizilaslan O, Aksan M A and Yakinci M E *Phys. B Condens. Matter* **2014** 445 24–7

[7] Bohnenstiehl S D, Susner M A, Yang Y, Collings E W, Sumption M D, Rindfleisch M A and Boone R *Phys. C Supercond. its Appl.* **2011** 471 108–11

[8] De Silva K S B, Gambhir S, Wang X L, Xu X, Li W X, Officer D L, Wexler D, Wallace G G and Dou S X *J. Mater. Chem.* **2012** 22, 13941-13946.

[9] Dou S X, Shcherbakova O, Yoeh W K, Kim J H, Soltanian S, Wang X L, Senatore C, Flukiger R, Dhalle M, Husnjak O and Babic E *Phys. Rev. Lett.* **2007** 98 2–5.

[10] Hossain M S A, Senatore C, Flükiger R, Rindfleisch M A, Tomsic M J, Kim J H and Dou S X *Supercond. Sci. Technol.* **2009** 22

[11] Higuchi M, Muralidhar M, P D, M J and Murakami M *Journal of Physics: Conference Series* p 871

[12] Muralidhar M, Higuchi M, Jirsa M, Diko P, Kokal I and Murakami M **2017** *IEEE Trans. Appl. Supercond.* **2017** 27 18–21

[13] Muralidhar M, Nozaki K, Kobayashi H, Zeng X L, Koblischka-Veneva A, Koblischka M R, Inoue K and Murakami M *J. Alloys Compd.* **2015** 649 833–42

[14] Bhagurkar A G, Yamamoto A, Anguilano L, Dennis A R, Durrell J H, Hari Babu N and Cardwell D A *Supercond. Sci. Technol.* **2016** 29

[15] Kumar D, Muralidhar M, Rao M S R and Murakami M *J. Supercond. Nov. Magn.* **2018** 31 2033–8

[16] Muralidhar M, Inoue K, Koblischka M R, Murakami A and Murakami M *J. Adv. Eng. Mater.* **2015** 17 831–8

[17] Ma Z, Liu Y, Han Y, Zhao Q, Gao Z, Ma Z, Liu Y, Han Y, Zhao Q and Gao Z *J. Appl.*

Phys. **2008** 104 0–5

[18] Cheng F, Ma Z, Liu C, Li H, Shahriar A. Hossain M, Bando Y, Yamauchi Y, Fatehmulla A, Farooq W A and Liu Y *J. Alloys Compd.* **2017**727 1105–9

[19] Arvapalli S S, Miryala M and Murakami M *Adv. Eng. Mater.* **2019** 21

[20] Arvapalli S S, Miryala M and Murakami M *IEEE Trans. Appl. Supercond.* **2019** 29 1–4

[21] Ansari I A *Ceram. Int.* **2019** 45 1523–7

[22] Dou S X, Flukiger R, Shcherbakova O, Senatore C, Lezza P, Lortz R and Yeoh W K *IEEE Trans. Appl. Supercond.* **2007** 17 2941–4

[23] Gurevich A *Phys. Rev. B - Condens. Matter Mater. Phys.* **2003** 67 1–13

[24] Ravindran P, Vajeeston P, Vidya R, Kjekshus A and Fjellvåg H *Phys. Rev. B* **2001** 64 224509.

[25] Kim J H, Zhou S, Hossain M S A, Pan A V. and Dou S X *Appl. Phys. Lett.* **2006** 89, 3–6.

[26] Serquis A, Serrano G, Moreno S M, Civale L, Maiorov B, Balakirev F and Jaime M *Supercond. Sci. Technol.* **2007** 20.

[27] Sudesh, Kumar N, Das S, Bernhard C and Varma G D *Supercond. Sci. Technol.* **2013** 26, 095008

[28] Dou S X, Soltanian S, Horvat J, Wang X L, Zhou S H, Ionescu M, Liu H K, Munroe P and Tomsic M *Appl. Phys. Lett.* **2002** 81 3419–21.

[29] Ye S J, Matsumoto A, Zhang Y C and Kumakura H *Supercond. Sci. Technol.* **2014** 27.

[30] Wilke R H T, Bud'ko S L, Canfield P C, Finnemore D K, Suplinskas R J and Hannahs S T *Phys. Rev. Lett.* **2004** 92 2–5.

[31] Bean C P *Rev. Mod. Phys.* **1964** 36 31–9.

[32] Avdeev, M., Jorgensen, J. D., Ribeiro, R. A., Bud'ko, S. L., & Canfield, P. C. *Physica C: Superconductivity*, **2003** 387(3-4), 301–306.

[33] Barua, S., Hossain, M. S. A., Ma, Z., Patel, D., Mustapic, M., Somer, M., … Dou, S. X. *Scripta Materialia*, **2015** 104, 37–40.

[34] Vajpayee A, Jha R, Srivastava A K, Kishan H, Tropeano M, Ferdeghini C and Awana V P S *Supercond. Sci. Technol.* **2011** 24.

[35] Kim J H, Zhou S, Hossain M S A, Pan A V. and Dou S X *Appl. Phys. Lett.* **2006** 89.

[36] Rossi L and Bottura L 2013 *Rev. Accel. Sci. Technol. Vol. 5 Appl. Supercond. Technol. to Accel.* **2012** 683 51–90.

[37] Asztalos S J, Carosi G, Hagmann C, Kinion D, Van Bibber K, Hotz M, Rosenberg L J, Rybka G, Hoskins J, Hwang J, Sikivie P, Tanner D B, Bradley R and Clarke J *Phys. Rev. Lett.* **2010** 104, 1–4.

[38] Ongena J, Koch R, Wolf R and Zohm H *Nat. Phys.* **2016** 12 398–410

[39] Braccini V, Gurevich A, Giencke J E, Jewell M C, Eom C B, Larbalestier D C, Pogrebnyakov A, Cui Y, Liu B T, Hu Y F, Redwing J M, Li Q, Xi X X, Singh R K, Gandikota R, Kim J, Wilkens B, Newman N, Rowell J, Moeckly B, Ferrando V, Tarantini C, Marré D, Putti M, Ferdeghini C, Vaglio R and Haanappel E *Phys. Rev. B - Condens. Matter Mater. Phys.* **2005** 71 24–7

[40] Eisterer M *Supercond. Sci. Technol.* **2007** 20 47–73

[41] Jirsa M, Rames M, Koblischka M R, Koblischka-Veneva A, Berger K and Douine B *Supercond. Sci. Technol.* **2015** 29

[42] Jirsa M, Koblischka M R, Higuchi T, Muralidhar M and Murakami M *Phys. C Supercond. its Appl.* **2000** 338 235–45

Chapter 5

Beneficial Impact of Excess Mg on Flux Pinning in Bulk MgB_2 Synthesized with Ag Addition and Carbon Encapsulated Boron.

5.1 Introduction

Despite the emerging high temperature superconducting (HTS) materials (T_c > 77K) till recent times, Magnesium diboride (T_c ~ 39K) caught immediate attention of many researchers since its discovery by Jun akimitsu group in 2001[1]. For example, the superconducting transition temperature of MgB_2 is significantly lower than that of $YBa_2Cu_3O_y$ "Y-123", however, MgB_2 benefits from some BCS-like superconducting features, e.g. a large coherence length and weak magnetic relaxation. Apart from that, the other vital reasons for MgB_2 being one of the trending bulk superconductors because of its attractive physical properties such as simple hexagonal crystal, light weight as the elements Mg and B are low atomic numbered, low coherence length, no weak link issue [2] and finally the most important advantage which is easy synthesis (solid state sintering). Hence mainly focused on working towards high trapped field applications at 20K. Extensive research has been carried on its characterization[3] and applications[4] as MgB_2 can be fabricated in many forms as crystals, powder, thin films, macroscopic wires, nanowires and tapes. These multiple forms and various intricate shaped bulks can be fabricated but not only solid state sintering but also various approaches such as mechanical alloying, sol-gel and vapor-transport process[5]. MgB_2 offers the possibility of wide-ranging engineering applications[6] in a temperature range of 20-30 K, where traditional superconductors such as Nb_3Sn [7] and Nb-Ti alloys, cannot play any role due to their low T_c (~ 10 K, operating temperatures are around 4.5 K). MgB_2 is superior because of its ability to exhibit superconductivity in sintered form unlike most of the HTS materials, as it doesn't have any weak link issues. The main feature of this material is

that its superconducting properties will not be deterred because of its grain boundaries; in contrary, these hindrances act as pinning centers there by enhancing the superconducting critical current density (J_c). This is mainly due to its peculiar inherent feature of the material of not being negatively effected by weak links caused by grain boundaries as mentioned earlier. Comparing the group of present intermetallic superconductors, the critical temperature of MgB_2 is rather high, which helps to lower the cooling costs. Because of the above mentioned advantages, MgB_2 is a promising material for several applications such as in power industry (superconducting wires etc.), magnetic resonance imaging (MRI), fault current limiters (FCL), SQUID devices, high energy storage, levitation based devices and powerful super-magnets operating at around 20 K [6]. When aiming at superconducting super-magnet applications, it is necessary to produce a good quality and high performance bulk MgB_2 material with high J_c and low production cost. For improving superconducting properties such as the trapped field of the superconducting material, one has to improve the critical current density as well as the volume parameter as the trapped field is proportional to J_c and volume. In case of MgB_2 bulk, as the synthesis technique is simple sintering, the volume parameter can be manipulated at will and hence improving J_c is the key for improving trapped field properties. In order to improve the critical current density of the MgB_2 material, various techniques have been employed such as chemical doping[8], ball milling[9], spark plasma sintering[10] use of nano-sized precursor powders[11] and irradiation[12]. These techniques are responsible for increasing flux pinning centers such as grain boundaries, defects, dislocations etc. So far, significant progress has been made concerning the development of processing techniques, flux pinning, critical current density (J_c), large size MgB_2 bulk growth. So far many dopants have been studied to obtain high J_c such as Titanium[13], SiC[8], Carbon and its allotropes etc. Among these substitutions, carbon is found much effective as it enters lattice, substituting boron. Although the J_c improves, this disorder (carbon substitution) causes reduction in critical temperature. Lately Ag addition has become popular as it has no impact on T_c while improving the J_c, especially in YBCO system[14][15]. Hence, similar studies have been performed on MgB_2 to check if the same effect can be observed[16]. Elsewhere, it is also reported that Gibbs energy of the Ag-Mg phase formation is negative which tells us the definite formation of Ag-Mg phase. It is also clear that above 1200 ^oC Gibbs energy of MgB_2 formation is inferior to that of Ag-Mg formation [17]. This implies that little amount of Mg is consumed by the Ag during the sintering. Now that slight

amount of Mg is consumed, the stoichiometric ratio of precursors Mg: B is disturbed, Mg being deficient.

In previous investigations where we, it is found that Ag-Mg based intermetallic secondary phases are formed and are acting as flux pinning centers. In this work, we tried to optimize the excess Mg required to be added in order to balance the loss when Ag is added and result in optimum Ag-Mg phases formation along with high superconducting performance. Changes in superconducting properties with excess Mg addition are also discussed.

5.2 Experimental procedure

To study the optimum amount of excess Mg precursor required for balancing the loss from Ag-Mg phases formation or obtaining best J_c, a series of bulk MgB_2 is synthesized by an *in situ* solid state reaction. Several amounts of Mg had been varied such as x = 1.05, 1.075, 1.1, 1.125, 1.15 in Mg_xB_2. The precursors used were commercial powders (Furu-uchi Chemical Corporation) of amorphous Mg powder (99.9% purity, 200 meshes), carbon encapsulated Boron powder (1.5% carbon) and 4 wt% Ag. In general, to make 1 gram of MgB_2 without Ag we use 0.529g of Mg powder and 0.471g of CCB (1.5% carbon) powder, which is 1: 2 molar ratio of Mg: B. The mixture is further processed into bulk as mentioned in chapter 2. Later, the sintered bulk pellets were characterized using XRD, FE-SEM, EDAX, and SQUID similar to that of in previous chapters.

The spatial trapped field distribution at 20 K was mapped 20 minutes after cooling the sample at the same temperature 10 mm away from a 45 mm diameter permanent magnet using a cryogen-free cryo-cooler. During these measurements, the temperature was monitored with two sensors. One was located on the cold head of the cryo-cooler and the other on the sample surface. The Hall probe used for mapping the field was located above the cryostat 10 mm away from the superconductor. Levitation force measurements were also carried out at 20 K after cooling down the samples at 35 mm from the permanent magnet.

5.3 Results and Discussion

5.3.1 XRD analysis

The X-ray diffractograms (XRD) (see Fig. 5.1) of the Mg excess samples (best sample and highest Mg excess doped) are compared with pure sample. Formation of Ag-Mg phases along with small

amounts of MgO, while MgB_2 being the main phase can be observed. From this systematic increase in Mg, $x = 1.075$ seems to have the highest Ag-Mg phase fraction which can be seen by peak intensity of Ag-Mg phase. However, in other samples where $x < 1.075$, the excess Mg is forming Ag-Mg phase but only minute amount and for sample where $x > 1.075$, the excess Mg seems to be contributing to other phases such as MgO which there by reducing the effecting the amount of Ag-Mg phase as the peak intensity of MgO keeps increasing with extra Mg addition. It is also important to note that the MgO phase is minute in all the samples, which is similar to our earlier reports[11]. In order to bolster the above-mentioned conclusions, we did rietveld refinement followed by phase fraction analysis using materials analysis using diffraction (MAUD) software (see Fig. 5.2).

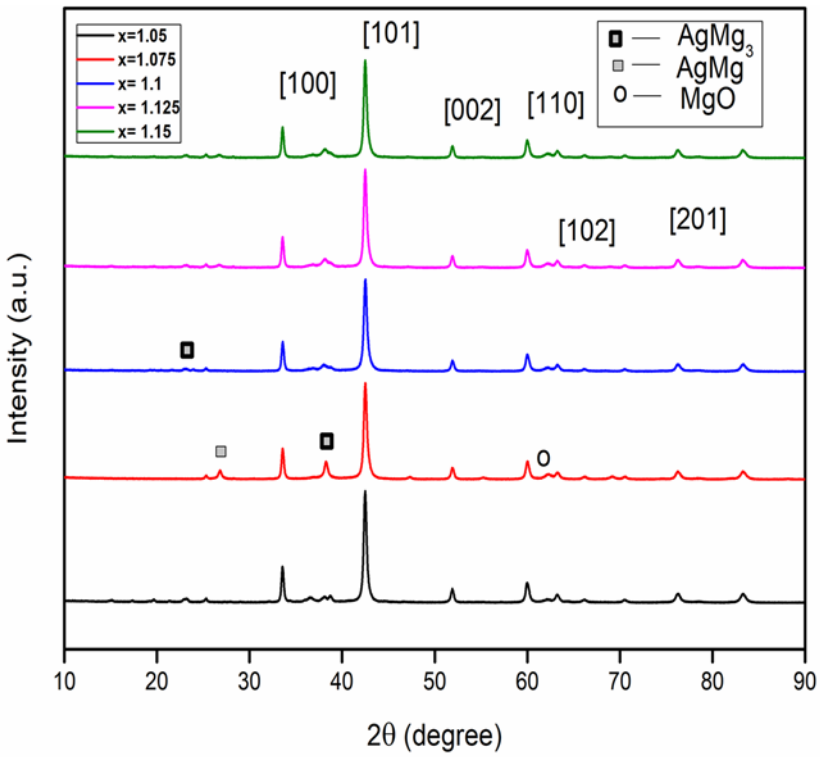

Fig. 5.1: XRD of Mg_xB_2-CCB 1.5%- Ag 4wt% which shows the optimum Ag-Mg phase formation at x=1.075.

Crystallographic information of MgB_2, MgO and AgMg used to analyze the phase fraction are P6/mmm (CIF ref: 1000026), Fm-3m (CIF ref: 1000053) and Pm-3m (CIF ref: 1509457) respectively. We found that the highest AgMg phase fraction percentage of around 2% is observed in the x=1.075

sample while in the highest excess Mg added sample showed only 0.3 wt% AgMg phase. In addition, it can be noticed from peak intensity as well as phase fraction that when excess Mg beyond x = 1.075 is added, formation of MgO is favored over AgMg, thereby diminishing the superconducting performance. Rietveld phase fraction analysis showed that the MgO phase fraction is around 4.9%, 6.43%, 6.78%, 6.9% and 7.34% for samples x = 1.05. 1.075, 1.1, 1.125 and 1.15 respectively.

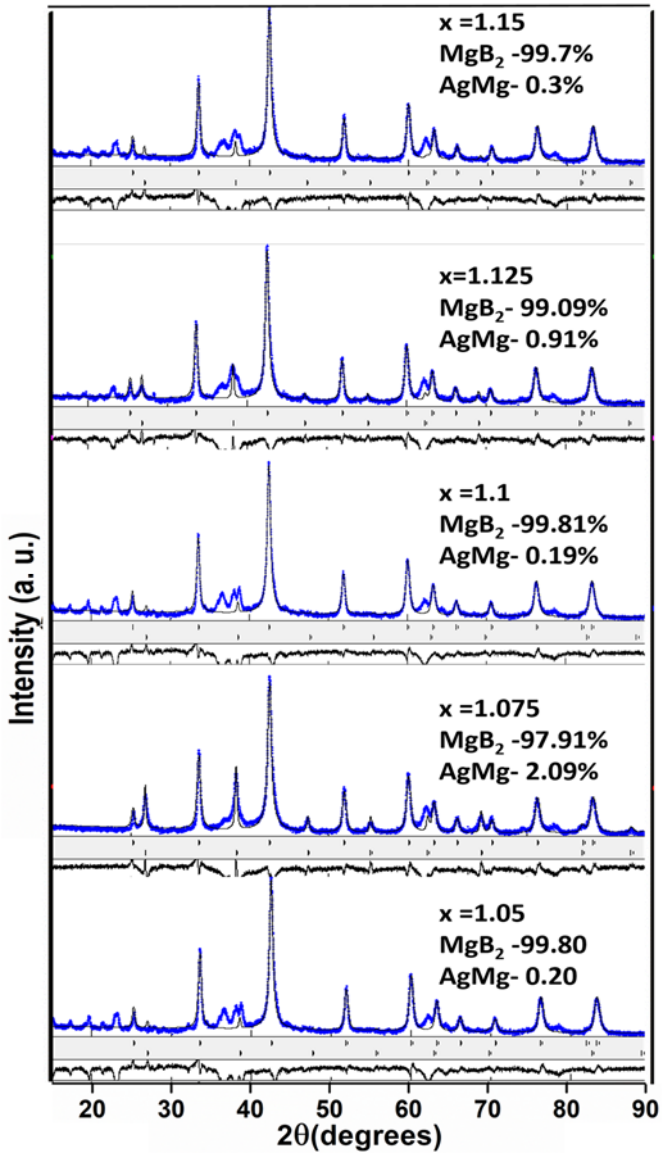

Fig. 5.2: Phase fraction calculation of Mg_xB_2-CCB 1.5%- Ag 4 wt%, Ag-Mg phase fraction is high in x = 1.075 sample. (using MAUD software).

5.3.2 Magnetic properties

To study the effect of this excess Mg addition on the superconducting properties of bulk Mg_xB_2. SQUID measurements have been done to determine the superconducting transition temperature (T_c) as well as superconducting critical current density (J_c).

Table. 5.1: Depicts the detailed information on superconducting critical temperature onsets ($T_{c(onset)}$) and offsets ($T_{c(zero)}$). ΔT_c is approximately 1 K.

Mg precursor concentration (x)	$T_{c(onset)}$, K	$T_{c(zero)}$, K	ΔT_c, K
1.05	37.3	36.57	0.73
1.075	37.43	36.42	1.01
1.1	37.43	36.23	1.2
1.125	37.52	36.3	1.22
1.15	37.36	36.03	1.33

Superconducting critical transition temperatures of all samples in detail can be seen in Table. 5.1, But the T_c is slightly lower than 39 K ranging from 37.3 to 37.5 K, which is expected from a doping. Coming to the superconducting transition temperature (T_c), for clear understanding, we have plotted the first derivative of DC magnetic moment against temperature (see Fig. 5.3, 5.4).

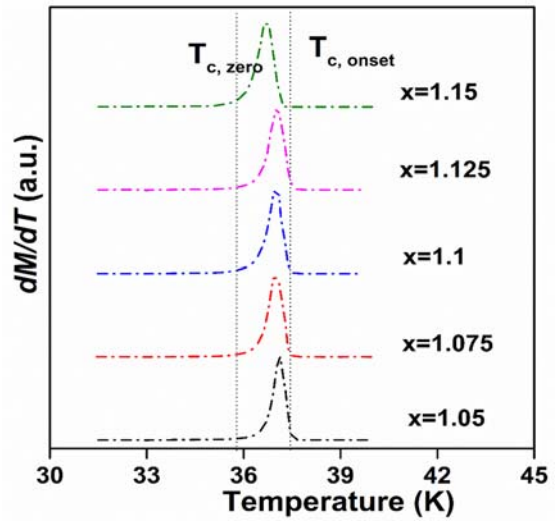

Fig. 5.3: First derivative of DC susceptibility vs temperature profiles of various Mg excess (Mg_xB_2-CCB 1.5%-Ag 4 wt%) added samples. T_c is around 37.5 K as expected of carbon addition.

All the samples have a sharp superconducting transition, which shows that ΔT_c is approximately 1 K. However, the ΔT_c is increasing with the increase in excess Mg addition; this is probably because of the formation of more MgO. T_c of all samples is near to 37.5 K (slightly lower than 39 K), which is expected from a carbon doping in form of carbon encapsulated boron[18]. This reduction is mainly due to carbon but not Ag because, Ag substitution is only possible when added in very less wt% and given a lot of sintering duration [17][19].

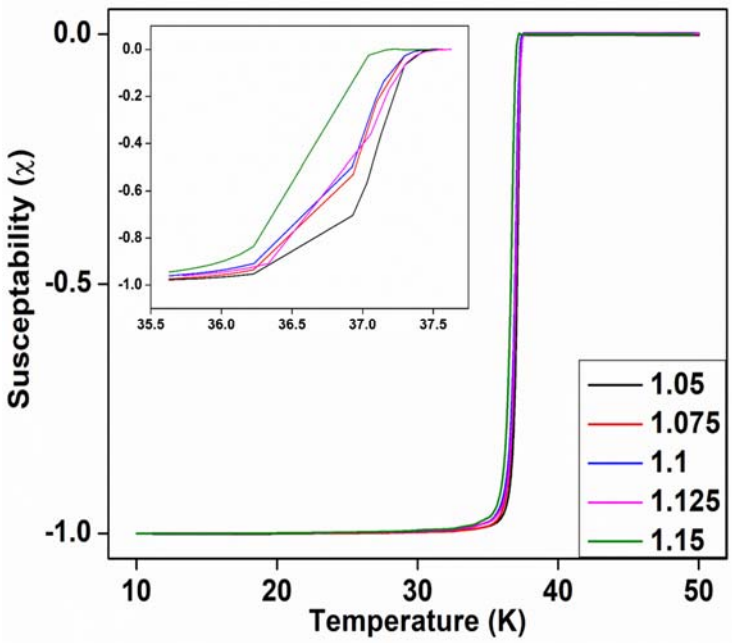

Fig. 5.4: Temperature dependence of magnetic susceptibility for MgB_2 bulk samples with various Mg precursor concentrations. All samples show sharp superconducting transition.

Hence, it is difficult for Ag to be substituted in MgB_2 lattice in our case. $T_{c(onset)}$ increases with increase in excess Mg concentration which might imply that Mg is sufficient enough to form high percentage of MgB_2 superconducting phase. The detailed information on superconducting critical temperature onsets ($T_{c(onset)}$) and ΔT_c can be found elsewhere [20].

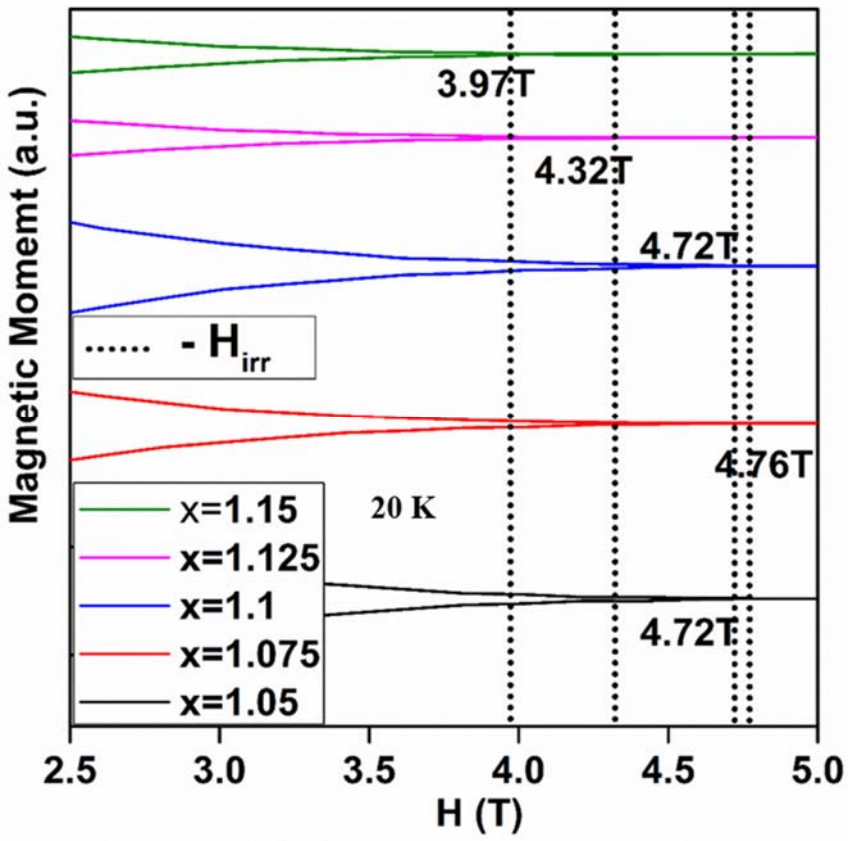

Fig. 5.5: Magnetization loops of systematically excess Mg added samples (Mg_xB_2-CCB 1.5%-Ag 4 wt%). Sample x = 1.075 shows high critical field or H_{irr}

M-H loops are studied to estimate the H_{irr} (Irreversibility field) and later are used to calculate superconducting critical current density (J_c). H_{irr} is value field strength at J_c equivalent to 100 A/cm^2. It is surprising to see the H_{irr} and J_c to be in accordance with the phase fraction of Ag-Mg phase. The highest H_{irr} is for sample x = 1.075 which is 4.76 T at 20 K, while that of a normal pristine sample is around 4.3 T[21], additional details for other samples can be found in Fig. 5.5. This indicates that addition of excess Mg along with usage of Ag and CCB can ascend the usage of MgB_2 up to high field applications. Simultaneously, the highest J_c is seen in x = 1.075 sample. 347 kA/cm^2 at self-field, 244 kA/cm^2 at 0.5 T and 136 kA/cm^2 at 1 T, while the values of pure sample is around 220 kA/cm^2 at self-field. J_c trends for other samples can be seen in Fig. 5.6, 5.7.

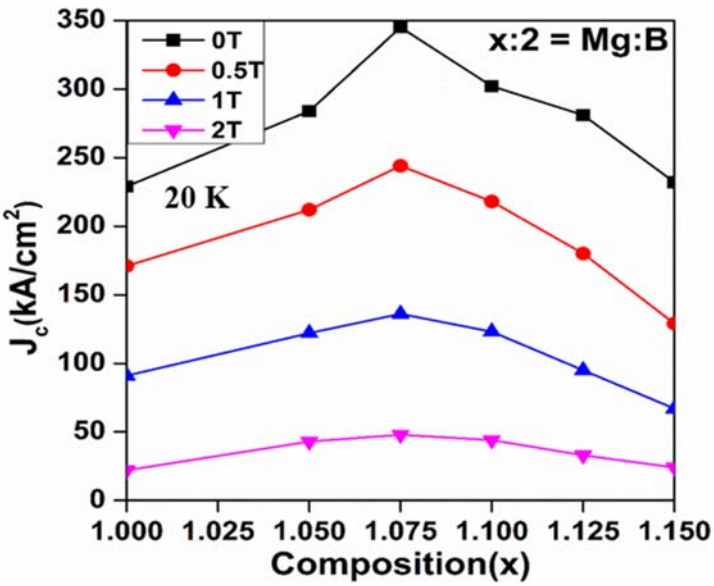

Fig. 5.6: Superconducting critical current density of various excess Mg added samples (Mg_xB_2-CCB 1.5%-Ag 4 wt%) at various magnetic fields. At high fields and low fields, x = 1.075 sample shows best performance.

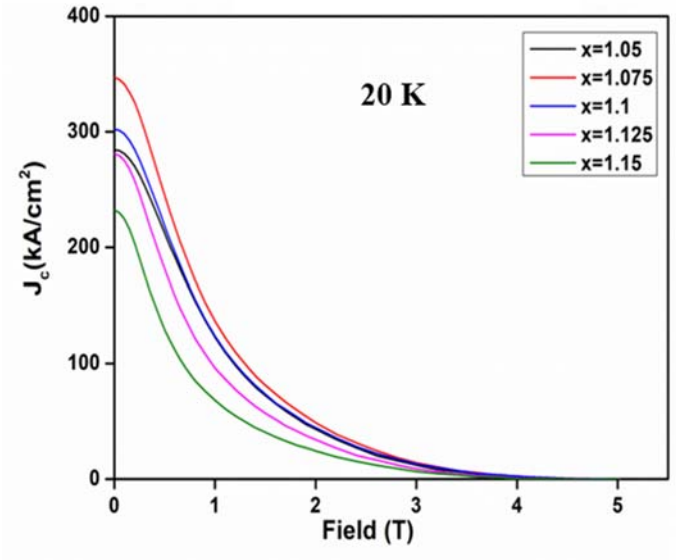

Fig. 5.7: Field dependence of critical current densities for Mg_xB_2-CCB 1.5% and 4wt% Ag, at 20 K. at x = 1.075 highest J_c can be observed.

It can be concluded that the excess Mg addition along with defects and other high field pinning centers is a contributing factor for improving the high field J_c. Similar effects have been observed in previous research such as optimizing Ag addition in MgB_2. It was reported that $AgMg_3$ phases formed

acts as flux pinning centers in MgB_2 responsible for the improved J_c [16][22][23]. Also, formation of tiny MgB_2 grains because of Ag addition was shown by AFM studies and the density improvement was also observed as the Ag-Mg particles fill in the voids [24]. In addition, mechanical properties are also enhanced because of the Ag-Mg alloy particles distribution in the matrix [16]. Later it was also considered that Ag addition that results in Ag-Mg alloys phase that has high thermal conductivity and will aid in suppressing flux jumps [25], [19]. Furthermore, this scenario of additive reacting with Mg in matrix is observed even in SiC doping where Mg_2Si, an Mg-Si based compound is formed which is responsible for the J_c improvement [26]. These J_c trends are also in congruence with X-ray and phase fraction analyzed data. This accordance is as per our assumption that when excess Mg is beyond x = 1.075, formation of MgO is favored over AgMg phase, thereby diminishing the superconducting performance there by resulting in low J_c.

5.3.3 Flux pinning diagrams

To evaluate the normalized pinning force density for a material, we used Dew-Hughes general expression

$$F_p/F_{p,max} \propto h^p(1-h)^q \qquad 5.1$$

In the above equation 5.1, p and q are dimensionless parameters that vary with flux pinning mechanism. Based on this evaluation, different types of pinning centers as well as mechanisms are attributed for different values of p and q. Usually, if the peak position or h_{max} ~ 0.2 the dominant pinning is from grain boundaries, if h_{max} ~ 0.33 pinning is from normal conducting inclusions and if h_{max} ~ 0.5 the pinning is from weak superconducting areas [27]. In order to understand the flux pinning characteristics in our sample, we have plotted and studied the normalized flux pinning force curve against reduced magnetic field. In this curve $f_p=F_p/ F_{p,max}$ is plotted against $h=H_o/H_{irr}$ at 20K, where H_{irr} is the irreversibility field obtained from M-H loops. Here we determined H_{irr} criterion as field where J_c ~ 100 A/cm^2 [28], similar to our previous literature [11][16][20][27]. In our system, the peak position is located at h_{max} = 0.2 (see Fig. 5.8), which indicates that the dominant mechanism for the pinning is grain boundary pinning (δl pinning).

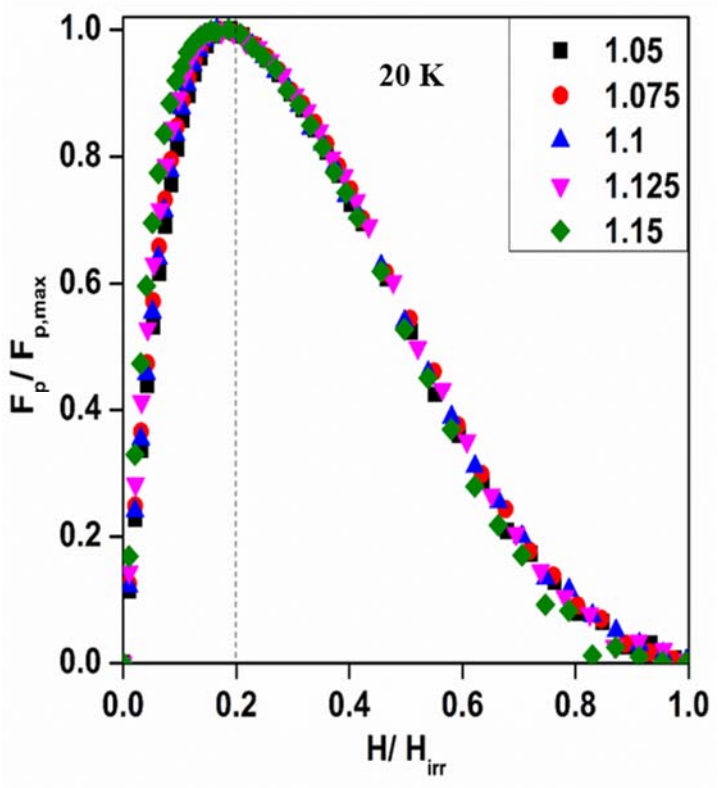

Fig. 5.8: Flux pinning diagrams calculated from the M–H loops using Dew–Hughes model. Peak position lies at approximately 0.2 which indicates the primary pinning mechanism is grain boundary pinning.

This result is in accordance with previous studies for which normal and surface pinning dominate within grains. Precisely the grain boundaries within the Ag-Mg nanoparticle layer are contributing to the pinning at self-field. In our previous work, the f_p vs h peak was at 0.17 when we used nano amorphous boron without any additives or dopants used [11]. The fact that peak shifted from 0.17 to 0.2 means that the contribution of 3D-defect pinning or δT_c pinning has improved, although the primary pinning is from grain boundaries[21]. Presence of Ag-Mg phases along with lattice distortion from CCB addition is responsible for this shift in the flux pinning peak position.

5.3.4 Levitation Force Measurements

Levitation force is a parameter reflecting the bulk's ability to suspend a powerful magnet, which is close to trapped field. In order to get an understanding of trapped field properties, we carried out levitation force measurement. Fig. 5.9 shows the levitation force measured at 20 K on

10 mm diameter MgB_2 bulk made of commercial boron and the present best bulk (10 mm diameter), 7.5 wt% excess Mg based MgB_2 after field cooling. The bulk samples were field-cooled under 45 mm diameter permanent magnet (NdFeB) at distance of 30 mm. Later, levitation force between the magnet and superconducting magnet was measured while varying the z-position/distance of the probe at 20, 30 and 40 mm. As could be expected, the levitation force increased as the separation between the superconductors and the magnet decreased. The levitation force of 7.5 wt% excess Mg based MgB_2 bulk was approximately by 25% higher than that of the conventional commercial boron-based MgB_2 bulk. This increase is attributed to the improved J_c in the 7.5 wt% excess Mg based MgB_2. Since both the levitation force as well as J_c (parameters directly proportional to trapped field value) improved significantly, it can be assumed that the 7.5 wt% excess Mg based MgB_2 can also exhibit superior trapped field value.

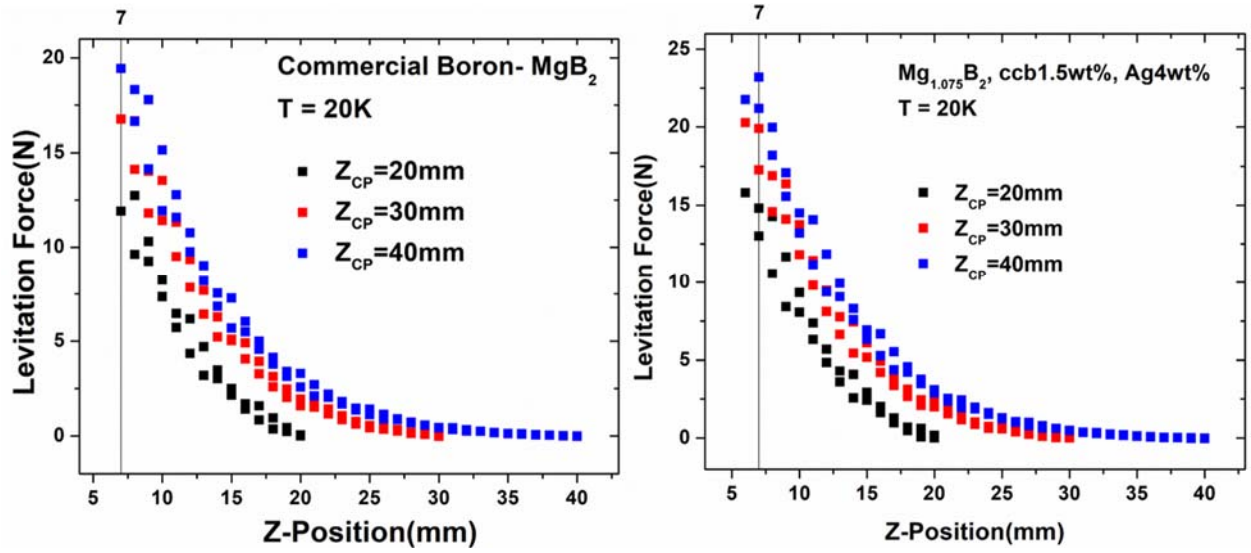

Fig. 5.9: Levitation force measured at 20 K on 10 mm diameter MgB_2 bulk made from commercial boron and the present best bulk (10 mm diameter), 7.5 wt% excess Mg based MgB_2.

5.3.5 Microstructural Analysis

Density calculations on prepared bulks were done using the formula, *desnity = Mass/ Volume* and arrived at a range of density, approximately 1.12-1.16 g/cm^3 that accounts to half of theoretical density of MgB_2 (2.6 g/cm^3). All of our samples and in general, bulk MgB_2 synthesized by conventional sintering show this behavior. To confirm the mechanisms responsible for the J_c improvement we have done microstructural analysis by scanning electron microscopy (SEM). It

can be observed from low magnification SEM images (left) and back scattered images (right) in Fig. 5.10 that secondary phases, mostly Ag-Mg based (white) are formed inside the matrix (black) and seem to be contributing for the flux pinning.

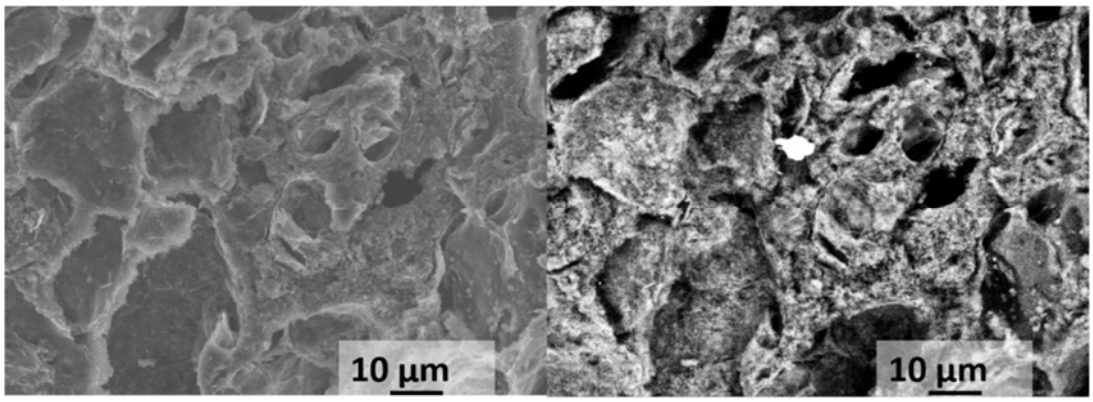

Fig. 5.10: Low magnification SEM analysis of Mg rich MgB_2 samples. AgMg phase (white) in the MgB_2 matrix (black); SEI image (left), comp image (right).

The white colored secondary phases are most likely Ag-Mg, while the matrix being MgB_2. On the other hand, high magnification images tell us that Nano-particle layers of Ag-Mg phases are formed in grain boundaries (see Fig. 5.11). To confirm the presence of these layers throughout the sample, we tried performing elemental mapping using Energy dispersive X-ray spectroscopy (EDX) in FE-SEM. The mapping (see Fig. 5.12) shows uniform distribution of Ag, which thereby tells us that these Ag-Mg layers are formed throughout the sample. In addition, uniform carbon distribution can also be observed since we have used carbon encapsulated boron as precursor.

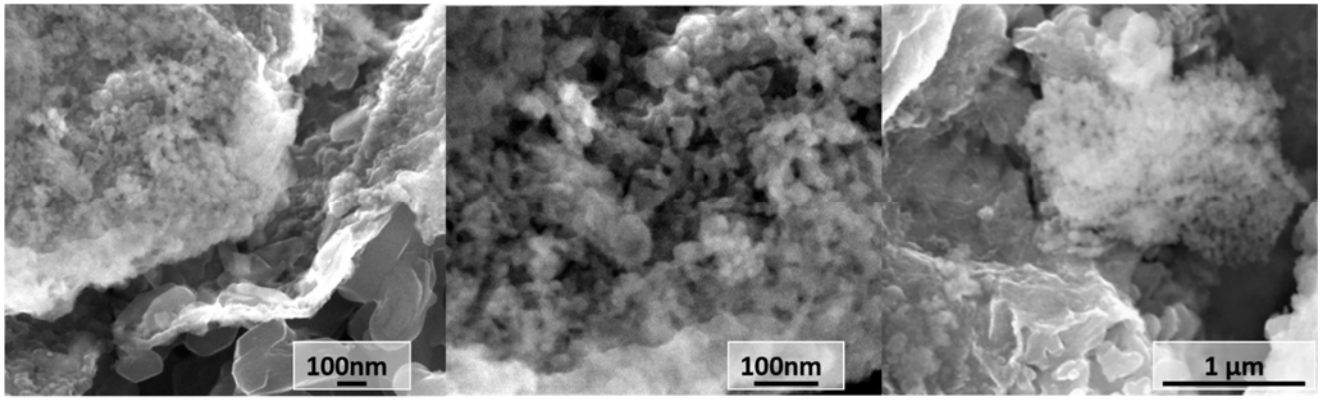

Fig. 5.11: High magnification SEM images of the layer structure over the big MgB_2 grains. Grain refinement up to 20–40 nm can be seen.

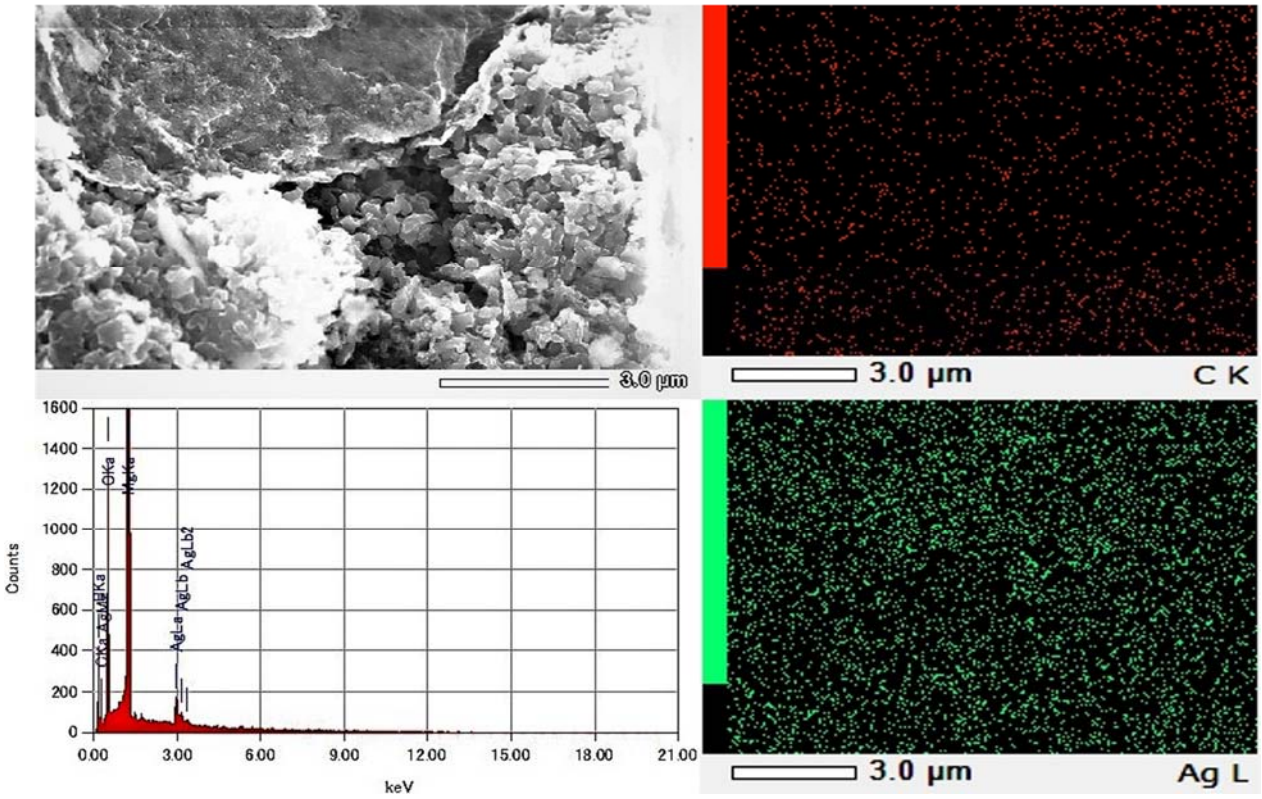

Fig. 5.12: EDX analysis of microstructure using SEM. Microstructure (left-top) indicates a nano-layer different from matrix. The peaks intensity or counts (left-bottom) show the Ag presence in the layer of the matrix. Distribution images (right) shows the uniformity of carbon from CCB (top) and Ag (bottom) in the matrix.

These results can clarify upon any suspicion over non-uniform distribution of dopants in the sample. These layers have Ag-Mg nanoparticles around 20-30 nm, which increase the number of grain boundaries that might be contributing to the zero field critical current density. Flux pinning diagrams are calculated to determine the dominant pinning mechanism. To deeply study the best sample's behavior we tried to measure the M-H loops at various temperatures (10, 15, 20, 25, 30 and 35 K) and calculated the J_c and flux pinning diagrams to observe the change in mechanisms with temperature. High J_c such as 521 kA/cm^2 was observed at 10 K, while it dropped steadily with increase in temperature. J_c of 441, 350, 250, 141 and 27 kA/cm^2 was noted at 15, 20, 25, 30 and 35 K respectively (see Fig. 5.13). Flux pinning diagram reveals that at high temperatures the peak is at h ~ 0.3, while low temperatures it is at h ~ 0.22 (see Fig. 5.14) which shows that the

dominant pinning mechanisms slightly changes with temperature, this is in accordance with previous research [27].

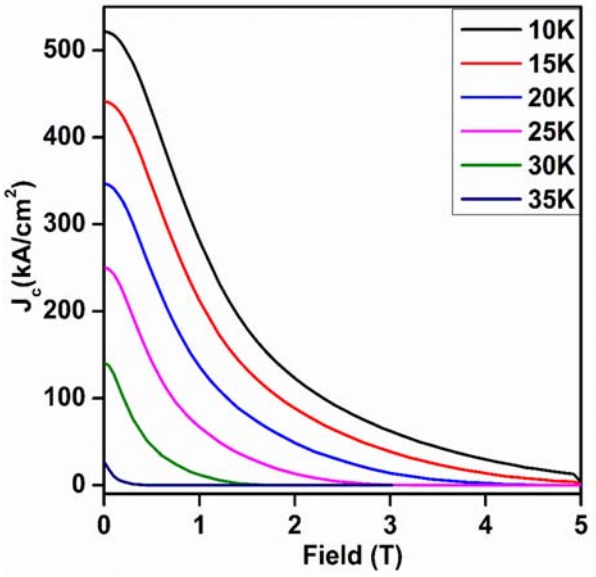

Fig. 5.13: Superconducting critical current density vs temperature curves of the beast sample at various temperatures. Exceptional value such as 521 kA/cm^2 J_c is observed at self-field, 10 K.

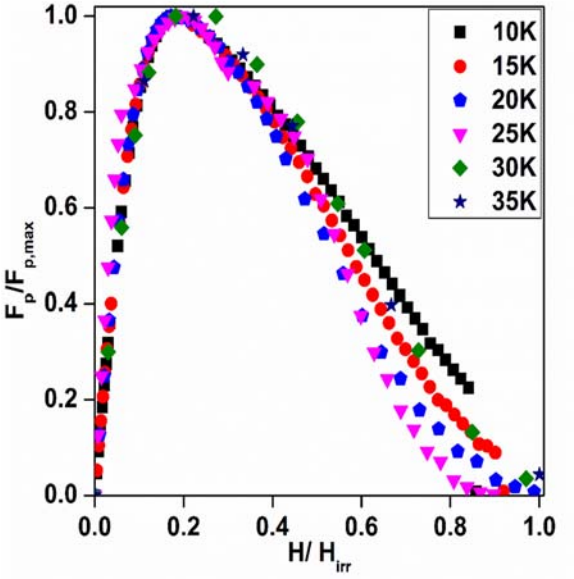

Fig. 5.14: Flux pinning diagrams of the best sample at various temperatures. $F_p/F_{p,max}$ is located close to 0.2 indicating the dominant grain boundary pinning does not change with the temperature after addition of excess Mg, Ag, and CCB usage.

Therefore, we think that slightly excess Mg addition is necessary and beneficial in obtaining optimum pinning effect from Ag addition in solid-state sintered bulk MgB_2 system.

5.4 Summary

Bulk MgB_2 samples with variation in excess Mg precursor has been synthesized in Argon atmosphere via solid-state sintering process at 775 ºC. XRD analysis shows that peak corresponding to Ag-Mg phase is strong when x = 1.075 (in Mg_xB_2), which is also reflected in phase fraction analysis. Critical temperatures of all the samples is close to 37.5 K, because of usage carbon-encapsulated boron, but have sharp transitions, ΔT~1 K. M-H loops show that the sample with 7.5wt% excess Mg or $Mg_{1.075}B_2$ (best sample) has high irreversibility field (H_{irr}) such as 4.76 Tesla. In correspondence with XRD, the best sample showed the highest J_c such as 520, 440, and 347 kA/cm^2 at 10, 15 and 20 K respectively. SEM analysis confirmed the presence of secondary Ag-Mg phases and improved microstructural changes such as particle refinement, up to 20-40 nm. Hence, the results suggest that using 1.075:2 ratio of Mg:B is crucial for development of high performance bulk MgB_2 material while using CCB and Ag addition.

5.5 References

[1] J. Nagamatsu, N. Nakagawa, T. Muranaka, Y. Zenitani, J. Akimitsu, *Nature* **2001**, *410*.

[2] D.C. Larbalestier, J. Jiang, D.M. Feldmann, L.D. Cooley, S. Patnaik, A. Gurevich, P. Khalifah, M.A. Hayward, R.J. Cava, K. Inumaru, X.Y. Cai, J.S. Slusky, C.B. Eom, E.E. Hellstrom, A.A. Polyanskii, M.O. Rikel, A.A. Squitieri, T. He, K.A. Regan, M. Haas, N. Rogado, M.T. Naus, *Nature* **2001**, *410*, 186.

[3] D.K. Finnemore, J.E. Ostenson, S.L. Bud'ko, G. Lapertot, P.C. Canfield, *Phys. Rev. Lett.* **2001**, *86*, 2420.

[4] K. Kajikawa, T. Nakamura, *IEEE Trans. Appl. Supercond.* **2009**, *19*, 2.

[5] N.P. Bansal, J.C. Goldsby, R.B. Rogers, M.A. Susner, M.D. Sumption, *J. Alloys Compd.* **2015**, *622*, 986.

[6] K. Vinod, R.G. Abhilash Kumar, U. Syamaprasad, *Supercond. Sci. Technol.* **2007**, *20*.

[7] B.T. Matthias, T.H. Geballe, S. Geller, E. Corenzwit, *Phys. Rev.* **1954**, *95*, 1435.

[8] S.X. Dou, S. Soltanian, J. Horvat, X.L. Wang, S.H. Zhou, M. Ionescu, H.K. Liu, P. Munroe, M. Tomsic, *Appl. Phys. Lett.* **2002**, *81*, 3419.

[9] A. Gümbel, J. Eckert, G. Fuchs, K. Nenkov, K.H. Müller, L. Schultz, *Appl. Phys. Lett.* **2002**, *80*, 2725.

[10] J.G. Noudem, M. Aburras, P. Bernstein, X. Chaud, M. Muralidhar, M. Murakami, *J. Appl. Phys.* **2014**, *116*.

[11] S.S. Arvapalli, M. Muralidhar, M. Murakami, *J. Supercond. Nov. Magn.* **2018**, 2.

[12] Y. Bugoslavsky, L.F. Cohen, G.K. Perkins, M. Polichetti, **2001**, 561.

[13] Y. Zhao, Y. Feng, C.H. Cheng, L. Zhou, Y. Wu, T. Machi, Y. Fudamoto, N. Koshizuka, M. Murakami, *Appl. Phys. Lett.* **2001**, *79*, 1154.

[14] M. Muralidhar, M. Murakami, *Phys. C Supercond. Its Appl.* **2001**, *360*, 657.

[15] M. Farbod, M.R. Batvandi, *Phys. C Supercond. Its Appl.* **2011**, *471*, 112.

[16] M. Muralidhar, K. Inoue, M.R. Koblischka, A. Murakami, M. Murakami, *J. Adv. Eng. Mater.* **2015**, *17*, 831.

[17] T. Sun, X.P. Zhang, Y.G. Zhao, R. Shen, K. Wang, L.W. Zhang, B.S. Cao, Y.H. Xiong, P.J. Li, H.H. Wen, *Phys. C Supercond. Its Appl.* **2002**, *382*, 367.

[18] M. Muralidhar, M. Higuchi, M. Jirsa, P. Diko, I. Kokal, M. Murakami, *IEEE Trans. Appl. Supercond.* **2017**, *27*, 18.

[19] Y. Kimishima, S. Takami, M. Uehara, S. Numa, Y. Sugiyama, T. Kuramoto, *Phys. C Supercond. Its Appl.* **2008**, *468*, 1181.

[20] S.S. Arvapalli, M. Miryala, M. Murakami, *IEEE Trans. Appl. Supercond.* **2019**, 1.

[21] M. Mudgel, V.P.S. Awana, H. Kishan, G.L. Bhalla, *Solid State Commun.* **2008**, *146*, 330.

[22] S.X. Dou, A. V. Pan, S. Zhou, M. Ionescu, H.K. Liu, P.R. Munroe, *Supercond. Sci. Technol.* **2002**, *15*, 1587.

[23] D. Kumar, S.J. Pennycook, J. Narayan, H. Wang, A. Tiwari, *Supercond. Sci. Technol.* **2003**, *16*.

[24] D. Kumar, M. Muralidhar, M.S.R. Rao, M. Murakami, *J. Supercond. Nov. Magn.* **2018**, *31*, 2033.

[25] T.H. Johansen, M. Baziljevich, D. V. Shantsev, P.E. Goa, Y.M. Gal Pe Rin, W.N. Kang, H.J. Kim, E.M. Choi, M.S. Kim, S.I. Lee, *Europhys. Lett.* **2002**, *59*.

[26] A. Vajpayee, R. Jha, A.K. Srivastava, H. Kishan, M. Tropeano, C. Ferdeghini, V.P.S. Awana, *Supercond. Sci. Technol.* **2011**, *24*.

[27] M. Muralidhar, K. Inoue, M.R. Koblischka, M. Tomita, M. Murakami, *J. Alloys Compd.* **2014**, *608*, 102.

[28] M.R. Koblischka, M. Muralidhar, *Int. J. Mod. Phys. B* **2016**, *30*, 1630017.

Chapter 6

High Energy Ultra-sonication of Boron Powder for High-Performance Bulk MgB_2.

6.1 Size reduction of boron particles by high-power ultrasonication in ethanol media for optimization of bulk MgB_2

6.1.1 Introduction

MgB_2 is a trendy material suitable for several superconductor applications such as bulk magnets for compact MRI & NMR, electric motors etc. Although T_c is slightly lower (39 K) [1] compared to superconducting cuprates (~90 K), the processing time, easy fabrication and cost parameters make it attractive. With liquid helium cooling would be usage of MgB_2 difficult and expensive in practical applications. However, cryogen-free cryo-coolers [2–4], liquid hydrogen[5] and neon are capable of reaching the required cooling temperature without expensive and technically complicated use of liquid helium. This promotes a rapid research on MgB_2 superconducting material. The light weight is another factor improving efficiency of the devices and increasing the range of applications [6–11], especially in space. Several research groups have been trying to improve trapped field and critical current density in MgB_2 bulks. Most of the trials were related to optimization of synthesis parameters [12,13], novel synthesis techniques[14–16], refining the raw precursors, doping, additions[17,18], and fabrication of films [19]. The primary synthesis method for bulk MgB_2 is the solid state sintering. This process is highly scalable and by maintaining uniformity in synthesis parameters, one can obtain uniformity in product's properties, such as elemental distribution, density, J_c etc. In addition, this sintering method also ensures a uniform trapped field, which is crucial for levitation and super-magnet device fabrication. Some researchers have tried manipulating the sintering temperature, sintering duration, multi-step heating [13,20–24] etc. In our previous research we have optimized the sintering process such 775-800 ^oC for 3 hours for best performance bulk MgB_2 [12]. One small disadvantage is the need of an inert

atmosphere during the sintering, as Mg is highly reactive with oxygen. Anyway, it doesn't hinder massive production of bulk MgB_2 material. Different techniques and synthesis methods were also practiced such as spark plasma sintering [25–27], diffusion method [16], infiltration growth [28] and chemical routes (combustion, pyrolysis, precipitation etc.). All these methods have their advantages and disadvantages. One way that can improve superconducting performance is to introduce pinning centers to pin vortex lattice motion and thereby reach a high performance up to high magnetic fields. The coherence length of MgB_2 materials is quite high when compared to other HT superconductors. Hence, defects with bigger sizes can thus act as pinning centers. Some of the effective pinning centers used are non-superconducting inclusions, defects, grain boundaries, voids etc. Such pinning centers can be MgB_4 [29,30], MgO [31,32], metals [33,34], metal oxides [35,36], grain refiners, rare-earth elements [37], dislocations, defects created by irradiation [38], carbon doping [39–46] etc.

It has been proven that increase of grain boundary area results in increase of J_c, in particular at low magnetic fields. In one of our previous work dealing with MgB_2 we used a commercial nano-amorphous boron [47] to enhance vortex pinning. The results were outstanding, but the powder was expensive, making the whole fabrication process costly. Ball milling is a technique proved to effectively decrease powder size, however is not scalable and has problems like poor T_c, B_2O_3 formation and contamination by other impurities [48,49]. Here, we utilized "High Energy Ultra-sonication", a novel technique that is scalable and results in uniformly refined particles [50,51]. It generates powerful waves using vibration of a metal probe. The high-energy waves cause turbulence in the medium and pass high energy to the particles, which then bombard each other and the container walls, resulting in particles breakage. In addition, tiny air bubbles or cavities are formed that release destructive forces inside the solution when popped. It results in the particles splintering. An important advantage of this method is that the process can be controlled and optimized via tuning frequency and power. However this process is new, the interaction between dispersant and dispersion is crucial. Optimum conditions for the best results need to be established. In the present work, we tried to ultra-sonicate the cheap commercial boron in ethanol medium to increase the grain boundary area in the final microstructure to produce high performance bulk MgB_2 while preserving the T_c.

6.1.2 Experimental:

i) Boron ultra-sonication: In order to develop a cheap, scalable fabrication process, we ultra-sonicated cheap commercial boron (Furu-uchi chemicals, 300 mesh, 99% purity) using ultra-sonication (Mitsui ultrasonic Homogenizer). The working principle comprises generation of high power waves in the beaker containing boron powder dispersed in ethanol. In this experiment, we systematically varied the ultra-sonication time such as 30, 60, 90 and 120 minutes, maintaining power constant, at 50% (150 W) and frequency at 20 kHz. The power was switched ON and OFF alternatively every 30 seconds. This ensured that the metal tip generating pulses got enough time to cool off the entire heat produced by the particles bombardment. Thus the real ultra-sonication times were 15, 30, 45, and 60 minutes. Immediately after the ultra-sonication, the powder was heated at 100 ^{o}C for one hour in a muffle furnace to remove ethanol. Later, the powders were characterized by scanning electron microscope (SEM) as well as transmission electron microscope (TEM JEOL/ JEM-2100) to confirm the size reduction.

ii) Synthesis of MgB_2: The precursors were commercial powders (Furu-uchi Chemical Corporation) of amorphous Mg powder (99.9% purity, 200 meshes) and an ultra-sonicated boron powder. One gram of MgB_2 was synthesized using 0.529 g of Mg and 0.471 g of B (ultra-sonicated) in the molar ratio of 1:2. The powders were rigorously mixed and ground in a glove box and heat treated after pelletizing as discussed in Chapter 2. The pellets were then removed out from thr furnace and the outer surfaces are polished to avoid any surficial MgO formed. From here on we address the various MgB_2 bulks as B-0, B-15, B-30, B-45 and B-60 corresponding to the boron precursor used which is ultrasonicated for 0, 15, 30, 45 and 60 minutes respectively.

These bulks were later characterized using XRD, FE-SEM, TEM and SQUID for understanding phase purity, microstructure, compositional analysis and superconducting properties respectively.

6.1.3 Results and Discussion

Ball milling as a standard technique for boron powder refinement is not suitable for industrial use because of the impurities, mainly B_2O_3 created during this process. XRD analysis revealed that the amount of B_2O_3 raised with increasing milling time, which resulted in a decrease of T_c of the MgB_2 bulk[49]. The ultra-sonication process doesn't show such a drawback. XRD results proved absence

of B_2O_3 diffraction peaks even after 1 hour of ultra-sonication (100% intensity peak- usually at approx. $2\theta = 27.8^{o}$), as shown in Fig. 6.1. Note that any oxides in the precursor promote formation of MgO, which is detrimental to the superconducting properties.

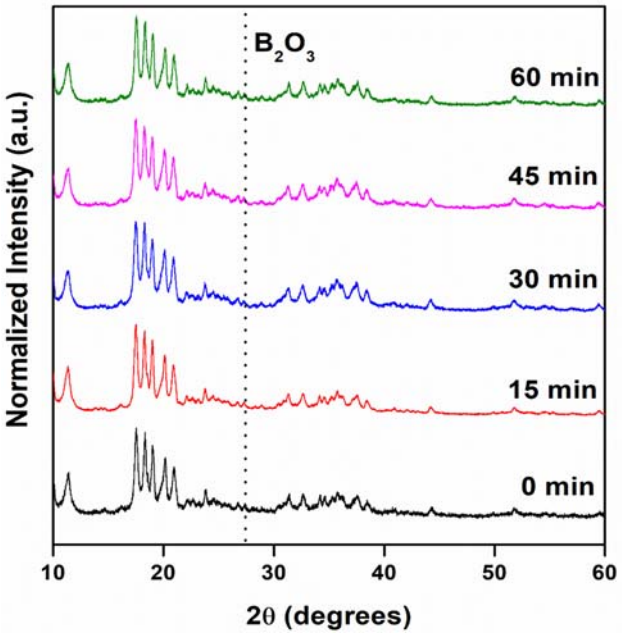

Fig. 6.1: XRD of the ultra-sonicated Boron (0, 15, 30, 45, 60 minutes). All diffraction patterns showed no signs of B_2O_3 formation.

The particles size was studied by means of SEM. Figs. 6.2 (a-e) shows the SEM micrographs of pure and 15, 30, 45 and 60 minutes ultra-sonicated boron. The particles size was significantly reduced with ultrasonication. Transmission electron microscopy revealed particles' size reduction (see Fig. 6.3) upto 20 – 50 nm after 15 min ultra-sonication in ethanol medium. In addition, clustering or agglomeration can be observed in boron powder ultrasonicated for longer than 15min, especially in 30, 45 and 60 min samples as pointed in the Fig. 6.2 (c), (d) and (e). Refinement upto few tens of nanometers can be observed. This implies that although there is size refinement with increase in ultrasonication, longer intervals over 15 minutes can result in clustering. This can be possible because ultrasonication involves collision between particles. We propose that these particles after 15 minutes of bombardment end up with irregular surfaces and smaller sizes which when subjected to further collisions can result in interlocking of particles.

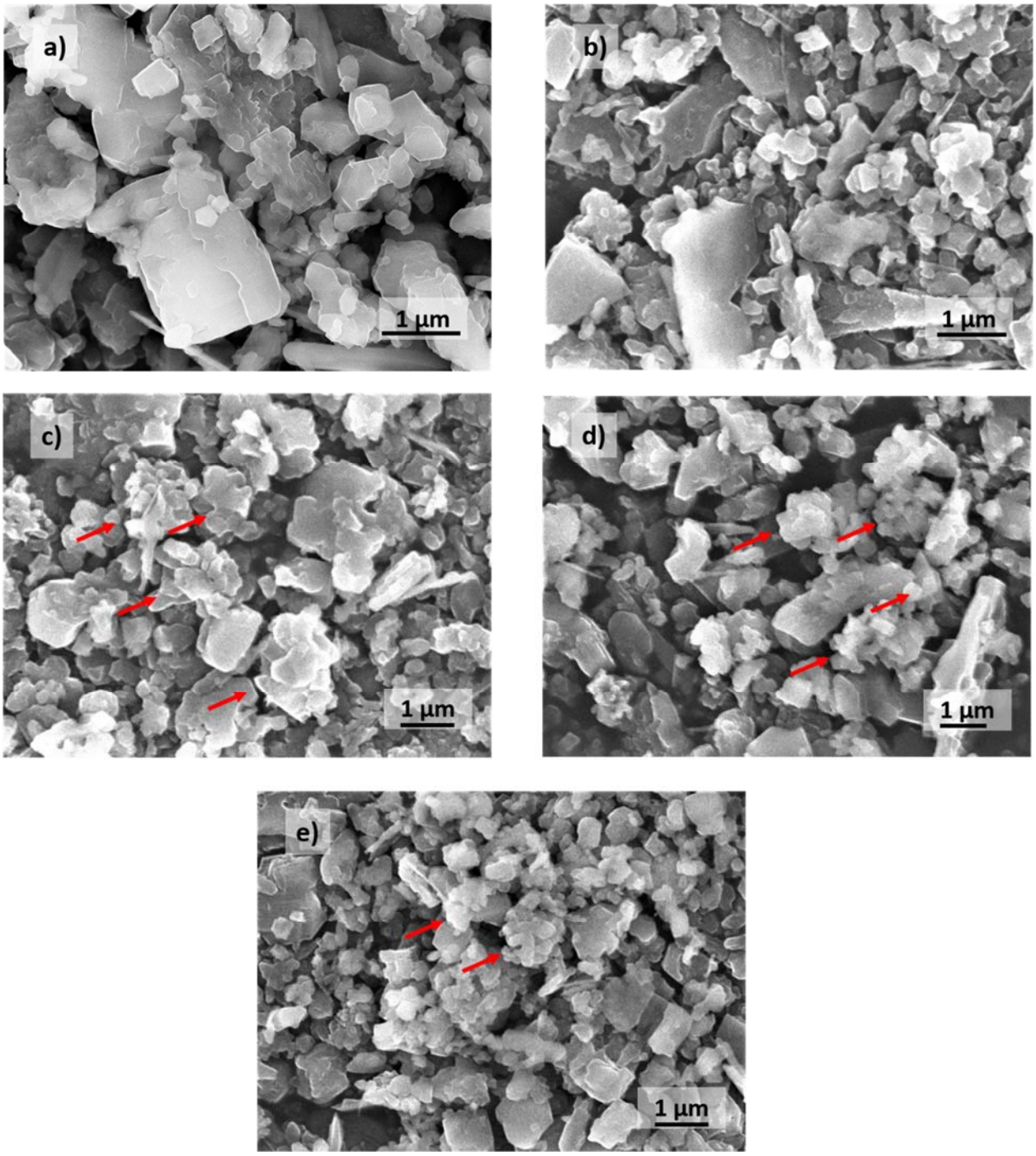

Fig. 6.2: SEM micrographs of a) Pristine cheap commercial boron, b) 15 min ultra-sonicated boron, c) 30 min ultra-sonicated boron, d) 45 min ultra-sonicated boron, and e) 60 min ultra-sonicated boron. Fine particles around few nano meters can be seen after ultrasonication. In higher ultrasonicated powders, clustering can be observed.

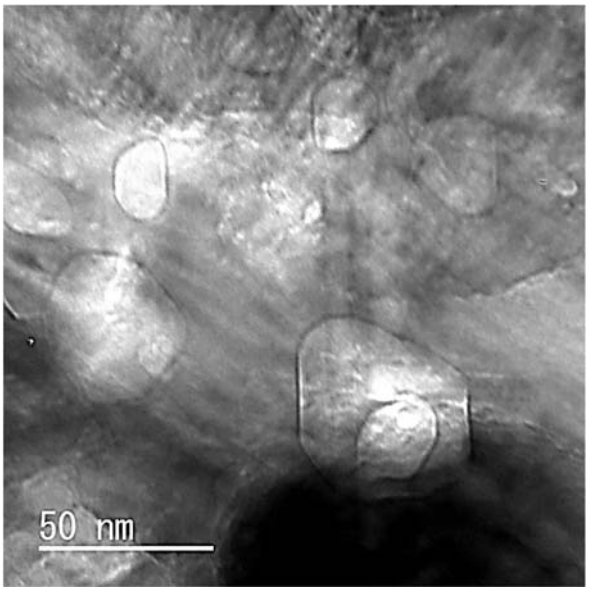

Fig. 6.3: TEM micrograph of 15 min ultra-sonicated boron powder. Tiny particles around 20 -50 nm can be seen.

Another possible explanation can be agglomeration, which is mainly due to the tendency of the system to minimize surface energy [52]. Similar phenomenon was reported recently, when boron was subjected to ball milling for size reduction [49]. The authors concluded that after 2 hours of ball milling, the performance goes down because of volume reduction in MgB_2 phase. They also observed formation of unreacted Mg and B_2O_3. In the case of ultrasonication, very minute amount of MgO was observed and T_c was close to pure MgB_2. Ultra-sonication occurs to be better than ball milling in terms of balanced quality, performance, and processing time.

From the XRD of MgB_2 bulks shown in Fig. 6.4 it is evident that there are no contaminants present in the matrix apart from a scare quantity of MgO, which is formed during the transfer from glove box to furnace and the pressing step. The intensity of MgO [220] peak ($2\theta \sim 62.3^o$) can be seen in the inset figure, which is very small when compared to other peaks. In addition, we compared the [110] MgB_2 peak ($2\theta \sim 60^o$), to check if there was any influence of ethanol such as carbon impartation during ultrasonication. In general, carbon substitutes into boron atoms on boron atomic place which is parallel to c-axis. Hence we choose the [110] plane to determine if there is any carbon substitution. As can be seen from the inset figure of Fig. 6.4, there is no shift in the [110] peak, which confirms that there was no carbon substitution.

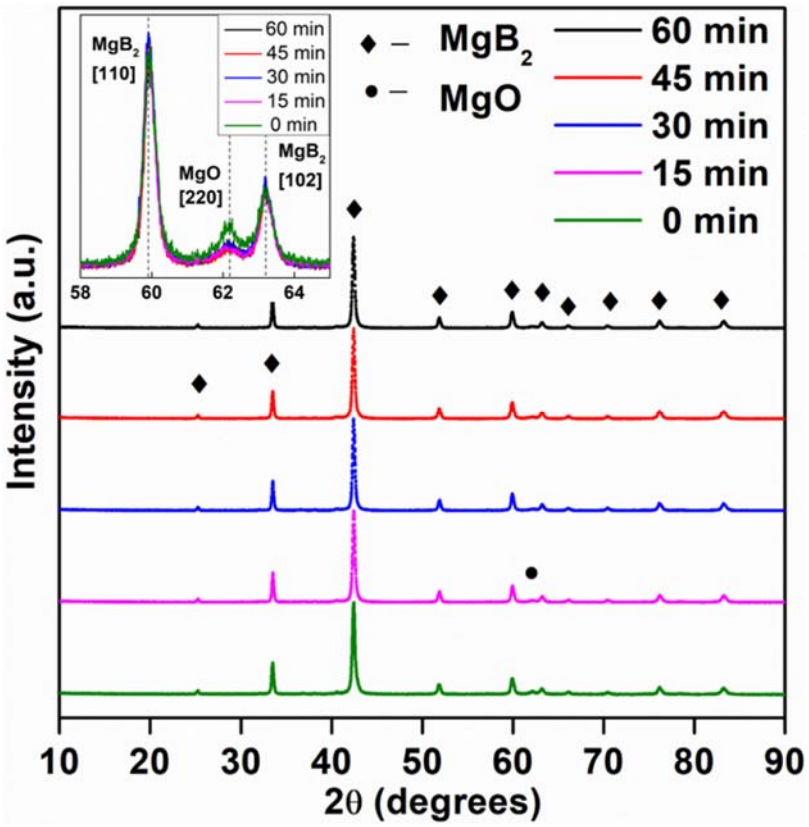

Fig. 6.4: XRD of the ultra-sonicated samples (0, 15, 30, 45, 60 minutes). All diffraction patterns are similar to conventional sintered MgB_2 pattern with scarce MgO impurities.

In accordance with XRD, *M-T* or superconducting critical temperature studies also show a sharp transition, which depicts the high quality bulk MgB_2 synthesis. All the samples show high $T_{c,onset}$ such as 38.5 K and ΔT_c around 0.7 K, more details can be found in Table. 6.1 and Fig. 6.5. These results also point to a high purity, as most of the secondary phases present in a superconducting material result in degradation of critical temperature. Additives and dopants such as carbon in various forms, Ti, Cu, Fe, SiC and others resulted in great decrease in T_c [46,53–57].

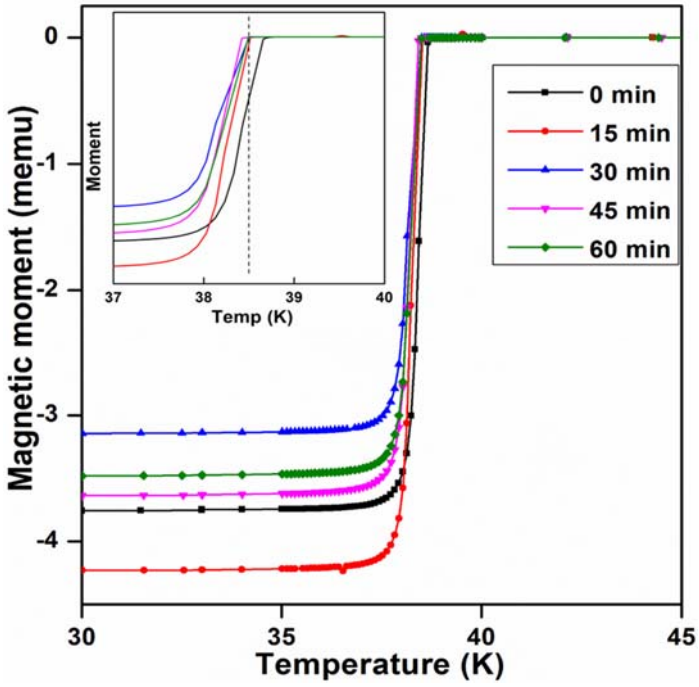

Fig. 6.5: Superconducting transition temperature of ultra-sonicated samples (0, 15, 30, 45, 60 min). All samples show sharp T_c indicating high quality superconducting MgB_2.

Table. 6.1: Critical onset and offset temperatures of bulk MgB_2 samples prepared with ultra-sonicated boron.

Bulk	$T_{c,onset}$ (K)	$T_{c,zero}$ (K)	ΔT_c (K)
MgB_2-0 min Ultra-B	38.7	38	0.7
MgB_2-15 min Ultra-B	38.5	37.8	0.7
MgB_2-30 min Ultra-B	38.5	37.6	0.9
MgB_2-45 min Ultra-B	38.4	37.7	0.7
MgB_2-60 min Ultra-B	38.5	37.8	0.7

Critical current density was plotted in log plots, along with regular curves in the inset. One can see in detail from Fig. 6.6 that B-15 shows high performance, along with improved H_{c2}. Self-field J_c at 20 K raised up to 300 kA/cm^2 in B-15 bulk, while other samples based on boron ultra-sonicated for different other times exhibited constant self-field J_c close to 270 kA/cm^2. Thus, there is about 36% improvement in B-15 and 22 % improvement for B-30, B-45, and B-60 when compared to B-0 (220 kA/cm^2).

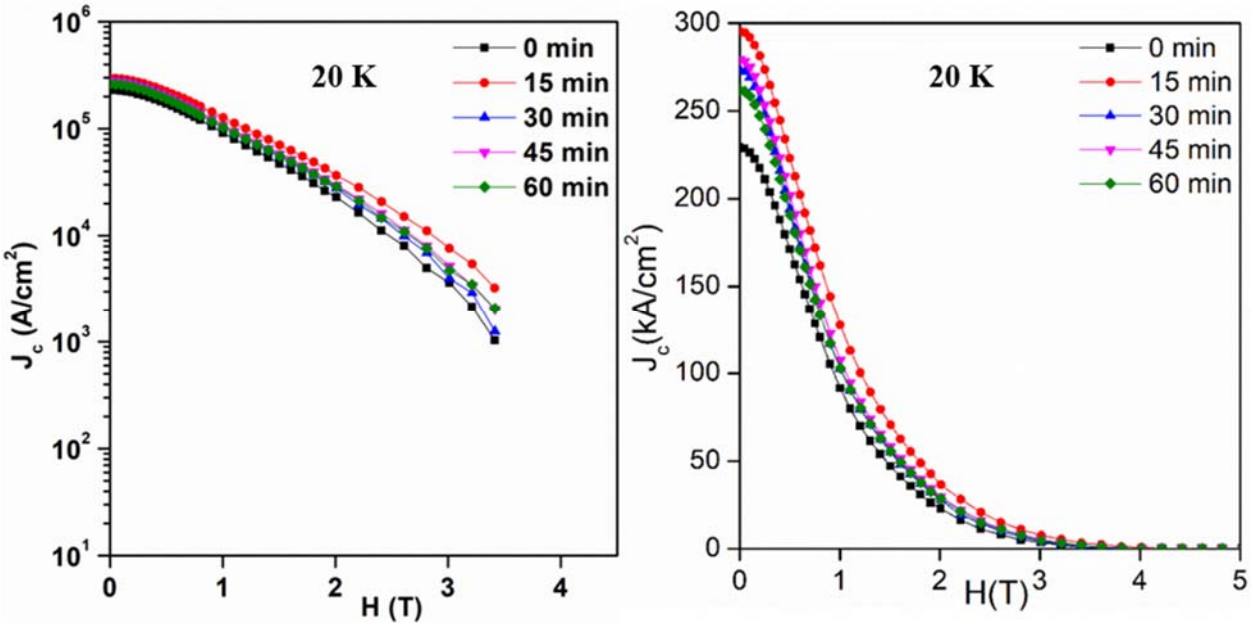

Fig. 6.6: Superconducting critical current density of ultra-sonicated samples (0, 15, 30, 45, 60 min). All samples show improvement in J_c. Especially, the 15 min ultra-sonicated sample shows superior improvement.

In order to understand this improvement, we carried out several microstructural studies using FE-SEM. In general, during the liquid-solid reaction of Mg and B, fine MgB_2 particles dissolve in the Mg melt and contribute to growth of bigger crystals [58]. From Fig. 6.7 (a-d), we can observe that the particles in microstructure B-15 bulk are much finer than other bulks. This is because the clustered boron particles merged to form larger MgB_2 grains in B-30, B-45 and B-60 bulks, which in turn reduced the grain boundary area. As we know, grain boundaries are primary pinning centres in bulk MgB_2 superconducting system. Hence the J_c reduction with the longer durations of ultra-sonication is a result of agglomeration or clustering of nano-B particles. While this also tells us that the grain boundary area is large in B-15 that aided in improving H_{c2}. From these results we can comprehend that this system reaches optimum at 15 minutes, from the current analysis. This is also evident from the decrease J_c values of B-30, B-45 and B-60. It can also be said that further ultrasonication might lead to an increase in boron cluster size and number, which will imply that the bulk microstructure consists larger grains, reducing the number of grain boundaries and therefore J_c. To justify this scenario, we measured the MgB_2 particle sizes using ImageJ. Fig. 6.8 reveals the average particle sizes of these bulks' microstructures. B-15 bulk has an average particle size of 260 nm, while B-30, B-45 and B-60 have 320, 350 and 370 nm respectively. The J_c observed was in

proportion with the measured average particle sizes for various bulks. This technique can be added to wires and tapes system, to harvest high performance at cheap means. Prior research on wires (Ag sheathed MgB_2 – 750°C/5 hrs) showed a critical current densities of around 2 x10^4 A/cm^2, which is very less when compared to our present bulk J_c values [59]. Hence we can see prospects of improving performance of wires also with employing ultrasonication treatment.

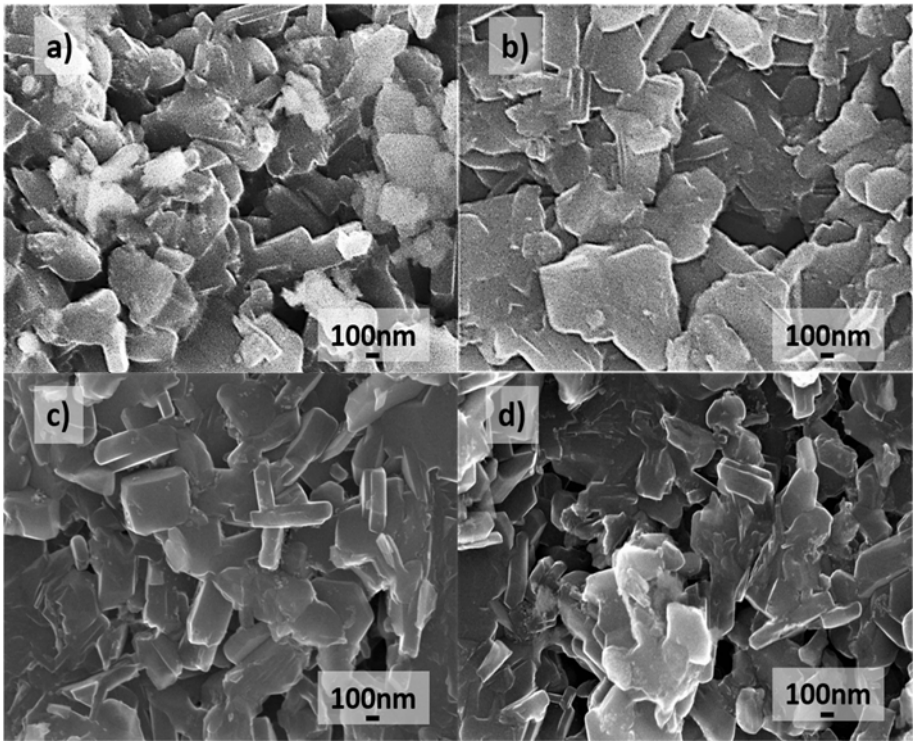

Fig. 6.7: FE-SEM images of a) 15 min ultra-sonicated MgB_2 bulk sample, b) 30 min ultra-sonicated MgB_2 bulk sample, c) 45 min ultra-sonicated MgB_2 bulk sample and d) 60 min ultra-sonicated MgB_2 bulk sample. The agglomerated tiny B particles grow into large grains in longer ultra-sonicated boron based bulk MgB_2.

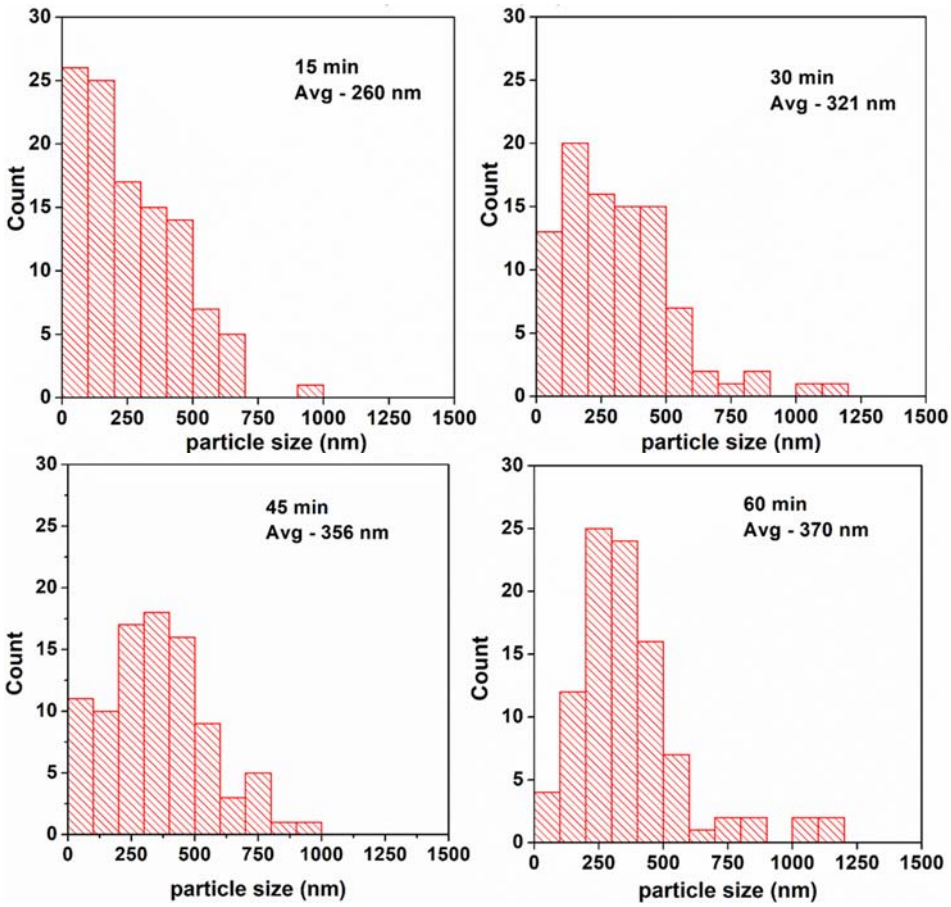

Fig. 6.8: Partcile-size distributions obtained from the analysis of the surface morphology by SEM, for the samples a) 15 min ultra-sonicated MgB_2 bulk sample, b) 30 min ultra-sonicated MgB_2 bulk sample, c) 45 min ultra-sonicated MgB_2 bulk sample, and d) 60 min ultra-sonicated MgB_2 bulk sample.

We calculated the density of bulks using, *density = Mass/ Volume* and arrived at a density of approximately 1.23-1.3 g/cm^3, which accounts to half of theoretical density of MgB_2 (2.6 g/cm^3), or also explained as 50% porosity. All of our samples and in general, bulk MgB_2 synthesized by conventional sintering show this behavior. To observe the effect of ultra-sonication on pinning mechanism, we calculated flux pinning diagrams. The results were evaluated in terms of Dew-Hughes general expression [60].

$$f_p = A(h)^p(1-h)^q \tag{6.1}$$

where f_p is normalized flux pinning force, $f_p=F_p/F_{p,max}$, and h is reduced magnetic field, $h=H/H_{irr}$, where the irreversibility field, H_{irr}, was determined as the field, where J_c in the $J_c(H)$ dependence

fell down to 100 A/cm^2, a standard practice in our works. The $f_p(h)$ dependence was analysed at 20 K. The dependence of equation 6.1 exhibits one peak at the field H_{max}. Dew-Hughes correlated the peak positions with different types of pinning in the material. In our case, the peak position was located at 0.22 (see Fig. 6.9), which is close to the position 0.2 predicted by Dew Hughes to grain boundary pinning (δl pinning). This result was expected because we only reduced the size of raw material (boron), increasing the grain boundary area. In fact, grain boundary pinning is a standard pinning mechanism observed in sintered bulk MgB_2 superconductor systems to which our samples belong. We tried to calculate p and q of Dew Hughes expression by fitting Eq. (6.1) and obtained at $p \sim 0.7$, $q \sim 2.7$, and $A \sim 5.6 \pm 0.11$. The fit curve is the displayed as a wine coloured line in Fig.6.8, labelled as Fit Curve-Eq(6.1). The fitted curve perfectly imitates flux pinning diagrams of all the bulk samples. However these curves have slender FWHM when compared to theoretical grain boundary pinning diagram, p=0.5 and q=2 (the dark cyan coloured curve, labelled as Ref in Fig.6.9). From the figure it is clear that the classical model was broad, as it is established for isotropic materials. However, in case of the polycrystalline bulk MgB_2, factors such as anisotropy and current percolation play important roles that can significantly slenderize the curve. In addition, there might be an effect of magnetic relaxation resulting in a difference between H_{c2}, to which magnetic fields in the original model were reduced, and H_{irr} determined by equilibrium between flux pinning and relaxation.

Table. 6.2: Curve fit parameter estimations using Dew Hughes expression on flux pinning diagrams.

Parameter	Value	Standard error
p	0.7	-
q	2.7	-
A	5.6	0.11

It is possible to estimate contributions of various pinning mechanisms by modifying Dew-Hughes general expression [60]. We tried to calculate the contributions from grain boundary pinning and point pinning. The reason for choosing point pinning among various pinning mechanisms [61,62] is that there is no scope for volume pinning ($p = 0$ & $q = 2$) as no secondary phase particles or dopants or δT_c pinning phases were added or formed during MgB_2 synthesis.

We used equation (6.2), with $p1 = 0.5$ & $q1 = 2$ (grain boundary pinning), and $p2 = 1$ & $q2 = 2$ (point pinning), A_1 & A_2 being constants and w is a weight factor.

$$f_p = w \times [A_1(h)^{p1}(1-h)^{q1}] + (1-w) \times [A_2(h)^{p2}(1-h)^{q2}] \quad (6.2)$$

By fitting Eq. (6.2) we arrived at $A_1 \sim 3.6$, $A_2 \sim 3.2$, and $w \sim 0.9545$, that indicates that nearly 95.5 % of pinning comes from grain boundaries, while the rest (5.5%) being point pinning.

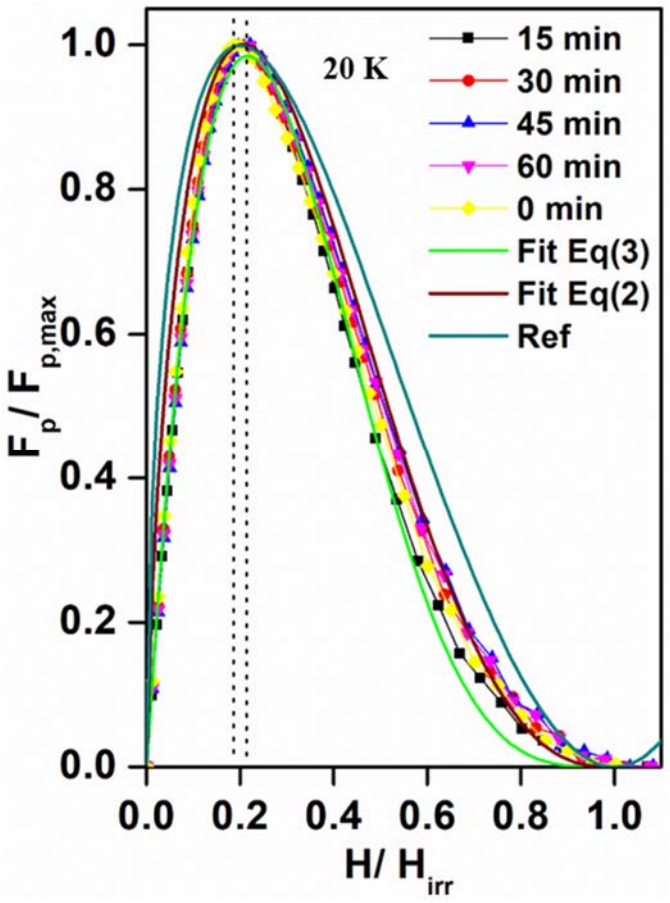

Fig. 6.9: Flux Pinning diagram of ultra-sonicated samples (0, 15, 30, 45, 60 min) with curve fitting of equation 6.1 & equation 6.2. Peak position ~ 0.22 indicating the dominance of grain boundary pinning.

In the previous research by Zongqing Ma et.al [63], where MgB_2 was doped by Cu, and synthesized at various temperatures, it was shown that tiny $MgCu_2$ nano-inclusions serve as point

pinning centres most effective at high fields. Depending on the working temperature, the Cu addition effect differed and the primary pinning mechanism also changed. The nano-scale MgB_2 particles formed in our work might function in a similar fashion. But, as mentioned earlier, these particles exist only on pore surfaces and hence have very little contribution to flux pinning.

We also measured pinning properties of the best sample (15 min ultra-sonicated boron based MgB_2) at various temperatures ranging from 10-35 K, giving insight into potential use in applications. High self-field J_c such as 434 and 382 kA/cm^2 was observed at 10 and 15 K, respectively (see Fig. 6.10). H_{irr} was higher than 5 T at 10 K, which indicated applicability up to high magnetic fields.

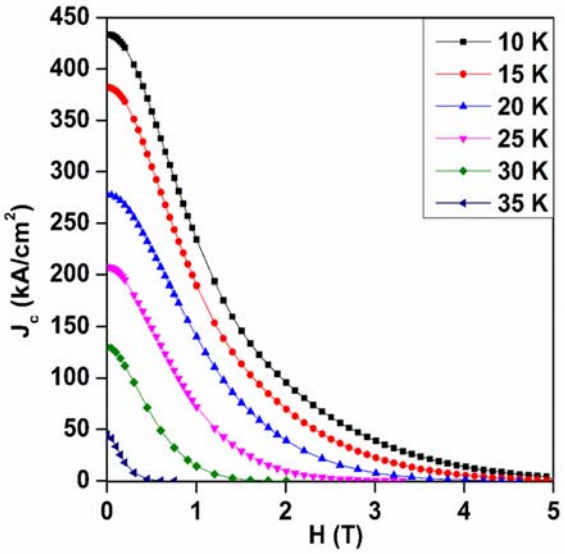

Fig. 6.10: Superconducting critical current density of 15 min ultra-sonicated sample at various temperatures. High self-field J_c such as 434 and 382 kA/cm^2 was observed.

Flux pinning studies revealed that the $f_p(h)$ peak position slightly shifted towards lower fields with decreasing temperature, but stood in the range of 0.18 to 0.25 (see Fig. 6.11). This increase is because of decrease in the magnetic anisotropy with increase in temperature. Overall these results point that grain boundary pinning is still dominant, even at low temperature.

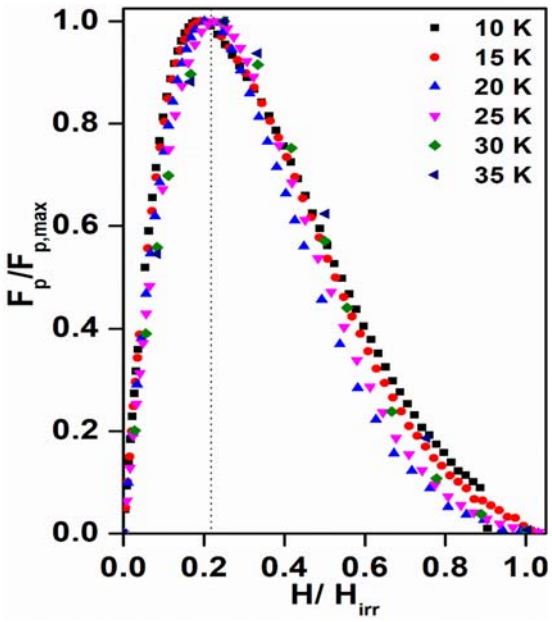

Fig. 6.11: Flux pinning diagram of 15 min ultra-sonicated sample at various temperatures (10 to 35 K). Peak position = 0.18 ~ 0.25, indicating the dominance of grain boundary pinning.

6.1.4 Conclusion

A novel high energy ultra-sonication technique was applied on cheap commercial boron precursor to improve superconducting performance of sintered bulk MgB_2. We successfully refined boron up to nanometer size without formation of B_2O_3. Longer ultrasonication resulted in clustering of boron particles. XRD and magnetic studies of bulk MgB_2 fabricated with this powder showed no impurities and high quality (T_c ~ 38.5 K; ΔT_c ~ 0.7 K). Fine nanometer sized particles were observed via FE-SEM responsible for J_c improvement (by about 36 %). Our study revealed that 15 minutes of ultra-sonication in ethanol is optimal for the best performance and reaches saturation thereafter because of the larger grains in the matrix. J_c as high as 434, 382, and 280 kA/cm^2 was observed in MgB_2 bulk based on for 15 minutes ultra-sonicated boron at 10, 15, and 20 K, respectively. Flux pinning studies indicated that dominant pinning was grain boundary pinning. The ultra-sonication technique is highly cost effective, impurity free, and scalable and thus suitable for transfer of bulk MgB_2 material to practice.

6.2 Influence of hexane dispersant on superconducting properties of high-energy ultra-sonicated boron based sintered bulk MgB_2

6.2.1 Experimental procedure

This section is fragmented into two parts such as; i) preparing refined boron precursor from cheap commercial crystalline boron (Furu-uchi chemicals, 300 mesh) using ultra-sonic homogenizer, ii) fabrication of bulk MgB_2 from the precursors-Mg powder and Refined boron powder obtained from part i).

i) In search of optimum conditions in hexane medium, the ultra-sonication time was varied, while maintaining power constant, at 50% (150 W) and frequency at 20 Hz. Continuous ultrasonication results in temperature rise of solution, hence we employed alternative intervals of 30 seconds run and pause. Effectively 15, 30, 45, and 60 minutes of ultasonication was carried out. The powder soon was heated around 100ºC in a muffle furnace for an hour to get rid of residual hexane.

ii) The precursors used were commercial powders (Furu-uchi Chemical Corporation) of amorphous Mg powder (99.9% purity, 200 meshes), ultra-sonicated boron powder. The rest of the processing was similar to Chapter 6.1. From here on MgB_2 bulks made from 15, 30, 45 and 60 hexane ultrasonicated boron will be addressed as H15, H30, H45 and H60 respectively.

These bulks were later characterized using XRD, FE-SEM, EDAX and SQUID for understanding phase purity, microstructure, compositional analysis and superconducting properties respectively.

6.2.2 Results and Discussion

In the novel technique –'High Energy Ultrasonication', the medium used to disperse boron powder is an important factor, in similar fashion to ball milling. Hence various medium result in different result, and in this work we used hexane. Hexane is a common lab chemical which has low boiling point (hexane boiling point - 68ºC) and is cheap. As soon as boron is ultrasonicated, the powder is separated and heated 100ºC for an hour, to ensure complete hexane evaporation. To check for any unwanted carbon incorporation from dispersant, we analyzed the powder using XRD (Fig. 6.12). XRD scanning from 2θ (10-60º) points out that there is no considerable change with

duration of ultrasonication as well as nature of dispersant. These powders were used to make MgB_2 bulk which were then studied for their superconducting performance.

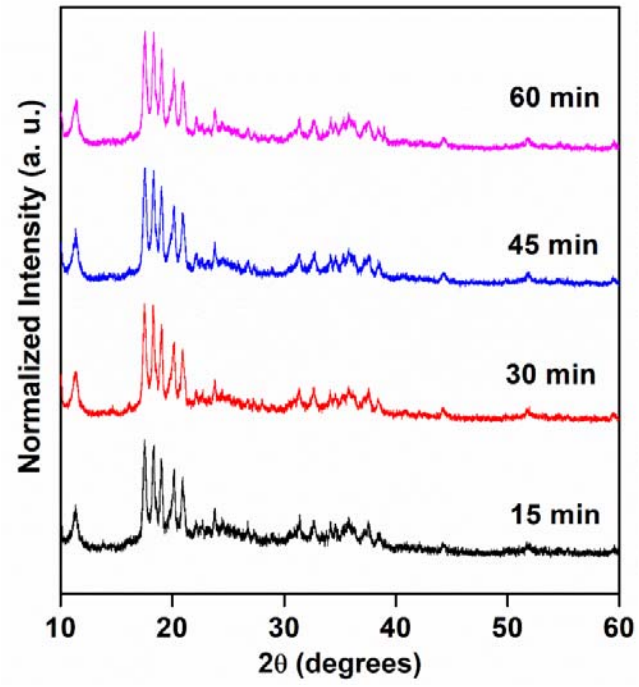

Fig. 6.12: XRD of the Boron ultra-sonicated for 15, 30, 45 and 60 minutes in hexane medium.

XRD of MgB_2 bulks prepared from ultrasonicated boron precursors (shown in Fig. 6.13) reveals that usage of boron ultrasonicated in hexane over 45 min (H45 and H60) started showing unreacted Mg in the final matrix. Apart from that scarce amount of MgO is also formed which is a common impurity. Furthermore the intensity of Mg peak (proportional to Mg wt%) increased with increase in ultrasonication duration. This most likely due lack of exposure of boron because of agglomeration, thereby leaving unreacted Mg. As discussed in Chapter 6.1, agglomeration in this system happens quite early.

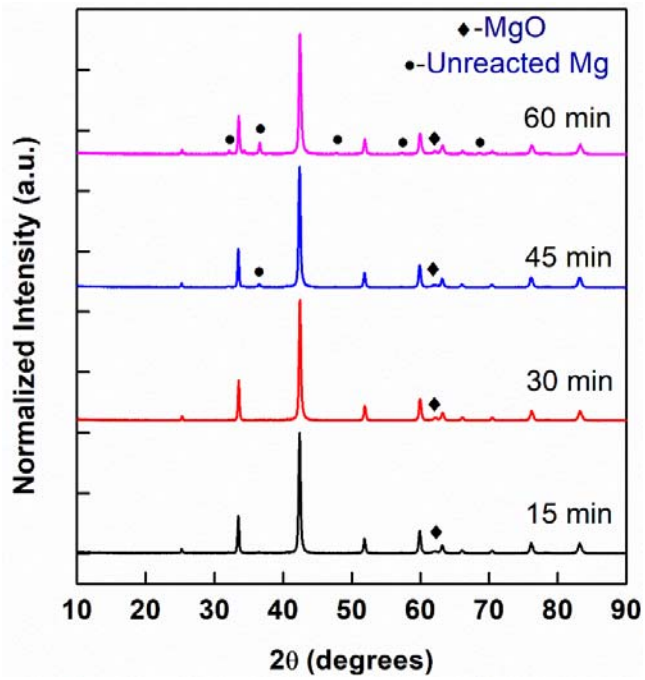

Fig. 6.13: XRD of the bulk MgB_2 fabricated with hexane ultra-sonicated boron (15, 30, 45, 60 minutes).

Table. 6.3: Critical onset and offset temperatures of bulk MgB_2 samples prepared with hexane ultra-sonicated boron.

Bulk	$T_{c,onset}$ (K)	$T_{c,zero}$ (K)	ΔT_c (K)
MgB_2-15 min Hex-B	38.5	37.9	0.6
MgB_2-30 min Hex -B	38.5	37.8	0.7
MgB_2-45 min Hex-B	38.5	37.8	0.7
MgB_2-60 min Hex-B	38.3	37.3	1

While SQUID magneto metric measurements reveal that all the samples show high $T_{c,onset}$ close to 38.5 K and ΔT_c around 0.7 K, which show that the bulks fabricated are of high quality. Table. 6.3 presents the detailed transition temperatures of all specimens. ΔT_c of bulk H60 is highest of all bulk, as the unreacted Mg is maximum. Fig. 6.14 shows the M-T curves of all bulks, while the inset figure shows the variance of ΔT_c of various bulks. Unreacted Mg akin to dopants is a non-superconducting phase that deteriorates T_c [64-69]. Examples of such scenarios comprise of

dopants like carbon sources, Ti, Cu, Fe, SiC and others resulted in decrease in T_c. Furthermore, the T_c drop increases with increase in amount of dopants added.

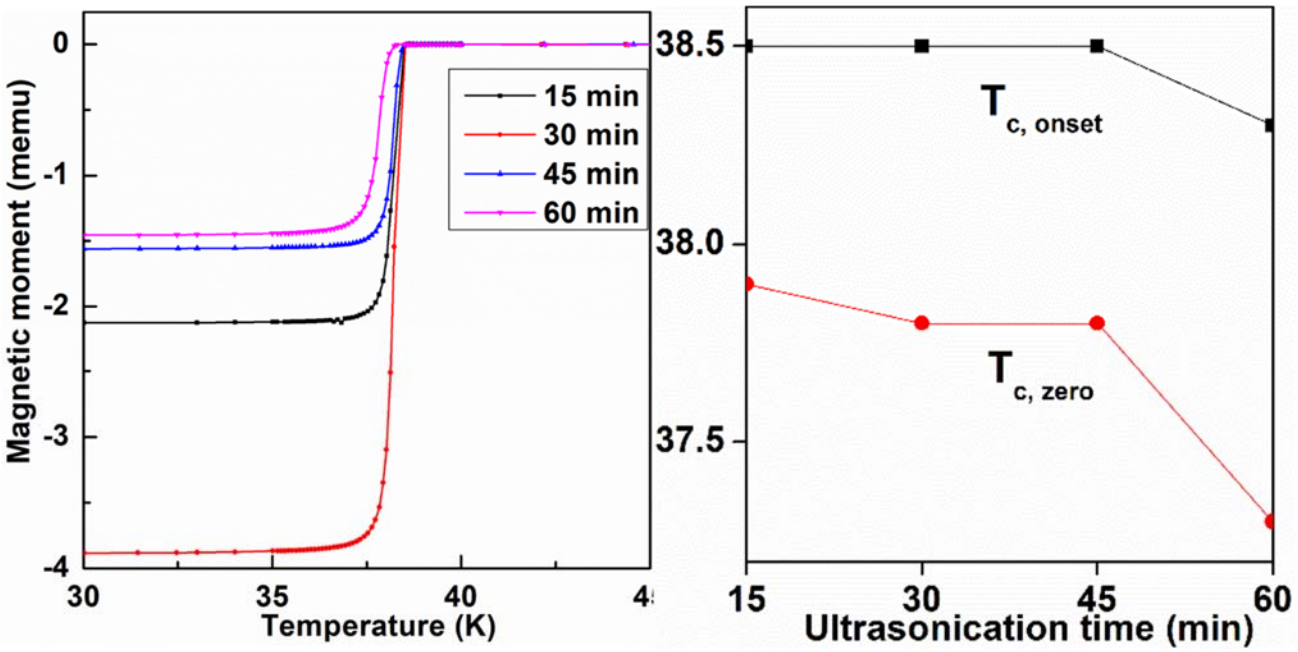

Fig. 6.14: Superconducting transition temperature of MgB_2 bulk made from Hexane ultra-sonicated boron powder (15, 30, 45, 60 min).

On the other hand, J_c has increased for all the bulks when compared to non-ultrasonicated system (220 kA/cm^2). However follows a trend of peak behavior with maximum in H30 bulk. Fig. 6.15 provides the $J_c - B$ curves. Self-field J_c of H30 has raised up to 260 kA/cm^2, at 20 K (approximately 20 % increment), H15 and H45 has raised up to 250 kA/cm^2, at 20 K (approximately 15 % increment), and H60 has raised up to 230 kA/cm^2, at 20 K (approximately 5 % increment). Simultaneously, flux pinning diagrams are calculated using Dew-Hughes expression [60]. In brief, normalized flux pinning force ($f_p=F_p/ F_{p,max}$) was plotted against reduced magnetic field ($h=H_o/H_{irr}$) at 20 K for various bulks, where H_{irr} is the irreversibility field taken as the field, where J_c fell down to 100 A/ cm^2 (see Fig. 6.16). The peak position is located to 0.18 (~0.2), which depicts the grain boundary pinning (δl pinning) behaviour which is expected because the ultrasonication helped in increasing grain boundaries in final microstructure.

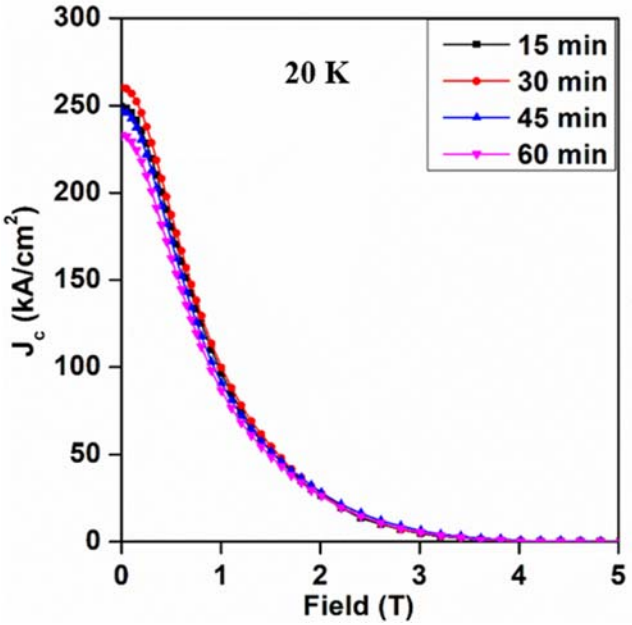

Fig. 6.15: Superconducting critical current density of MgB_2 bulk made from Hexane ultra-sonicated boron powder (15, 30, 45, 60 min). All samples show improvement in J_c. Especially, the 30 min ultra-sonicated sample shows superior improvement.

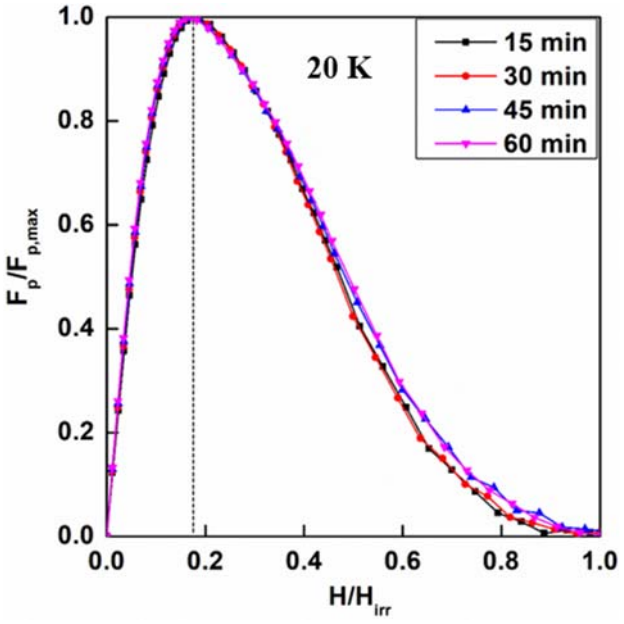

Fig. 6.16: Flux pinning diagrams of MgB_2 bulk made from Hexane ultra-sonicated boron powder (15, 30, 45, 60 min). Peak position ~ 0.2 indicating the dominance of grain boundary pinning.

FE-SEM images (see Fig. 6.17) show a peculiar layered structures in all bulks, which is one of the important reasons from increment in J_c. However, the primary reason is due to the particle size refinement, similar to what we have observed in the ethanol medium scenario from chapter 6.1. Later Energy dispersive –X-ray analysis revealed that the layered structure contains more oxygen than regular matrix, likely an Mg-B-O phase (Fig. 6.18). From the quantitative analysis, it is found that oxygen is 4.5 wt% in layered structure and 2.2 wt% in the regular matrix. In the beginning we assumed that the phase might be regular MgO, however boron wt% was also significantly observed in layered structure. In previous studies such phases were observed in this system, popularly known as oxygen rich MgB_2 [70, 71].

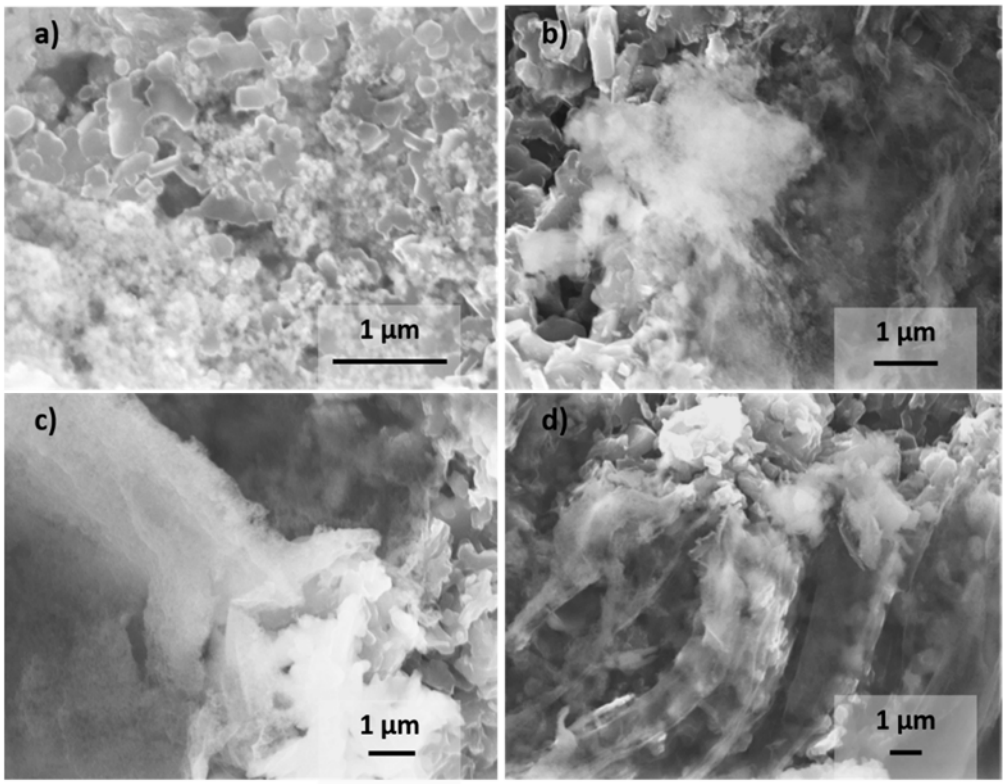

Fig. 6.17: FE-SEM images of a) MgB_2 bulk made from 15 min hexane ultra-sonicated boron powder, b) MgB_2 bulk made from 30 min hexane ultra-sonicated boron powder, c) MgB_2 bulk made from 45 min hexane ultra-sonicated boron powder and d) MgB_2 bulk made from 60 min hexane ultra-sonicated boron powder.

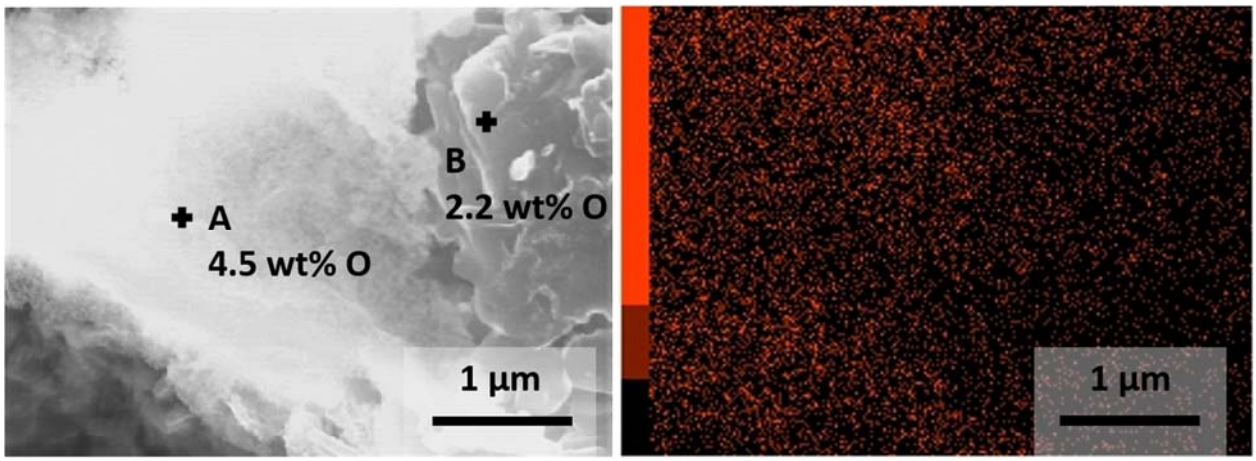

Fig. 6.18: Oxygen weight percentage in MgB_2 bulk made from 30 min hexane ultra-sonicated boron powder.

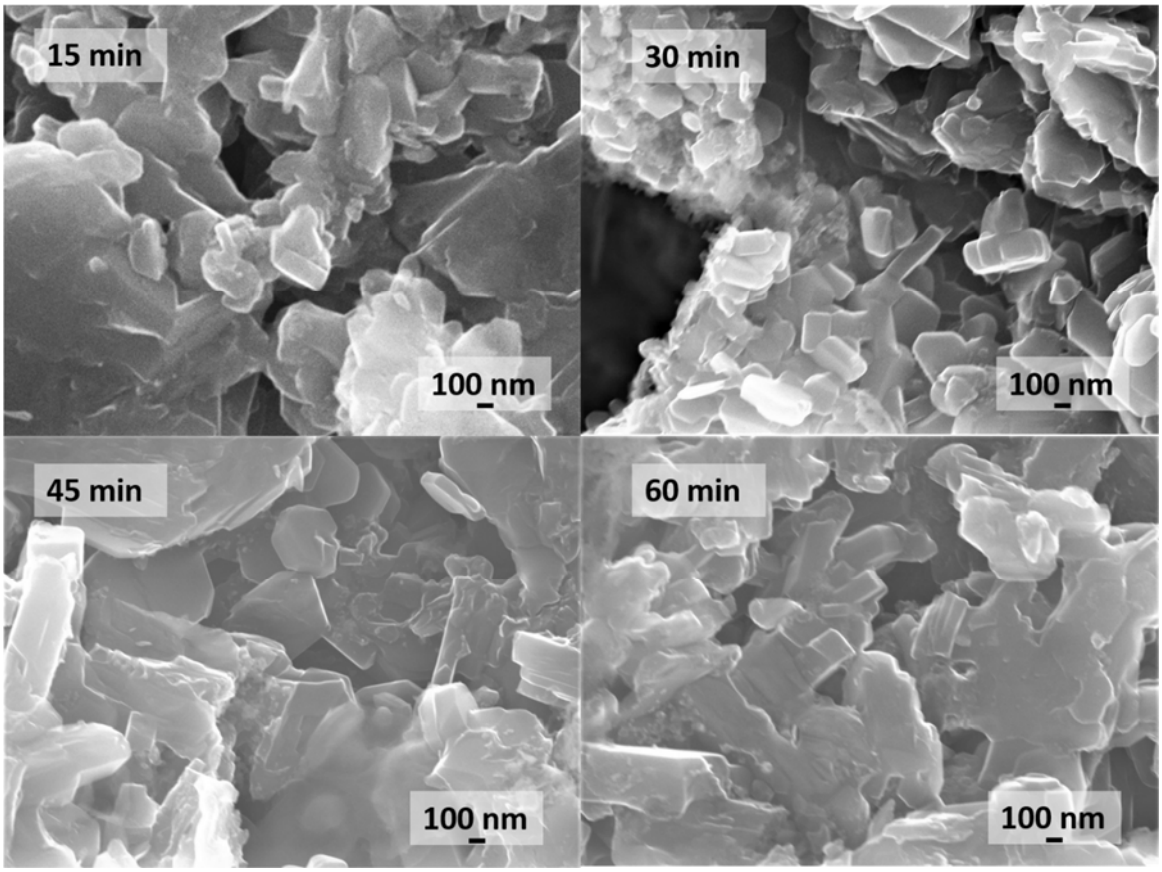

Fig. 6.19: FE-SEM images of fractured surfaces of a) MgB_2 bulk made from 15 min hexane ultra-sonicated boron powder, b) MgB_2 bulk made from 30 min hexane ultra-sonicated boron powder, c) MgB_2 bulk made from 45 min hexane ultra-sonicated boron powder and d) MgB_2 bulk made from 60 min hexane ultra-sonicated boron powder.

On the other hand, the J_c values of the present bulk are below those of MgB_2 made of in ethanol ultra-sonicated boron. FE-SEM images of fractured surfaces (Fig. 6.18) show that grains are much larger in the present bulks compared to MgB_2 made of in ethanol ultra-sonicated boron. The particles/grains in H30 are the finest, followed by comparable H15 and H45 and largest are in H60. These trends reflect what we observed in J_c. The bigger particles are most likely due to the low refinement of boron precursor powder due to a low viscosity of hexane.

To estimate the limits of H30 bulk for practical applications, we performed M-H measurements at various temperatures such as 10 to 35 K with 5 K intervals. High self-field J_c such as 370, 330, 260, 200, 125 and 50 kA/cm^2 was observed at 10, 15, 20, 25, 30, and 35 K, respectively (see Fig. 6.20). Flux pinning studies revealed that the $f_p(h)$ peak position was static at 0.2 (see Fig. 6.21). This shows that grain boundary pinning is still dominant, irrespective of temperature below T_c.

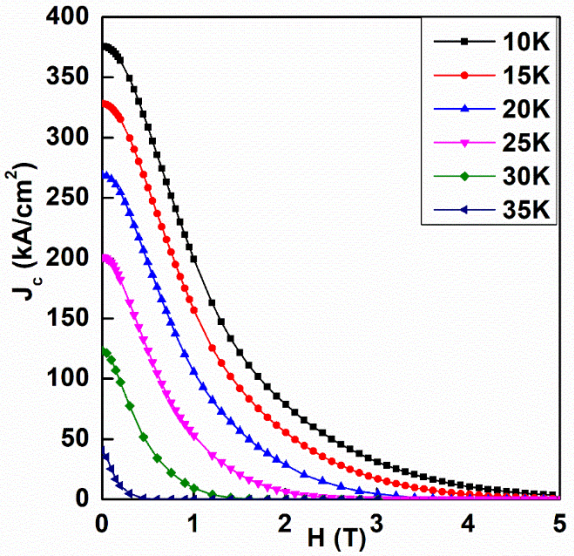

Fig. 6.20: Superconducting critical current density of MgB_2 bulk made from 30 min hexane ultra-sonicated boron powder, at various temperatures. High self-field J_c such as 375 and 330 kA/cm^2 was observed at 10 and 15 K respectively.

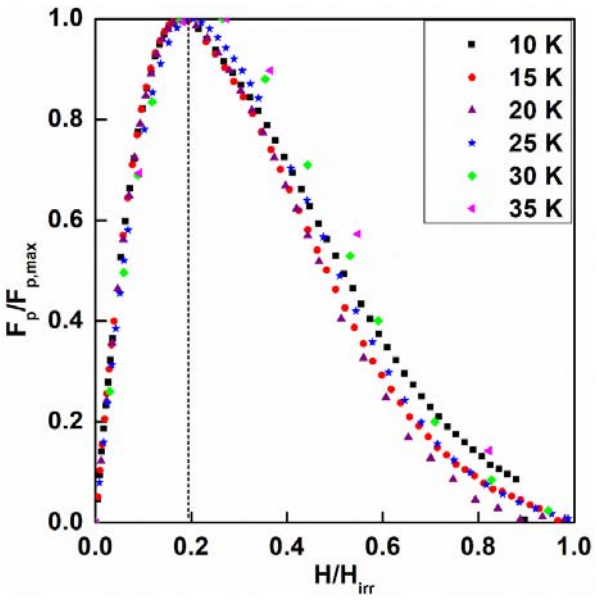

Fig. 6.21: Flux pinning diagram of MgB_2 bulk made from 30 min hexane ultra-sonicated boron powder, at various temperatures (10 to 35 K). Peak position ~ 0.2, indicating the dominance of grain boundary pinning.

6.2.3 Conclusion

Ultrasonicated boron powder was free of boric oxide and carbon contamination, which was confirmed by XRD. However XRD of bulk MgB_2 fabricated with the long duration (> 45 min) ultrasonicated powder showed signs of unreacted Mg in the final matrix. M-T curves revealed that longer ultrasonication of boron in the hexane medium can result in large ΔT_c (~1K). Because of the peculiar microstructure such as Mg-B-O layers and refined grains, J_c performance improved by about 20%. The present work reveals that 30 minutes of B ultra-sonication in hexane is optimal for the best performance. J_c as high as 370, 330, and 260 kA/cm^2 was observed in the best bulk at 10, 15, and 20 K, respectively. Flux pinning studies indicated that dominant pinning was grain boundary pinning. The performance was poor compared to ethanol medium ultrasonicated samples. However, other parameters such as oscillating frequency and power etc. are yet to be studied for obtaining best condition.

6.3 Effect of distilled water high-energy ultra-sonicated boron on sintered bulk MgB_2

6.3.1 Experimental

Like in prior chapters (6.1 and 6.2), in this work we tried to investigate optimum ultrasonication time in distilled water medium for refining cheap commercial boron (Furu-uchi chemicals, 300 mesh). The ultra-sonication time was varied from 15 to 60 minutes with an interval of 15 minutes, under constant power (50% of maximum limit - 150 W) and frequency (20 Hz). The powder soon was heated around 125 ^oC in a muffle furnace for an hour to get rid of residual water. These refined powders are mixed with amorphous Mg powder (99.9% purity, 200 meshes) in a molar ratio of 1:2 and ground rigorously for 30-40 minutes in a glove box containing Argon atmosphere. Pellets of 20 mm diameter, 7 mm thickness were pressed using a uniaxial hydraulic press with a force of approximately 20 kN. These pellets were wrapped in Titanium (Ti) foils and sintered in a tube furnace at 775^oC for 3 hours with continuous Ar flow. From here on MgB_2 bulks made from 15, 30, 45 and 60 distilled water ultrasonicated boron will be addressed as W15, W30, W45 and W60 respectively.

The bulks after sintering are characterized by High-resolution automated Rigaku smart-lab X-ray powder diffractometer (RINT2200) with a step size of 0.01^o over 20^o to 90^o, using Cu-K_α radiation generated at 40 kV and 30 mA was used to identify the phase information. Followed by M-H and M-T curves measurements using a SQUID magnetometer. Special specimens with dimensions around 1x1x0.5 mm^3 were made from bulk MgB_2 pellets which are subjected to varied magnetic field (0 – 5 T) and temperature (10 – 50 K). Later J_c and flux pinning are estimated using Extended Bean's Critical state model and Dew Hughes equation respectively.

6.3.2 Results and Discussion

From the XRD shown in Fig. 6.22, it is evident that there are no contaminants present in the matrix apart from scarce quantities of MgO, which is formed during the transfer from glove box to furnace and the pressing step.

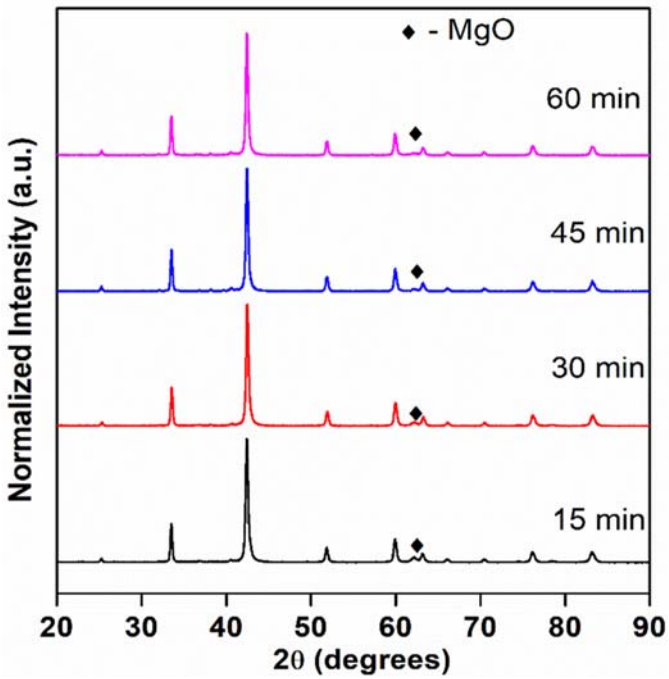

Fig. 6.22: XRD of the bulk MgB_2 fabricated with distilled water ultra-sonicated boron (15, 30, 45, 60 minutes).

From Fig. 6.23 (a-e), we can observe that the particles in microstructure of W0 are big and agglomerated, while W15 and W30 bulk are much finer. And the microstructure of W45 and W60 are finer, but not as fine as in W30. Slight hints of agglomeration can also be observed. This scenario looks very similar to of the ethanol medium, where the maximum performance was observed in B-15 bulk. In a similar hypothesis, based on microstructure it is expected to have highest J_c in W30 bulk followed by W15 and then others. This is because of the increase in number of grains helps in increased flux pinning. In case of W45 and W60, the grains look bigger and collated to form large grains and hence we can expect decrease in J_c.

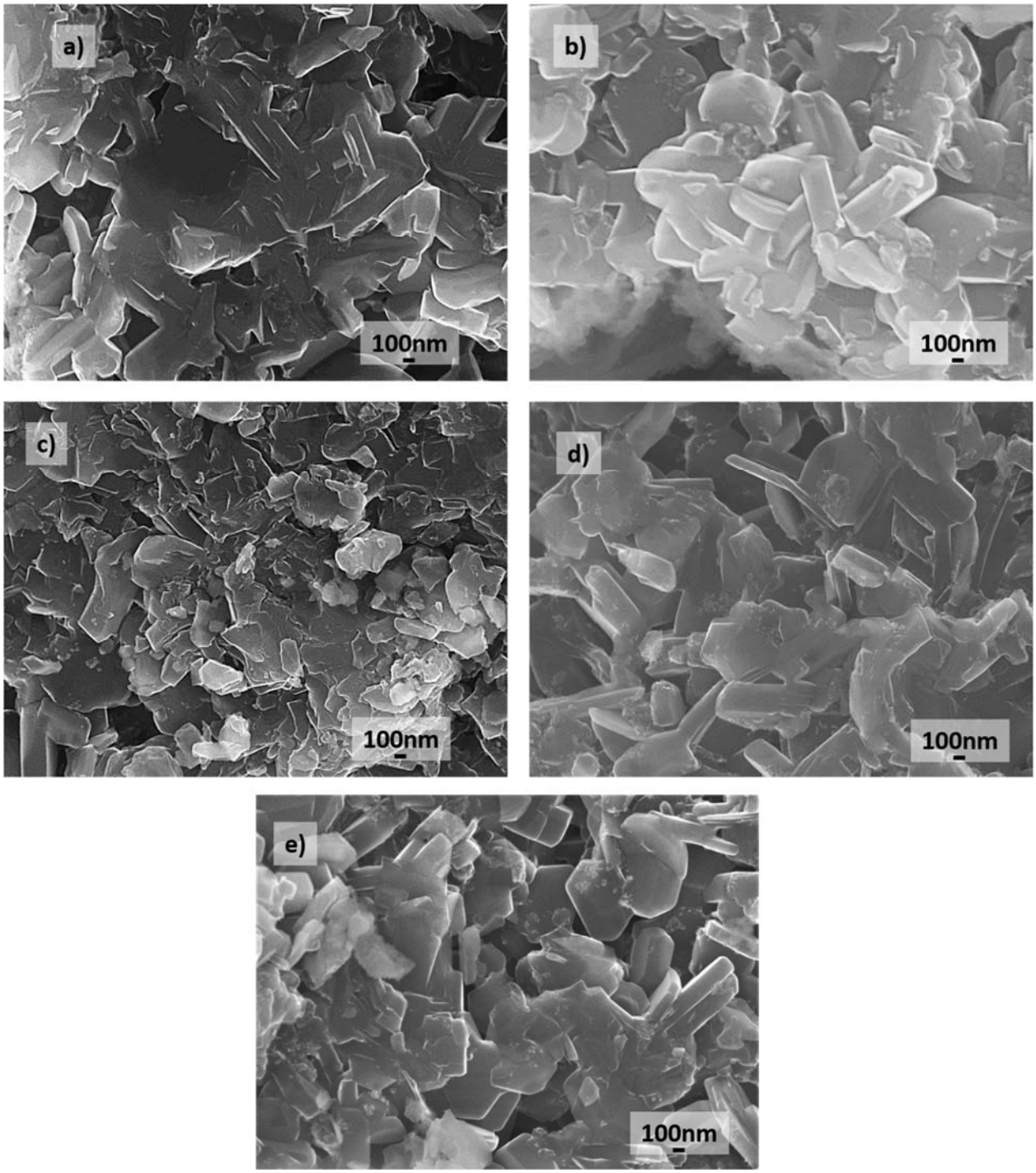

Fig. 6.23: FE-SEM images of various MgB_2 bulks; a) non ultrasonicated, b) made from 15 min distilled water ultra-sonicated boron powder (W15), c) MgB_2 bulk made from 30 min distilled water ultra-sonicated boron powder (W30), d) MgB_2 bulk made from 45 min distilled water ultra-sonicated boron powder (W45) and e) MgB_2 bulk made from 60 min distilled water ultra-sonicated boron powder (W60).

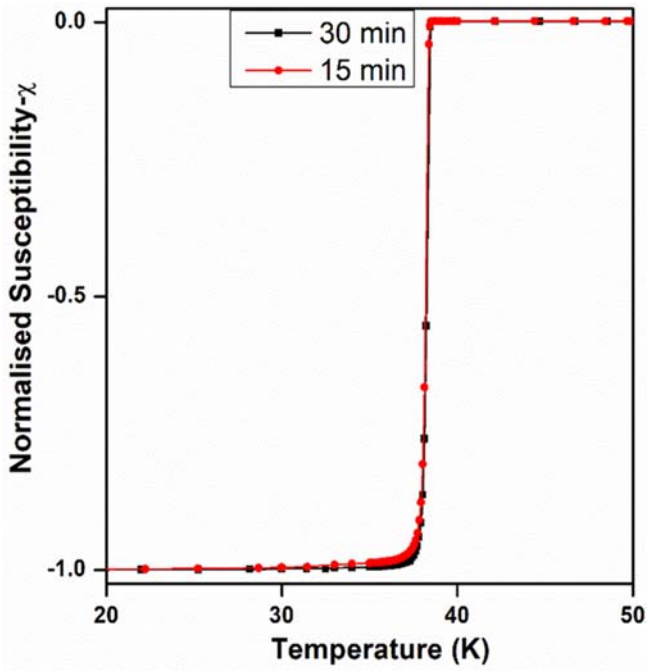

Fig. 6.24: Normalized Susceptibility vs Temperature curves of MgB_2 bulks made from distilled water ultrasonicated boron (15, 30 min).

M-T or superconducting critical temperature studies were performed on W15 and W30 (see Fig 6.24). $T_{c,onset}$ of the both bulks was around 38.5 K, similar to that of bulks made for other media ultrasonicated boron. ΔT_c of both the bulks was around 0.5 K which implies a sharp transition that depicts high quality bulk MgB_2. While critical current density plotted (Fig. 6.25) using M-H curves, reveal that as anticipated the W30 bulk showed the highest J_c. Self-field J_c at 20 K was 295, 303, 260 and 240 kA/cm^2 in W15, W30, W45 and W60 bulks respectively, which amounts upto 34, 36, 18 and 9% improvement. The J_c values followed the predicted trend and was consistent with all media. Much clear details can be found from Table. 6.4

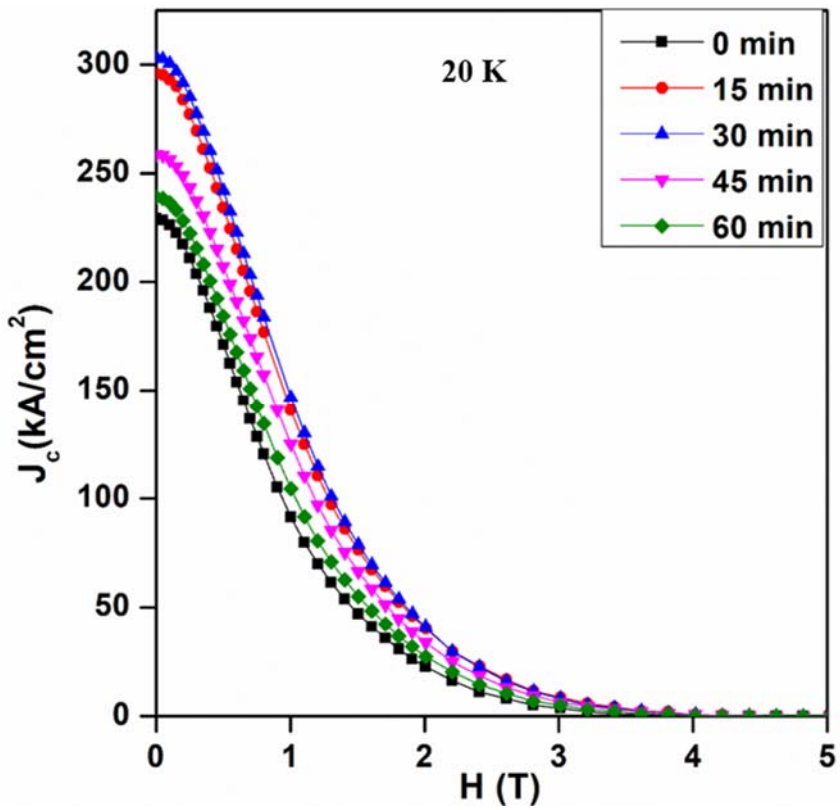

Fig. 6.25: J_c- H curves of MgB_2 bulks made from distilled water ultrasonicated boron (15, 30, 45 and 60 min minutes).

Table. 6.4: Superconducting properties of MgB_2 bulks made from distilled water ultrasonicated boron (15, 30, 45 and 60 min).

Bulk	$T_{c,onset}$ (K)	ΔT_c (K)	Self-field J_c (kA/cm^2), at 20K	% increase in J_c
MgB_2-15 min Ultra-B	38.5	0.6	295	34 %
MgB_2-30 min Ultra-B	38.4	0.5	303	36 %
MgB_2-45 min Ultra-B	-	-	260	18 %
MgB_2-60 min Ultra-B	-	-	240	9 %

6.3.3 Conclusion:

High energy ultra-sonication technique using distilled water medium was applied on cheap commercial boron precursor to improve superconducting performance of sintered bulk MgB_2. XRD shows that single bulk MgB_2 was fabricated with very scarce MgO impurities. While critical

transition temperature results (T_c ~ 38.5 K; ΔT_c ~ 0.5 K) revealed high quality bulk. Refined grain structure was observed via FE-SEM in final bulks that are made up of ultrasonicated boron. This microstructure is responsible for J_c improvement (by about 35 %) in both MgB_2 bulks made out of boron ultra-sonicated in distilled water for 15 and 30 minutes. Self-field J_c as high as 303 and 295 kA/cm^2 was observed in W15 and W30 at 20K. The present results show that the performance of bulk is similar to that of what we observed in ethanol medium, however better than hexane medium. Furthermore, it is evident from all the systems ethanol, hexane and water media that 15-30 minutes of pre ultrasonic treatment to boron powder is optimum for best J_c.

6.4 References

[1] J N, N N, T M, Y Z, J A, *Nature*, **2001**, 410, 63.

[2] Duband L, Collaudin B, *Cryogenics (Guildf).,* **1999**, 39, 659–63.

[3] Kim Y, Park I, Jeong S, *Cryogenics (Guildf).,* **2013**, 57**,** 113–21.

[4] Pan C, Zhang T, Zhou Y, Wang J, *Cryogenics (Guildf).,* **2016**, **77,** 20–4.

[5] Kajikawa K, Nakamura T, *IEEE Trans. Appl. Supercond.,* **2009**, 19**,** 2–6.

[6] Rafieazad M, Balcı Ö, Acar S, Somer M, *Bor Derg.,* **2017**, 2**,** 87–96.

[7] Baig T, Al Amin A, Deissler R J, Sabri L, Poole C, Brown R W, Tomsic M, Doll D, Rindfleisch M, Peng X, Mendris R, Akkus O, Sumption M, Martens M, *Supercond. Sci. Technol.,* **2017**, 30**.**

[8] Yao W, Bascuñán J, Hahn S, Iwasa Y, *IEEE Transactions on Applied Superconductivity,* **2010**.

[9] Eisterer M, *Supercond. Sci. Technol.,* **2007**.

[10] Tomsic M, Rindfleisch M, Yue J, Mcfadden K, Phillips J, Sumption M D, Bhatia M, Bohnenstiehl S, Collings E, *Int. J. Appl. Ceram. Technol.,* **2007**.

[11] Larbalestier D, Gurevich A, Feldmann D M, Polyanskii A, *Nature,* **2001**.

[12] Muralidhar M, Inoue K, Koblischka M R, Tomita M, Murakami M, *J. Alloys Compd.,* **2014**, 608**,** 102–9.

[13] Muralidhar M, Nozaki K, Kobayashi H, Zeng X L, Koblischka-Veneva A, Koblischka M R, Inoue K, Murakami M, *J. Alloys Compd.,* **2015**, 649**,** 833–42.

[14] Mackinnon I D R, Shahbazi M, Alarco J A and Talbot P C, *Supercond. Sci. Technol.,* **2017**, 30**.**

[15] Bhagurkar A G, Yamamoto A, Dennis A R, Durrell J H, Aljohani T A, Nadendla H B, Cardwell D A, *J. Am. Ceram. Soc.,* **2017**, 100**,** 2451–60.

[16] Rosová A, Kulich M, Kováč P, Brunner B, Scheiter J, Häßler W, *Supercond. Sci. Technol.,* **2017**, 30**.**

[17] Arvapalli S S, Miryala M, Murakami M, *IEEE Trans. Appl. Supercond.,* **2019**, 29**,** 1–4.

[18] Arvapalli S S, Miryala M, Murakami M, *Adv. Eng. Mater.,* **2019**, 21**.**

[19] Kauffmann-Weiss S, Hassler W, Guenther E, Scheiter J, Denneler S, Glosse P, Berthold T, Oomen M, Arndt T, Stocker T, Hanft D, Moos R, Weiss M, Weis F, Holzapfel B, *IEEE Trans. Appl. Supercond.,* **2017**, 27**,** 2–5.

[20] Cai Q, Liu Y, Guo Q, Ma Z, Li H, *Scr. Mater.,* **2016**, 124**,** 184–8.

[21] Zou X, Zhang W, Wang Q, Zheng L, Yu X, Yu Z, Zhang H, Zhao Y, Zhang Y, *Mater. Lett.,* **2019**, 244, 111–4.

[22] Ma Z, Liu Y, Cai Q, Jiang H, Yu L, *Mater. Chem. Phys.,* **2013**, 141**,** 378–82.

[23] Ma Q, Peng J, Ma Z, Cheng F, Lan F, Li C, Yang Z, Liu C, Liu Y, *Mater. Chem. Phys.,* **2018**, 204**,** 62–6.

[24] Cai Q, Liu Y, Guo Q, Ma Z and Li H, *Scr. Mater.,* **2016**, 124,184–8

[25] Aldica G, Burdusel M, Badica P, *Phys. C Supercond. its Appl.,* **2014**.

[26] Noudem J G, Aburras M, Bernstein P, Chaud X, Muralidhar M, Murakami M, *J. Appl. Phys.,* **2014**, 116**.**

[27] Murakami A, Iwamoto A, Noudem J G, *IEEE Trans. Appl. Supercond.,* **2018**, 28**.**

[28] Giunchi G, Ripamonti G, Cavallin T, Bassani E, *Cryogenics (Guildf).,* **2006**, 46**,** 237–42.

[29] Ishiwata J, Muralidhar M, Inoue K, Murakami, *Phys. Procedia,* **2015**, 65**,** 69–72.

[30] Peng J, Cai Q, Cheng F, Ma Z, Li C, Xin Y, Liu Y, *J. Alloys Compd.,* **2017**, 694**,** 24–9.

[31] Prikhna T, Eisterer M, Goldacker W, Gawalek W, Sokolovsky V, Weber H W, Kozyrev A V., Moshchil V E, Sverdun V B, Kovylaev V V., Karpets M V., Basyuk T V., Shaternik A V., *IEEE Trans. Appl. Supercond.*, **2015**, 25**.**

[32] Prikhna T A, Eisterer M, Weber H W, Gawalek W, Kovylaev V V., Karpets M V., Basyuk T V., Moshchil V E, *Supercond. Sci. Technol.,* **2014**, 27**.**

[33] Zeng R, Lu L, Wang J L, Horvat J, Li W X, Shi D Q, Dou S X, Tomsic M, Rindfleisch M, *Supercond. Sci. Technol.,* **2007**, 20**,** 1–6.

[34] Ansari I A, *Ceram. Int.,* **2019**, 45, 1523–7.

[35] Sudesh, Kumar N, Das S, Bernhard C, Varma G D, *Supercond. Sci. Technol.,* **2013**.

[36] Ansari I A, Shahabuddin M, Ziq K A, Salem A F, Awana V P S, Husain M, Kishan H, *Supercond. Sci. Technol.,* **2007**, 20**,** 827–31.

[37] Pan X F, Cheng C H, Zhao Y, *J. Supercond. Nov. Magn.,* **2011**, 24**,** 1611–6.

[38] Bugoslavsky Y, Cohen L F, Perkins G K, Polichetti M, *Nature,* **2001**, 411**,** 561–3.

[39] Konduru P, Singh A V P, Kandasami A, Dinakar K, Sreehari Sastry S, *Nucl. Instruments Methods Phys. Res. Sect. B Beam Interact. with Mater. Atoms,* **2019**, 438**,** 42–7.

[40] Zhou S, Pan A V., Wexler D, Dou S X, *Adv. Mater.,* **2007**, 19, 1373–6.

[41] Bohnenstiehl S D, Susner M A, Yang Y, Collings E W, Sumption M D, Rindfleisch M A, *Phys. C Supercond. its Appl.,* **2011**, 471**,** 108–11.

[42] Wilke R H T, Bud'ko S L, Canfield P C, Finnemore D K, Suplinskas R J, Hannahs S T, *Phys. Rev. Lett.,* **2004**, 92, 2–5.

[43] Ye S J, Matsumoto A, Zhang Y C, Kumakura H, *Supercond. Sci. Technol.,* **2014**, 27**.**

[44] Jun B H, Park S D, Kim C J, *J. Alloys Compd.,* **2012**, 535**,** 27–32.

[45] Herbirowo S, Sofyan N, Saragih R, Imaduddin A, Sebleku P, Herbirowo S, Sofyan N, Saragih R, Imaduddin A, *Am. Inst. Phys.,* **2017**, 020007**.**

[46] Muralidhar M, Higuchi M, Jirsa M, Diko P, Kokal I, Murakami M, *IEEE Trans. Appl. Supercond.,* **2017**, 27**,** 18–21.

[47] Arvapalli S S, Muralidhar M, Murakami M, *J. Supercond. Nov. Magn.,* **2018**, 2–6.

[48] Xu X, Kim J H, Yeoh W K, Zhang Y, Dou S X, *Supercond. Sci. Technol.,* **2006**, 19**.**

[49] Kang M O, Joo J, Jun B H, Park S, Kim C S, Kim C, *Prog. Supercond. Cryog.,* **2019**, 21**.**

[50] Palomino R L, Miró A M B, Tenorio F N, Jesús F S De, Escobedo C A C, Ammar S, *Ultrason. – Sonochemistry,* **2016**, 29**,** 470–5.

[51] Sreekumar V M, Babu N H, Eskin D G, Fan Z, *Mater. Sci. Eng. A,* **2015**, 628**,** 30–40.

[52] Nakaso K, Shimada M, Okuyama K, Deppert K, *J. Aerosol Sci.,* **2002**, 33**,** 1061–74.

[53] Vives Díaz N E, Hosmani S S, Schacherl R E, Mittemeijer E J, *Acta Mater.,* **2008**, 56**,** 4137–49.

[54] Yang F, Feng J Q, Xiong X M, liu G Q, Zhang P X, Li C S, Wang Q Y, Feng Y, Pang Y C, Li S Q, Yan G, *Phys. Procedia,* **2015**, 65**,** 157–60.

[55] RUI X F, SUN X F, XU X L, ZHANG L, ZHANG H, *Int. J. Mod. Phys. B,* **2005**, 19**,** 375–7.

[56] Aldica G, Plapcianu C, Badica P, Groza J R, *A Global Road Map for Ceramic Materials and Technologies: Forecasting the Future of Ceramics, International Ceramic Federation - 2nd International Congress on Ceramics, ICC **2008**, Final Programme.*

[57] Pan X F, Shen T M, Li G, Cheng C H, Zhao Y, *Phys. Status Solidi Appl. Mater. Sci.,* **2007**, 204**,** 1555–60.

[58] Ma Z, Liu Y, *Sintering of Ceramics - New Emerging Techniques,* **2012**, pp 469–98

[59] Glowacki B A, Majoros M, Vickers M, Evetts J E, Shi Y Superconductivity of powder-in-tube MgB_2 wires, **193.**

[60] Dew-Hughes D, *Philos. Mag.,* **1974**, 30**,** 293–305.

[61] Kramer E J, *J. Appl. Phys.,* **1973**, 44**,** 1360.

[62] Koblischka M R, Muralidhar M, *Int. J. Mod. Phys. B,* **2016**, 30**,** 1630017.

[63] Ma Z, Liu Y, Han Y, Zhao Q, Gao Z, Ma Z, Liu Y, Han Y, Zhao Q, Gao Z, *J. Appl. Phys.,* **2008**, 104**,** 0–5.

[64] M. Muralidhar, M. Higuchi, M. Jirsa, P. Diko, I. Kokal, M. Murakami, *IEEE Trans. Appl. Supercond*, **2017**, 27, 18.

[65] N.E. Vives Díaz, S.S. Hosmani, R.E. Schacherl, E.J. Mittemeijer*, Acta Mater*., **2008**, 56, 4137.

[66] F. Yang, J.Q. Feng, X.M. Xiong, G.Q. liu, P.X. Zhang, C.S. Li, Q.Y. Wang, Y. Feng, Y.C. Pang, S.Q. Li, G. Yan, *Phys. Procedia*, **2015**, 65, 157.

[67] X.F. RUI, X.F. SUN, X.L. XU, L. ZHANG, H. ZHANG, *Int. J. Mod. Phys. B*, **2005**, 19, 375.

[68] G. Aldica, C. Plapcianu, P. Badica, J.R. Groza, in A Glob. Road Map Ceram. Mater. Technol. Forecast. Futur. Ceram. Int. Ceram. Fed. - *2nd Int. Congr. Ceram. ICC* **2008**, Final Program.

[69] X.F. Pan, T.M. Shen, G. Li, C.H. Cheng, Y. Zhao, *Phys. Status Solidi Appl. Mater. Sci.,* **2007**, 204, 1555.

[70] Prikhna, T. et.al*, IEEE Transactions on Applied Superconductivity,* **2015**, 25(3), 1–4.

[71] T A Prikhna et al, *Supercond. Sci. Technol*., **2014**, 27, 044013.

Chapter 7

Summary and Conclusions

Bulk MgB_2 shows great potential for commercial applications under the conditions of good flux pinning, high H_{irr} & H_{c2} and J_c. In this work, we tried to address these issues via thorough understanding of the processing, microstructure control, magnetic performance and their intrinsic relationship. In addition, ways to attain high performance in a cheap way was also explored.

First, we tried to improve critical current density (J_c). From prior research we know that grain-boundaries are effective pinning centers in this material. Further, boron precursor particle size plays a vital role in optimizing J_c. To achieve this effect, we used a commercial nano-amorphous boron. The results were astonishing and J_c of 408 $kAcm^{-2}$ was observed at 20K, self-field. These results were justified by SEM micrographs, which revealed nano-sized grains in final microstructure and supported by flux pinning diagrams. However, the high field J_c and upper critical field H_{c2} was not improved much.

Second, carbon is considered the best dopant for H_{c2} and high-field pinning. However, there was a serious issue of inhomogeneous distribution of carbon in the matrix. To solve this issue, we used a carbon-encapsulated boron prepared by a special pyrolysis technique applied on nano-amorphous boron. Several wt% of carbon were applied and systematically studied. It was found that a low amount of carbon gives the best results. We further tested the carbon concentration and dispersion to find the precise optimum. As expected, both the high-field J_c and H_{c2} were improved and showed optimum values for 1.5 wt% carbon. Tremendous self-field J_c of 660 kA/cm^2 was observed at 10 K, and in high fields J_c also significantly increased. H_{c2} (calculated by extrapolation) was also substantially improved, being almost equivalent to the best records reported so far. To further improve this result, our group tried to add Ag. Microstructural analysis showed Ag-Mg phases formed in the matrix and optimum performance was observed for 4 wt% Ag. To compensate for loss of Mg entering reaction with Ag, as well as to increase the Ag-Mg phase fraction, we then added excess Mg to the precursor. 7.5 wt% excess of Mg resulted in the best result, with highest

Ag-Mg phase (2 wt%), high irreversibility field (H_{irr}) of 4.76 Tesla and large J_c such as 440 kA/cm^2 at 20 K, self-field. SEM analysis confirmed presence of secondary Ag-Mg phases and improved microstructural changes such as Ag-Mg particle refinement, up to 20-40 nm which acted as pinning centers. Although these values were remarkable, the commercial precursors were expensive, which might make the final product costly. In order to reach this level of performance with cheap inputs, we introduced a novel technique of high-energy ultra-sonication and explored the possibilities. The main aim in this work was to create nano-sized boron via ultra-sonication, and arrive at high J_c in the final bulk. Various dispersants, like ethanol, hexane and distilled water, were used to suspend the boron particles during ultra-sonication. Beside size refinement, the obtained fine boron powder was free of B_2O_3, due to which the MgB_2 bulks were of good quality. TEM and SEM analysis on ultrasonicated boron revealed nano-sized particles. Among all attempts, ultra-sonication in ethanol and water resulted in the highest J_c of 300 kA/cm^2 at 20 K, self-field (35% improvement compared to bulk MgB_2 produced by normal commercial boron powder). Low duration ultra-sonication for 15 min and 30 min in ethanol and distilled water was enough to reach the best performance. Further ultra-sonication caused boron powder to get agglomerated, which resulted in large grains in the final microstructure.

In conclusion, the present work checks ways to tackle the current trending issues in bulk MgB_2 and make it suitable for use in practical applications.

List of Figures

List of Tables